Synthesis and characterisation of fluoride containing transition metal phosphate and sulfate framework materials

Marshall, Kayleigh

Award date:
2020

Awarding institution:
University of Bath

Synthesis and characterisation of fluoride containing transition metal phosphate and sulfate framework materials

Kayleigh Louise Marshall

A thesis submitted for the Degree of Doctor of Philosophy

University of Bath

Department of Chemistry

September 2019

COPYRIGHT

Declaration of authorship

I am the author of this thesis, and the work described therein was carried out by myself personally, with the exception of the atomic absorption spectroscopy measurements used in chapter 4, section 4.1, which were carried out by Alan Carver: Elemental analysis instrument technician, Dept. of Chemistry; chapter 5, section 5.1 to 5.3 and chapter 6 section 6.1 where 40% of the work was carried out by two project students (Stefanie Zekoll and Hannah Sullivan) who produced the synthetic reactions.

Signature Date

Acknowledgements

First and foremost, I would like to dedicate this work to my Mum, Debbie Marshall, who passed away during the first year of this project and is sorely missed. As the wonderful woman who raised me single-handedly, I can only hope I am making her proud.

Secondly, I would like to thank my fiancé Ben, for the sacrifice and support on my journey through this research. You have been my rock and kept me going when things got tough, thank you for just being you.

To the rest of my family and friends, my deepest thanks are extended for believing in me when I didn't believe in myself and being a great support network. I am truly grateful for all the great memories created during my time in Bath and I have met some truly inspiring people who have vastly enriched my life.

To Mark and all the members of the Weller group I had the pleasure of working with, thank you for your guidance and support, both academically and personally. Dom, Kevin, Anto, Oli, Adam, Beth and Pascaline: You all ROCK!!

Abstract

Synthesis and characterisation of fluoride containing transition metal phosphate and sulfate framework materials

A variety of transition metal and lanthanide polyhedral framework materials have been successfully synthesised and characterised. The preparation of these materials was carried out under high fluoride hydrothermal (hydrofluorothermal) conditions or with a high temperature ceramic method. The prepared material structures were characterised with single-crystal X-ray diffraction (SXRD) with further analysis by powder X-ray diffraction and scanning electron microscopy (SEM).

Fluoride containing transition metal phosphates and sulfates have several potential applications as electrode and electrolyte battery materials due to high ion transport capacities which arise from the ability of the transition metal polyhedra and phosphate/sulfate tetrahedra to connect in a multitude of combinations to form stable frameworks with sufficiently low energy pathways for lithium and sodium intercalation. The ability of the transition metal centres to undergo charge balancing redox reactions during the ionic intercalation also plays a vital role in the applications of these materials. The addition of fluoride is believed to increase the cell potential when incorporated into the polyanioic frameworks due to its high electronegativity producing an increased inductive effect.

High temperature ceramic and hydrothermal techniques employed with high fluoride reagents have produced nineteen new inorganic materials, whose structures have been characterised by SXRD. Transition metal (M = Ti, Mn, V, and Cr) and lanthanide (Ln = Y, Nd, Eu, Gd, Tb, Dy, Ho, Er) polyhedra interlinked by simple and complex anions (O^{2-}, F^-, PO_4^{3-}, SO_4^{2-}) formed a variety of structural motifs, from discreet complex polyhedral units, through one-dimensional chains and two dimensional layers to three-dimensional structures. Much lower dimensionality was generally observed for the fluoride sulfate phases based on titanium and manganese, while a higher dimensionality was achieved in the sodium lanthanide fluoride sulfate: $NaLn(SO_4)_2F$. These new inorganic materials add to the wealth of known structures with structural features suggestive of electrochemical/intercalation functionality.

Table of Contents

Chapter 1: Introduction

1.0 Inorganic materials

Interest in inorganic materials chemistry saw a resurgence in the past 20-30 years. With the onset of technological advances and new synthetic methods, solid-state chemists have been able to access a multitude of structures only previously found in nature (minerals). It is the relationship between these structures and their physical and chemical properties that have been the fundamental understanding required to enable the search of new materials which will better suit modern demands.

The simplest inorganic solid material is the binary transition metal oxide, formula $MO/MO_2/MO_3$. First-row transition metal monoxides adopt the rock-salt structure which exhibits a face centred cubic unit cell with a close-packed array of oxide ions. Non-stoichiometry is common for the first-row transition metal oxides with $Fe_{1-x}O$ being extensively studied.[1,2] Most transition metal dioxides adopt the rutile crystal structure which has a primitive tetragonal unit cell, rutile is the thermodynamic preference of the eight TiO_2 polymorphs: rutile, anatase, brookite, bronze, ramsdellite, hollandite, columbite and baddeleyite. Nanosized rutile TiO_2 had been investigated for a multitude of applications with particular interest in Li insertion as a potential anode material in high power lithium-ion batteries.[3] Transition metal trioxides are rare, and the structures generally consist of corner-sharing MO_6 octahedra in a primitive unit cell with varying degrees of distortion from ideal octahedral geometry.[4,5]

Ternary oxides such as perovskites of general formula ABO_3, where A is generally the larger of the two metal ions, are much greater in number due to the increased complexity of the formulation giving rise to a larger number of possible combinations of metal cations and oxide anions.[4] Perovskites of varying compositions have been investigated for their photovoltaic, ferroelectric, ferromagnetic and superconducting properties.[6] As well as the perovskite structure, many ternary transition metal oxides adopt the spinel structure type of general formula AB_3X_4 (X = O, S) which have been extensively investigated for their electrochemical and ion transport properties for use as electrode materials in rechargeable batteries (for further details see section 1.1.2 of this work). [7]

Zeolites are more complex inorganic materials which can be considered as frameworks constructed from linked tetrahedra such as AlO_4, SiO_4 and PO_4. Zeolites have the generic formula $\{[M_{n+}]_{x/n.}\ [mH_2O]\}\ \{[AlO_2]_x\ [SiO_2]_{1-x}\}$ and the numerous different linkages of TO_4 form a wide variety of structures containing large channels or cavities which make zeolites of high interest for use in absorption, ion exchange and catalysis.[4]

Polyanionic frameworks combine multivalent polyanions such as MO_6 and TO_4 creating stable framework materials exhibiting small ion conduction pathways in channels or between layers. Lithium and sodium-containing polyanionic structures have been shown to exhibit very fast ion conduction and have been termed NASICON (Na Super Ionic Conductor) with general formula $A_3M_2(XO_4)_3$ (A = Li, Na; M = Ti, V, Cr, Fe; X = P, As, S). [4,8]

1.1 Applications as battery materials

Since the onset of the technological revolution, the worlds energy requirements have grown exponentially. Today, almost everyone in the western world owns at least one portable electronic device and there are more cars on the roads than ever. In recent years, concern over burning of fossil fuels to supply the ever-increasing power demands to the world has pushed development of effective means of generating power from renewable sources such as wind and solar power. The major drawback is the lack of ability to efficiently store the excess power generated at peak harvest times. Much research has been focused on improving battery capacity to be able to combat this problem. As discussed briefly in the previous section great variety of inorganic materials show properties which are favourable for use as battery materials such as the ability to conduct cations through open channels/between layers, and the availability of redox-active transition metal centres. The following sections will discuss these materials and their development within the area of electrochemical energy storage.

First and foremost is a discussion of the basic principles and historical development of primary and secondary batteries and some of the first systems employed.

1.1.1 Primary batteries

In 1866 the first primary battery was developed by Georges-Lionel Leclanché, which comprised of a zinc-amalgam (Zn/Hg) anode, a carbon-rod centred MnO_2 cathode and an ammonium chloride solution as the electrolyte and after some development work had a voltage of 1.5 V and a capacity of 224 Ah/kg. [9]

The Leclanché cell was further improved by Carl Gassner in 1888 who used FeO(OH) mixed with MnO_2 and a small amount of carbon as the cathode and a hollowed zinc cylindrical container as the anode. An electrolyte paste comprising of $ZnCl_2$, ammonium chloride, water and wheat flour replaced the ammonium chloride liquid electrolyte. The layout of the cell was also altered by mixing the electrolyte paste with the cathode mixture before pouring it into the zinc container and placing a carbon rod in the centre of the paste. This cell was commercialised in 1896 with a potential of 1.5 V and a capacity of 146-202 Ah/kg and morphed into the zinc/carbon batteries which are sold widely today. [9]

$$Anode: Zn \rightarrow Zn^{2+} + 2e^- \quad + 0.76V \qquad \text{Equation 1.1}$$

$$Cathode: 2NH_4^+ + 2MnO_2 + 2e^- \rightarrow Mn_2O_3 + H_2O + 2NH_3 + 0.78V \qquad \text{Equation 1.2}$$

$$Zn + 2MnO_2 \rightarrow ZnO \cdot Mn_2O_3 \quad + 1.54\,V \qquad \text{Equation 1.3}$$

A major disadvantage of the zinc/carbon batteries is the presence of the electrolyte in the cell reaction; thus, the electrolyte is depleted on discharge of the cell. The zinc anode is also corroded by the presence of acidic NH_4^+ ions, the combination of these issues results in unstable voltages and short shelf lives for these batteries.[9]

The research attempts to improve the shelf-life and power density of zinc/carbon batteries led to the development of alkaline-manganese dioxide batteries which are the most common commercial dry cells. This system was first commercialised in 1959 by Ever Ready and employs the same cathode and anode as the zinc/carbon system but the electrolyte contains an alkaline $KOH_{(aq)}$ solution which has a greater ionic conductivity which results in a much lower internal electrical resistance for the cell. Alkaline batteries have a capacity of 65 Ah/kg which is 25-30% higher than the zinc/carbon cell.[9]

The primary lithium battery arose due to the demand for high energy density power sources to be used in small and lightweight equipment. Lithium is the lightest metal with a very low standard reduction potential (-3.05 V at 298 K) resulting in incredibly high capacity of 3860 Ah/kg (compared with Na: 1.16 Ah/g and Zn: 0.82 Ah/g). The major hurdle with lithium is its high reactivity (especially with water), this was overcome by using lower conducting organic electrolytes over aqueous solutions. This lower conductivity allows for low self-discharge which significantly improves battery shelf-life. [9]

In 1975 the first Li primary battery was made commercially available by Sanyo Electric Co. This utilised a lithium metal anode and a manganese dioxide cathode in a cylindrical battery for use in cameras. Many other cathode materials were also used in primary Li batteries including $SOCl_2$, SO_2Cl_2, TiS_2, $NbSe_3$ and MoS_3, all used in combination with lithium metal anodes. [9,10]

1.1.2 Secondary (rechargeable) batteries

The first rechargeable battery was developed in 1859, this was the lead-acid battery as shown in the schematic below (Figure 1.1). Though this is the oldest known rechargeable battery it is still used to start combustion engines in most cars today.[11]

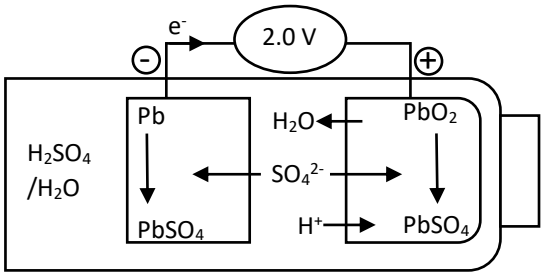

Figure 1.1 Schematic of a lead-acid battery

$$Pb + SO_4^{2-} \rightarrow PbSO_4 + H^+ + 2e^- \quad \text{Equation 1.4}$$

$$PbO_2 + SO_4^{2-} + 4H^+ + 2e^- \rightarrow PbSO_4 + H_2O \quad \text{Equation 1.5}$$

$$Pb(s) + PbO_2 + 2H_2SO_4 \rightarrow 2PbSO_4 + 2H_2O \quad \text{Equation 1.6}$$

In the case of the lead-acid battery shown above, the anode consisting of lead reacts with the sulfate ions of the electrolyte, giving off electrons to the external circuit (Equation 1.4). At the cathode lead oxide reacts with sulphate ions, protons and electrons to form lead sulfate and water (Equation 1.5).[11]

The second rechargeable battery system was invented in 1899 which comprises of a nickel hydroxide/graphite cathode, a cadmium hydroxide/cadmium oxide/iron anode and potassium hydroxide solution electrolyte. During discharge NiO(OH) in the cathode forms $Ni(OH)_2$ while Cd in the anode oxidises to $Cd(OH)_2$. The operating voltage of these batteries is 1.25 V with a capacity of 20 Ah/kg and a power of 27 Wh/kg. Some water decomposition to hydrogen and nitrogen occurs at the end of every charge of this system which is negated with design features of the battery such as excess capacity given to the anode. Other design improvements were made and material changes to a NiO(OH) or Ni_2O_3 cathode, Cd metal anode and KOH aqueous electrolyte containing a small amount of LiOH. This improved system has a working voltage of 1.2 V, a capacity of 50 Ah/kg and a power of 40-60 Wh/kg. Ni-Cd batteries have a higher energy density and a longer life than lead-acid batteries but suffer drawbacks caused by conversion of NiO(OH) into $NiO_2(OH)$ irreversibly over a long period of usage as well as the use of toxic cadmium in the anode.[11]

Secondary alkaline manganese batteries comprise of a zinc gel anode (Zn powder mixed with gelled KOH), a MnO_2/graphite doped with 10% Bi_2O_3 cathode mixed together in the aqueous potassium hydroxide electrolyte solution to form a paste which is packed in a hermetically sealed cell. These batteries have twice the energy density of Ni-Cd cells at 80

Wh/kg with a working voltage of 1.5 V, combine this with the lack of toxic cadmium, secondary alkaline manganese batteries became a popular choice for use in toys and smaller low powered personal devices. Disadvantages of secondary alkaline manganese batteries include a high internal resistance resulting in low load currents of less than 400 mA.[11]

As with the primary batteries in the previous section, lithium is attractive for the secondary battery systems because it is the lightest and most electropositive metal. The first commercialised secondary lithium-ion (Li-ion) battery was released by Sony in 1991 and is represented by the schematic below (Figure 1.2).[12]

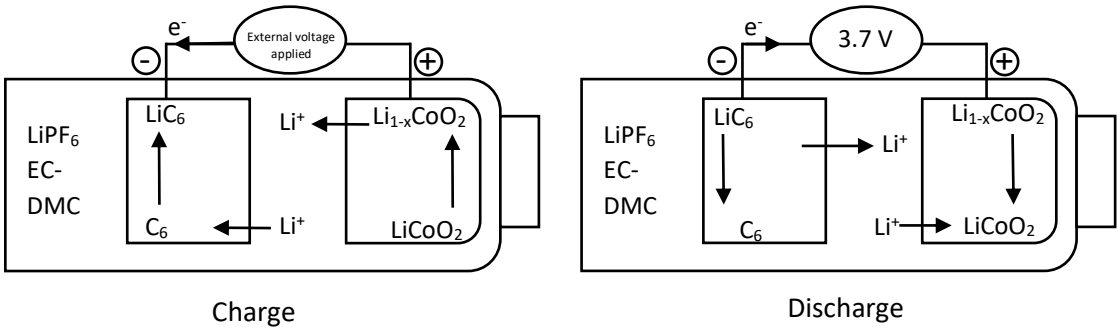

Figure 1.2 Schematic of charging (left) and discharging (right) of a Li-ion battery

$$Li_xC_6 + Li_{1-x}CoO_2 \xrightarrow{discharge} C_6 + LiCoO_2 \qquad \text{Equation 1.7}$$

These Li-ion batteries work on the principle that lithium ions can be reversibly intercalated into the electrodes via the electrolyte medium (normally an aqueous or organic liquid), producing around 3.7V at 25 °C with a 150 Ah/kg capacity and power over 200 Wh/kg.[12]

1.1.2.1 Cathode material development

There has been a vast amount of research centred around improving the performance of cathode materials for lithium-ion batteries. The following will review the progress made over the last 30 years of cathode material development.

Layered oxides

The sony cell commercialised in 1991 contained a cathode made from the cobalt analogue of the layered transition metal oxides, general formula: $LiMO_2$ (M = Co, Ni, Mn, V). The crystal structure of $LiCoO_2$ reported by Goodenough *et al.* comprises alternating layers of interconnected CoO_6 octahedra and octahedrally coordinated lithium ions (Figure 1.3).[13] The structure shows a trigonal unit cell in space group $R\bar{3}m$, the layers are stacked above

one another in the c-direction and comprise of edge-sharing octahedrally coordinated cobalt(III) ions in the *a*- and *b*- directions. [13,14]

Delithiation between x = 0.21 - 0.51 in $Li_{1-x}[Co/Ni]O_2$ results in a reversible phase transition from trigonal crystal symmetry to monoclinic. When $x > 0.5$ the structure becomes destabilised due to the high oxidation potential increasing reaction with the organic electrolyte. This reduces the capacity of batteries based on $LiCoO_2$ cathodes to around half of the theoretical capacity if 100% delithiation was possible.[14]

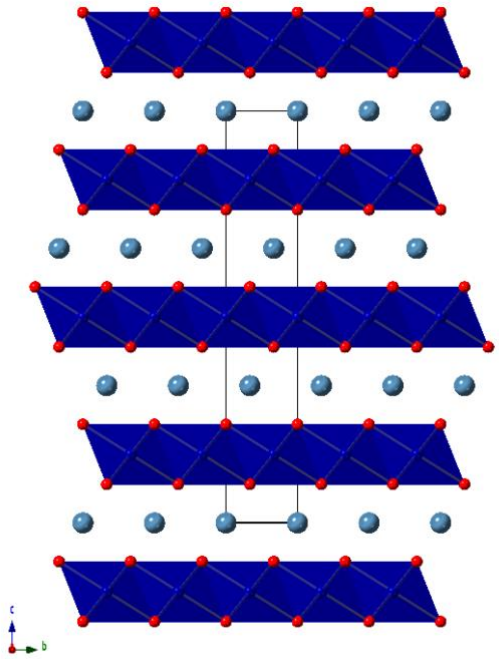

Figure 1.3 Structure of $LiCoO_2$ viewed along the a-axis. Co octahedra are shown in royal blue, O atoms in red and Li atoms in pale blue. The unit cell is outlined in black.

Spinel oxides

The natural progression from the two-dimensional layered oxides is to the three-dimensional spinel oxides, of general formula $Li[M_2]O_4$ (M = Ti, Mn, Co, V). Of particular interest is the $LiMn_2O_4$ analogue, due to environmental and economic perspectives as manganese is much more abundant than cobalt and non-toxic. $LiMn_2O_4$ crystallises with cubic symmetry in the space group $Fd\bar{3}m$. The crystal structure of $LiMn_2O_4$ comprises a three-dimensional framework of edge-sharing MnO_6 octahedra with lithium ions occupying the tetrahedral holes in between MnO_6 octahedra framework (Figure 1.4). [14]

$LiMn_2O_4$ cathode charge-discharge profiles show two distinct plateaus around 4 and 4.1V (vs. Li/Li^+) which is attributed to the two-step reversible lithium intercalation. The

theoretical value of specific capacity based on intercalation of one lithium ion per formula unit at room temperature is 148 mAh/g but $LiMn_2O_4$ suffers from capacity fading on prolonged current discharge which is increased at elevated temperatures. This capacity fade is attributed to structural changes occurring at the surface of the electrode whereby overlithiation results in oxidation of Mn^{4+} to Mn^{3+} and subsequent Jahn-Teller distortion and reduction in crystal symmetry from cubic to trigonal. The formation of phase separation between the two crystal structures disrupts the lithium diffusion pathways and disrupts electronic conductivity. Efforts to reduce this effect have involved surface coatings and partial substitution of Mn for other cations. Numerous coatings have been explored; including Al_2O_3, $LiCoO_2$ and $AlPO_4$, all showing improvement in capacity retention of cathodes.[14–16] Substituted manganese spinels have been widely investigated with the effects of both cationic and anionic substitution reported by Manthiram *et al.* who found that partial substitution of both Mn and O reduced capacity face without sacrificing capacity values. Their systematic investigation of the $Li_{1+x}Mn_{2-2x}M_xO_{4-\delta}F_\delta$ ($0.075< x <0.15$; M = Al, Ti, Cr, Fe, Co, and Ni; $0 < \delta <0.38$) system showed that initial charge capacity values increased with increasing δ, and that capacity loss in 50 cycles decreased significantly from M = Ti to Al, Cr, Fe, Co and Ni.[17]

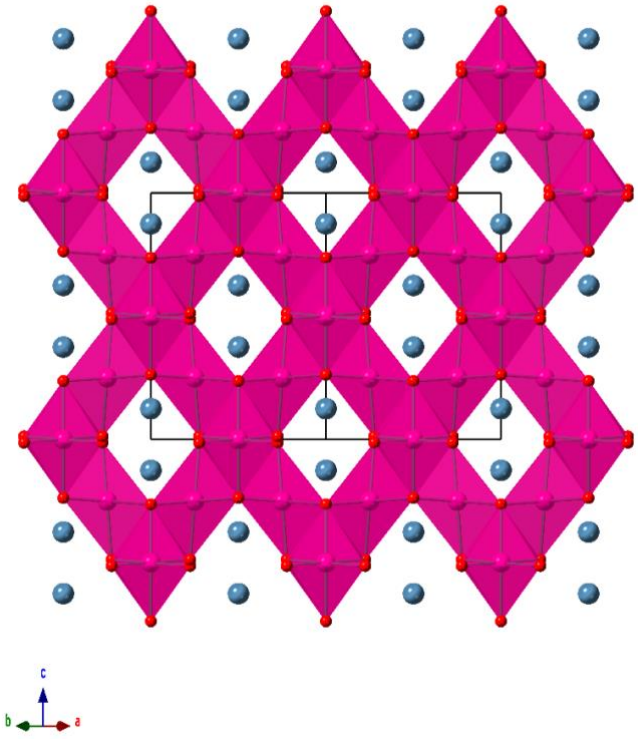

Figure 1.4 Structure of $LiMn_2O_4$ viewed along the a^*-direction. Mn octahedra are shown in magenta, O atoms in red and Li atoms in pale blue. The unit cell is outlined in black.

Olivines

The iron phosphate analogue of olivine structure of general formula Li_xMXO_4 (M = Mn, Fe, Co and Ni; X = P, S and As) has also garnered a great deal of interest since its first introduction as a potential cathode material by Padhi *et al.* in 1997.[18] $LiFePO_4$ crystallises in the space group *Pnma* and comprises a three-dimensional framework which is built from layers of corner-sharing FeO_6 octahedra interconnected by edge and vertex sharing with PO_4 tetrahedra (Figure 1.5). [15,18]

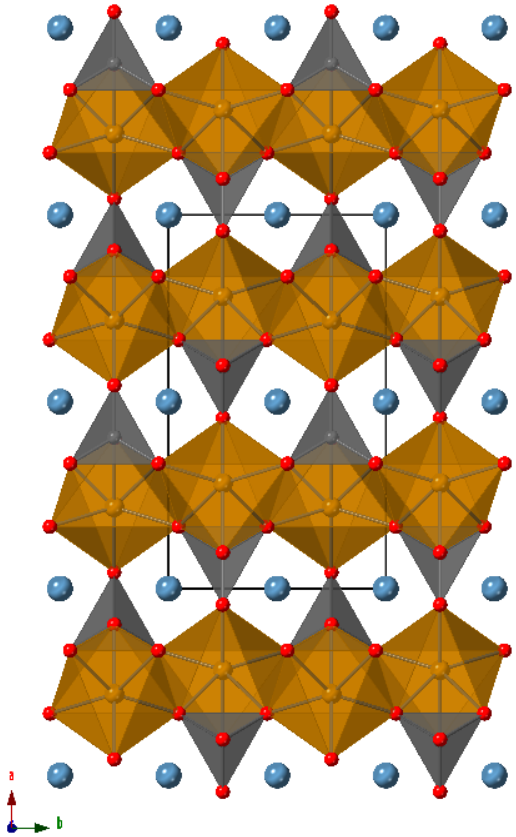

Figure 1.5 Structure of $LiFePO_4$ viewed along the c-axis. Fe octahedra are shown in brown, P tetrahedra shown in grey, O atoms in red and Li atoms in pale blue. The unit cell is outlined in black.

Electrochemical cycling revealed a voltage of 3.5V (vs. Li/Li^+) with approximately 0.6 lithium atoms per formula unit being reversibly deintercalated. Though the phase formed from delithiation ($FePO_4$) has the same crystal symmetry as the lithiated phase, there is a small reduction in unit cell volume (~ 7%). $LiFePO_4$ has very low conductivity at room temperature, therefore, only achieves close to theoretical capacity at very low current density or at higher temperatures. In order to overcome inherent poor electronic conduction

of both $LiFePO_4$ and $FePO_4$, $LiFePO_4$ has been synthesised as nanoparticles coated in electronically conductive carbon. Cathodes produced from such material exhibited initial discharge capacities of 165 mAh/g with no capacity fading over 100 cycles. As with spinel oxides, increasing electrical conductivity has also been investigated by partial substitution of Fe by Nb^{5+}, Mg^{2+}, Al^{3+}, Ti^{4+} and W^{6+}.[16,18,19]

Silicates

In the last decade, cathodes based on orthosilicates of general formula Li_2MSiO_4 (M = Mn, Fe, Co) have been the centre of much research with the iron analogue being the most investigated due the abundance and low cost of iron and silicone. Several polymorphs exist for the structure, in the β_{II} polymorph all the tetrahedra point in the same direction giving it an orthorhombic structure in space group *Pmn*2_1 (Figure 1.6). The polymorphs synthesised at higher temperatures show inversion of half the tetrahedral sites, resulting in distortions of the FeO_4 tetrahedra as they go from vertex sharing to edge-sharing with the LiO_4 tetrahedra.[20,21]

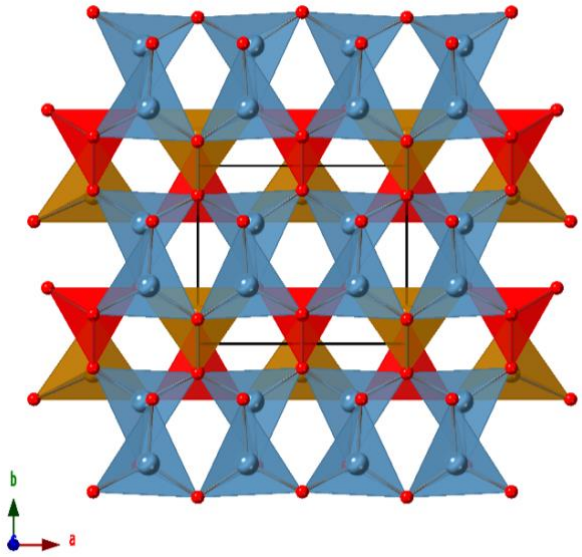

Figure 1.6 Structure of the β_{II} polymorph of Li_2FeSiO_4 viewed along the c-axis. Fe tetrahedra are shown in brown, Si tetrahedra shown in red, Li tetrahedra shown in pale blue and O atoms shown in red. The unit cell is outlined in black.

The dependence of the electrochemistry on these structural differences was reported by Sirsopananporn *et al.* who confirmed that the shortening of the Fe-O bonds and increased disorder in the high-temperature polymorphs showed a lowering of the Fe^{2+}/Fe^{3+} potentials vs Li+/Li and cyclability. Similar observations were seen for the manganese and cobalt analogues with structural changes between polymorphs during cycling of electrodes

resulting in significant capacity fading.[20,21] Zhang *et al*. have improved the cyclability and electrochemical performance of Li_2FeSiO_4 by combining nanocrystallites with an ordered mesoporous carbon (CMK-3).[22]

Tavorites

Tavorites of general formula $AMXO_4Y$ (A = alkali metal, M = transition metal, X = P/S, Y = OH/F) are named after their isostructural naturally occurring counterpart $LiFePO_4(OH)$. Barker *et al*. synthesised four of the lithium transition metal fluorophosphate phases, $LiMPO_4F$ (M = Fe, Ti, Co, Cr) but did not report any electrochemical properties.[23] The structure is comprised of a three-dimensional network of interconnected FeO_4F_2 octahedra and PO_4 tetrahedra with lithium cations in the inter framework space (Figure 1.7). As with the olivines, tavorites show good stability due to the covalent bonding nature of PO_4 but suffer from low energy density. The inclusion of fluorine increases the volume and dimensionality of the lithium diffusion pathways, therefore increasing ionic conductivity.[24,25]

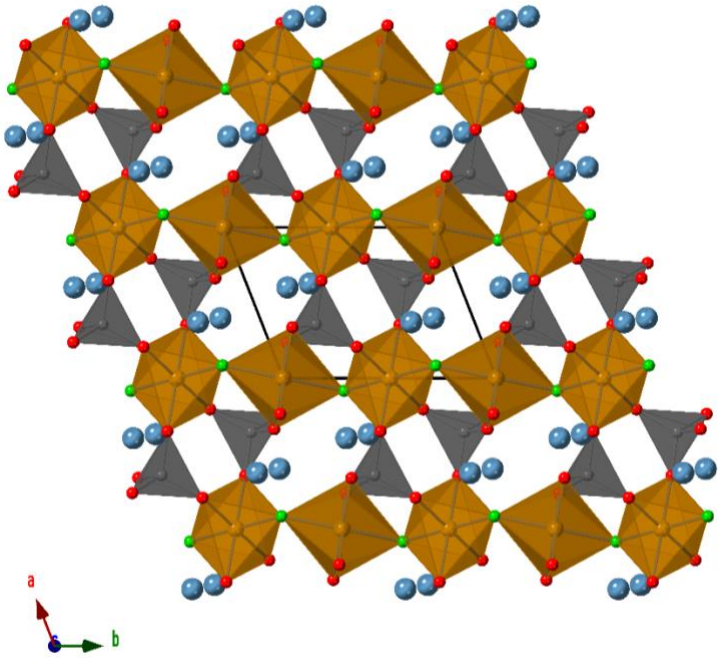

Figure 1.7 Structure of $LiFePO_4F$ viewed along the c-axis. Fe octahedra are shown in brown, P tetrahedra shown in grey, O atoms shown in red, F atoms shown in green and Li atoms shown in pale blue. The unit cell is outlined in black.

The iron fluorosulfate tavorite-type and triplite-type structures $LiFeSO_4F$ has also been analysed for its electrochemical performance and ion conductivity, as it has previously been shown that the open-circuit voltage can be improved from swapping the PO_4^{3-} unit for

SO_4^{2-} with only a small decrease in the energy density.[26] Triplite-type $LiFeSO_4F$ (Figure 1.8) has been grown from tavorite-type and shown similar energy densities to $LiFePO_4$, with very high voltage for an iron-containing compound, making it a strong contender for use as a cathode material in lithium-ion batteries.[26–28]

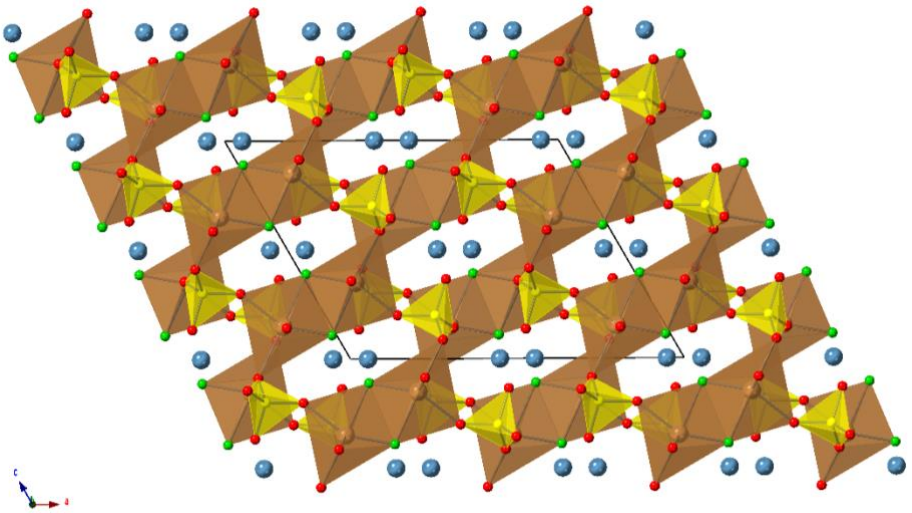

Figure 1.8 Structure of triplite-$LiFeSO_4F$ viewed along the b-axis. Fe octahedra are shown in brown, S tetrahedra shown in yellow, O atoms shown in red, fluorine atoms shown in green and lithium atoms shown in light blue. The unit cell is outlined in black.

Borates

Lithium transition metal borates of general formula $LiMBO_3$ (M = Mn, Fe, Co) are of interest as cathode materials due to higher theoretical energy density over other polyanionic materials. The structure comprises of a three-dimensional framework of interconnected FeO_5 trigonal bipyramids and BO_3 trigonal planes (Figure 1.9). The lithium ions occupy tetrahedral holes in the inter-framework space. Initial cycling at room temperature did not achieve the full theoretical capacity but subsequent investigations have improved the performance of this material by the exclusion of air and moisture from all processing steps, resulting in a 2.8 - 3.2V potential and 190 mAh/g reversible capacity.[25,29,30]

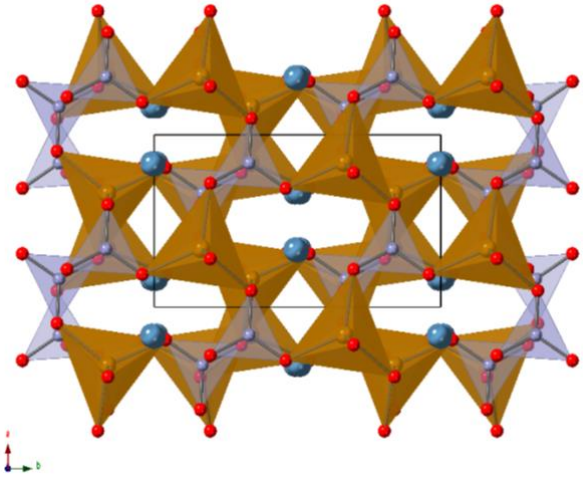

Figure 1.9 Structure of $LiFeBO_3$ viewed along the c-axis. Fe trigonal bipyramids are shown in brown, B trigonal planes shown in lilac, O atoms shown in red and lithium atoms shown in pale blue. The unit cell is outlined in black.

1.1.2.2 Anode material development

To tailor the performance of lithium-ion batteries as a whole, the properties of the anode material have also been widely investigated, with special focus on developing very high-capacity anodes. The discovery of carbonaceous anode materials led the way for replacement of lithium metal anodes and became the first anode material of choice for lithium-ion batteries.[12]

Graphite

Going back to the Sony cell commercialised in 1991, the anode utilised layered graphite, C_6, which is reversibly electrochemically intercalated with lithium to form Li_xC_6 ($x < 1$) during charging. Though this offers advantages in terms of safety of the battery by avoiding lithium dendrite formation, capacity is greatly reduced with 372 mAh/g for LiC_6 compared with 3860 mAh/g for Li. Another issue with graphite is the co-intercalation of solvent molecules which exfoliate the graphite layers, advancing battery failure. This can be counteracted by surface modification with, for example, lithium carbonate or oxalaborates but subsequent expansion and contraction of the graphite layers forms crack in the solid-electrolyte interface (SEI), allowing reaction with the liquid electrolyte. [31]

Graphene

The two-dimensional nanomaterial graphene has a very large surface area and excellent electronic conductivity. It can be produced from exfoliation of graphite and shows an equivalent capacity of 744 mAh/g, due to the ability for the lithium ions to absorb on both sides of the layer. Unfortunately, the large surface area which gives such good absorption

also has the drawback of a large SEI (solid electrolyte interface) formation resulting in a large hysteresis in the potential-capacity curve. Utilising graphene as an additive in composite electrodes can improve the electrochemical properties of other materials. [31,32]

Li alloys

Zintl phases or Li_xSn alloys can be formed electrochemically through a series of plateaus less than 1 V. Nanocrystallinity or amorphous particles show much better stability than the crystalline tin counterparts and offers a specific capacity value of 990 mAh/g. This in combination with low toxicity and cost makes nanocrystalline or amorphous tin a promising anode material. Unfortunately, nanoparticles of tin tend to lower their surface energy by the formation of aggregates which can lead to quick capacity fading. Formation of composite anodes whereby the tin nanoparticles are suspended in a carbonaceous matrix may offer the solution to the aggregation problem and maintaining high capacity.[31]

Ti oxides

In early anode development, titanium oxides were discounted as the drive to use anode materials with a working potential as close as possible to lithium metal was achievable with carbonaceous materials. However, lithium salt/organic solvent electrolytes are not stable in the working voltage range of the graphite anodes. The working potential of TiO_2 is approximately 1.5 V above the Li^+/Li redox couple therefore safety concerns over side reactions with electrolyte are negated. Bulk crystalline rutile-TiO_2 shows poor lithium diffusion which can be improved upon by using nanostructured and anatase-TiO_2 material for the anode. Self-assembled TiO_2 nanotubes have been utilised in combination with tin and Fe_2O_3 to give capacities of 675 and 468 mAh/g respectively.[31,33] Jia *et al*. have reported exceptional electrochemical performance exhibited by carbon-coated, europium doped hierarchical mesoporous lithium titanate: $Li_{4-x/2}Ti_{5-x/2}Eu_xO_{12}$@C ($x$ = 0.004) with capacity maintained at 173.4 mAh/g after an initial discharge capacity of 198.7 mAh/g and 1000 subsequent cycles.[34]

Polyanionic compounds

The use of polyanionic compounds such as lithium titanyl phosphate (LTP) : $LiTi_2(PO_3)_3$ as anodes in combination with aqueous electrolytes has been tested and shown promising capacity of 113 – 115 mAh/g with over 80% capacity retention over 100 cycles.[35]

1.1.3 Sodium-ion batteries

A move away from lithium towards sodium technology occurred recently, in order to investigate the capability of a system whose main components comprise of highly abundant and therefore low-cost materials with reliable supply chains, all of which are highly favourable factors for larger scale energy storage such as powering electric vehicles and national grid storage.[36]

The development of suitable cathode materials for sodium-ion batteries has followed a similar pattern to that of the lithium-ion batteries, with sodium analogues of many materials previously used for lithium-ion batteries. Generally, these sodium analogues show lower operating potentials compared with their lithium counterparts. This is often attributed to the larger ionic radius of sodium in comparison to lithium causing greater volume changes on charging cycles.[36]

1.2 Aims and objectives/Scope of work

With the promise shown by sodium and lithium-containing transition metal fluorophosphate and fluorosulfate frameworks as functional materials, the main aim of this PhD research project is the implementation of high fluoride hydrothermal and ceramic syntheses to obtain novel fluoride-containing transition metal framework materials and their characterisation via single-crystal X-ray diffraction.

1.2.1 Titanium

Though a few titanium fluorophosphate structures have been previously reported and their electrochemical properties investigated, titanium fluorosulfate frameworks have proven elusive due to stability issues. Therefore, the initial objective of this project is to further investigate both the titanium fluorophosphate and fluorosulfate systems to obtain novel fluoride-containing framework structures with open frameworks to promote high ion transport capacity. This has been achieved with the use of high fluoride precursors such as TiF_3, TiF_4, H_2TiF_6 and K_2TiF_6. The results from this investigation are covered in Chapters three and four, where ten new titanium-containing structures are described.

1.2.2 Manganese

Manganese frameworks have been heavily researched over the years, but relatively few mixed cation and/or mixed polyanion frameworks have been reported. The second focus of this research is to investigate mixed cation and mixed polyanion manganese phosphate and sulfate-containing framework materials. The mixed cation part of this work is a part of a masters student's final year project completed under the supervision of the author and is presented in Chapter five sections 5.1 - 5.3. Results from the mixed polyanion work are presented in Chapter 5 section 5.4 - 5.5.

1.2.3 Other transition metals and lanthanides

Finally, though the drive towards cheap and sustainable metals such as iron and manganese has taken precedence in a vast amount of functional material research to date, lanthanides are still of interest in Ni-MH batteries and offer a much greater variety of possible frameworks due to the larger ionic radius and valency. Additionally, other transition metals such as vanadium, chromium and yttrium have proven to be of interest in functional materials, either as the sole redox centre or as dopant cations. As such, the final focus of this research was the vanadium/chromium/yttrium/lanthanide fluorosulfate system. The results of this final effort are presented in Chapter six, where four new structures are described.

1.3 References

(1) Akimitsu, M.; Mizoguchi, T.; Akimitsu, J.; Kimura, S. Magnetic Structure and Magnetic Properties of Non-Stoichiometric Fe1-XO. *J. Phys. Chem. Solids* **1983**, *44* (6), 497–505.

(2) Press, M. R.; Ellis, D. E. Defect Clusters in Wustite Fe1-XO. *Phys. Rev. B* **1987**, *35* (9), 4438–4454.

(3) Hu, Y. S.; Kienle, L.; Guo, Y. G.; Maier, J. High Lithium Electroactivity of Nanometer-Sized Rutile TiO_2. *Adv. Mater.* **2006**, *18* (11), 1421–1426.

(4) Weller, M. T. *Inorganic Materials Chemistry*; Evans, J., Ed.; Oxford University Press: Oxford, 1994.

(5) Jang, W.; Yun, J.; Lee, T.; Lee, Y.; Soon, A. Disentangling the Effects of Inter- and Intra-Octahedral Distortions on the Electronic Structure in Binary Metal Trioxides. *J. Phys. Chem. C* **2018**, *122* (6), 3558–3566.

(6) Attfield, J. P.; Lightfoot, P.; Morris, R. E. Perovskites. *Dalt. Trans.* **2015**, *44* (23), 10541–10542.

(7) Ferg, E.; Gummow, R. J.; Kock, A. De. Spinel Anodes for Lithium-Ion Batteries. *J. Electrochem. Soc.* **1994**, *141* (11), L147–L150.

(8) Nanjundaswamya, K.; Padhi, A.; Goodenough, J.; Okada, S.; Ohtsukab, H.; Arai, H.; Yamakib, J. Synthesis, Redox Potential Evaluation and Electrochemical Characteristics of NASICON-Related-3D Framework Compounds. *Solid State Ionics* **1996**, *92*, 1–10.

(9) Sarakonsi, T.; Kumar, R. V. Primary Batteries. In *High Energy Density Lithium Batteries*; Aifantis, K. E., Hackney, S. A., Kumar, R. V., Eds.; Weimheim : Wiley-VCH, 2010; pp 27–52.

(10) Tirado, J. L. Inorganic Materials for the Negative Electrode of Lithium-Ion Batteries: State-of-the-Art and Future Prospects. *Mater. Sci. Eng. R Reports* **2003**, *40* (3), 103–136.

(11) Kumar, R. V.; Sarakonsri, T. A Review of Materials and Chemistry for Secondary Batteries. In *High Energy Density Lithium Batteries*; Aifantis, K. E., Hackney, S. A., Kumar, R. V., Eds.; Weimheim : Wiley-VCH, 2010; pp 53–80.

(12) Choi, D.; Wang, W.; Yang, Z. Material Challenges and Perspectives. In *Lithium-Ion Batteries Advanced Materials and Technologies*; Yuan, X., Liu, H., Zhang, J., Eds.; Green Chemistry and Chemical Engineering; CRC Press, 2012; pp 1–50.

(13) Mizushima, K.; Jones, P. C.; Wiseman, P. J.; Goodenough, J. B. $LixCoO_2$ ($0<x<1$): A New Cathode Material for Batteries of High Energy Densities. *Solid State Ionics* **1981**, *15* (6), 783–789.

(14) Thackeray, M. M. Lithiated Oxides for Lithium Ion Batteries. *J. Electrochem. Soc.* **1995**, *142* (8), 2558–2563.

(15) Bakenov, Z.; Taniguchi, I. Cathode Materials for Lithium-Ion Batteries. In *Lithium-Ion Batteries Advanced Materials and Technologies*; Yuan, X., Liu, H., Zhang, J., Eds.; CRC Press, 2012; pp 51–96.

(16) Whittingham, M. S. Lithium Batteries and Cathode Materials. *Chem. Rev.* **2004**, *104* (10), 4271–4301.

(17) Gutierrez, A.; Manthiram, A. Understanding the Effects of Cationic and Anionic Substitutions in Spinel Cathodes of Lithium-Ion Batteries. *J. Electrochem. Soc.* **2013**, *160* (6), 901–905.

(18) Padhi, A. K.; Nanjundaswamya, K. S.; Goodenough, J. B. Phospho-Olivines as Positive-

Electrode Materials for Rechargeable Lithium Batteries. *J. Electrochem. Soc.* **1997**, *144* (4), 1188–1194.

(19) Bakenov, Z.; Taniguchi, I. Cathode Materials for Lithium-Ion Batteries. In *Lithium-Ion Batteries Advanced Materials and Technologies*; Yuan, X., Liu, H., Zhang, J., Eds.; Green Chemistry and Chemical Engineering; CRC Press, 2012; pp 51–96.

(20) Sirisopanaporn, C.; Masquelier, C.; Bruce, P. G.; Armstrong, A. R.; Dominko, R. Dependence of Li_2FeSiO_4 Electrochemistry on Structure. *J. Am. Chem. Soc.* **2011**, *133* (5), 1263–1265.

(21) Islam, M. S.; Dominko, R.; Masquelier, C.; Sirisopanaporn, C.; Armstrong, A. R.; Bruce, P. G. Silicate Cathodes for Lithium Batteries: Alternatives to Phosphates? *J. Mater. Chem.* **2011**, *21* (27), 9811–9818.

(22) Qiu, H.; Zhu, K.; Li, H.; Li, T.; Zhang, T.; Yue, H.; Wei, Y.; Du, F.; Wang, C.; Chen, G.; Zhang, D. Mesoporous Li_2FeSiO_4 ordered Mesoporous Carbon Composites Cathode Material for Lithium-Ion Batteries. *Carbon N. Y.* **2015**, *87* (C), 365–373.

(23) Barker, J.; Gover, R. K. B.; Burns, P.; Bryan, A. J. Hybrid-Ion A Lithium-Ion Cell Based on a Sodium Insertion Material. *Electrochem. Solid-State Lett.* **2006**, *9* (4), A190–A192.

(24) Recham, N.; Chotard, J. N.; Jumas, J. C.; Laffont, L.; Armand, M.; Tarasco, J. M. Ionothermal Synthesis of Li-Based Fluorophosphates Electrodes. *Chem. Mater.* **2010**, *22*, 1142–1148.

(25) Xu, B.; Qian, D.; Wang, Z.; Meng, Y. S. Recent Progress in Cathode Materials Research for Advanced Lithium Ion Batteries. *Mater. Sci. Eng. R Reports* **2012**, *73* (5–6), 51–65.

(26) Tripathi, R.; Gardiner, G. R.; Islam, M. S.; Nazar, L. F. Alkali-Ion Conduction Paths in $LiFeSO_4F$ and $NaFeSO_4F$ Tavorite-Type Cathode Materials. *Chem. Mater.* **2011**, *23* (8), 2278–2284.

(27) Melot, B. C.; Rousse, G.; Chotard, J. N.; Ati, M.; Rodríguez-Carvajal, J.; Kemei, M. C.; Tarascon, J. M. Magnetic Structure and Properties of the Li-Ion Battery Materials $FeSO_4F$ and LiFeSO4F. *Chem. Mater.* **2011**, *23* (11), 2922–2930.

(28) Ati, M.; Sathiya, M.; Boulineau, S.; Reynaud, M.; Abakumov, A.; Rousse, G.; Melot, B.; Van Tendeloo, G.; Tarascon, J. M. Understanding and Promoting the Rapid Preparation of the Triplite -Phase of $LiFeSO_4F$ for Use as a Large-Potential Fe Cathode. *J. Am. Chem. Soc.* **2012**, *134* (44), 18380–18387.

(29) Yamada, A.; Iwane, N.; Harada, Y.; Nishimura, S.; Koyama, Y.; Tanaka, I. Lithium Iron Borates as High-Capacity Battery Electrodes. *Adv. Mater.* **2010**, *22* (32), 3583–3587.

(30) Janssen, Y.; Middlemiss, D. S.; Bo, S. H.; Grey, C. P.; Khalifah, P. G. Structural Modulation in the High Capacity Battery Cathode Material $LiFeBO_3$. *J. Am. Chem. Soc.* **2012**, *134* (30), 12516–12527.

(31) Alcántara, R.; Lavela, P.; Pérez-Vicente, C.; Tirado, J. Anode Materials for Lithium-Ion Batteries. In *Lithium-Ion Batteries Advanced Materials and Technologies*; Yuan, X., Liu, H., Zhang, J., Eds.; Green Chemistry and Chemical Engineering; CRC Press, 2012; pp 97–146.

(32) Huang, Y.-H.; Bao, Q.; Duh, J.-G.; Chang, C.-T. Top-down Dispersion Meets Bottom-up Synthesis: Merging Ultranano Silicon and Graphene Nanosheets for Superior Hybrid Anodes for Lithium-Ion Batteries. *J. Mater. Chem. A* **2016**, *4*, 9986–9997.

(33) Zhu, G.-N.; Wang, Y.-G.; Xia, Y.-Y. Ti-Based Compounds as Anode Materials for Li-Ion Batteries. *Energy {&} Environ. Sci.* **2012**, *5* (5), 6652.

(34) Cai, Y.; Huang, Y.; Jia, W.; Wang, X.; Guo, Y.; Jia, D.; Sun, Z.; Pang, W.; Guo, Z. Super High-Rate, Long Cycle Life of Europium-Modified, Carbon-Coated, Hierarchical Mesoporous Lithium-Titanate Anode Materials for Lithium Ion Batteries. *J. Mater. Chem. A* **2016**, *4* (25), 9949–9957.

(35) Wessells, C.; Mantia, F. La; Deshazer, H.; Huggins, R. A.; Cui, Y. Synthesis and Electrochemical Performance of a Lithium Titanium Phosphate Anode for Aqueous Lithium-Ion Batteries. *J. Electrochem. Soc.* **2011**, *158* (3), A352–A355.

(36) Wang, L. P.; Yu, L.; Wang, X.; Srinivasan, M.; Xu, Z. J. Recent Developments in Sodium-Ion Batteries. *J. Mater. Chem. A* **2015**, *3*, 9353–9378.

Chapter 2 : Experimental techniques

2.0 Introduction

The synthetic and analytical methods employed in this work are typical for the synthesis and characterisation of novel inorganic materials. Solid-state and hydrothermal synthesis methods were heavily employed as the methods of choice, with emphasis on the hydrothermal method due to the desire to produce inorganic framework materials with the capability of ion transport. Analysis of synthetic products was completed with powder X-ray diffraction (PXRD) in the first instance to identify known phases, and also to analyse phase purity of produced samples.

Single crystal X-ray diffraction (SXRD) was the primary analytical technique used as this characterised the crystal structures of new materials synthesised. Scanning electron microscopy (SEM) in combination with energy dispersive X-ray analysis (EDX) gave insight into the morphology and confirmed the elemental composition of select microcrystals.

2.1 Synthetic Methods

When attempting to synthesise solid inorganic materials, the choice of synthetic method plays an important role in determining the form of the products. For unknown structure determination crystals big enough to collect SXRD data are the desired form but for actual applications, other forms such as powders or solid monoliths may have more desirable bulk properties. As this project focused on the synthesis of novel inorganic framework materials, the synthetic methods employed are well known to produce crystalline products. These methods are high-temperature solid-state reactions and hydrothermal or solvothermal synthesis.

2.1.1 Solid-state synthesis

The solid-state reaction is a very commonly used method for synthesis of inorganic materials, including complex oxides, fluorides, phosphates, silicates and sulphides. It involves heating stoichiometric ratios of dry-powder (microcrystalline) starting materials possessing the desired elements (usually binary oxides-due to commercial availability) to very high temperatures (500 -2000 °C). The starting reagents are ground together with a pestle and mortar (or in a ball mill), often pressed into a pellet and transferred to a crucible made of inert material such as silica, alumina or platinum. The crucible containing the solid reaction mixture/pellet is placed in a furnace at a sufficiently high temperature to promote ion migration through crystal face contacts at the grain boundaries within the mixture. This is a structurally disruptive process, which normally involves the migration of

the smaller cations of an oxide. These cations are normally coordinated to multiple oxide anions (increasing in number, the larger the cation), and the energy required to displace them, termed the lattice energy, is quite high. The lattice energy depends on the charge to radius ratio and hence the ionic attraction to the lattice. Small charge to radius ratio ions (e.g. alkali metals) have a weak attraction to the lattice (small lattice energy) and so will react at lower temperatures. Conversely, smaller highly charged ions (large charge to radius ratio) are much more attracted to the lattice (higher lattice energy) and require much higher temperatures.[1,2]

Though increasing the temperature will speed up the reaction time needed to form the new phase, there is a limit to how high the temperature can be raised. This limit is the point at which the solid reaction mixture melts, and though the ions will become highly mobile, crystallisation of a molten reaction mixture rarely results in the desired product. Instead, the reaction rate can be increased by increasing the number of crystal interfaces, which can be achieved through smaller particles sizes, homogenous mixing (and re-mixing throughout the reaction process) and pressing the reaction mixture into a pellet using a hydraulic press (this reduces the void space). [1,2]

When grinding does not provide small enough particles (less than 0.1 μm) precursors which decompose during the heating process can be employed. For example, metal carbonates, hydroxides and nitrates will decompose, releasing gaseous species and leaving behind fine reactive powders which increase the reaction rates. In addition, precursors are usually more air-stable than their oxide counterparts, making it much easier to weigh stoichiometric reaction mixtures. [2]

Solutions are employed to gain greater homogeneity in reaction mixtures but precipitation from solution does not always yield the stoichiometric solid desired. This is often overcome with gel methods which involve turning the solution into gel via complexation and/or the loss of water. The gel can then be heated in a crucible at a lower temperature and for significantly less time than the direct reaction of solid oxides.[2]

High-temperature reactions can be carried out under controlled atmospheres in a tube furnace. This is useful to control reaction stoichiometry and oxidation state by passing inert gases or hydrogen over the heated reaction mixture. If any of the reagents are volatile at the reaction temperature, the reaction mixture can be sealed under vacuum in a sealed

glass tube before heating, thus preventing loss of reagents and subsequent impurities caused by non-stoichiometry.[2]

2.1.2 Hydrothermal synthesis

The hydrothermal technique is an extension of the solution based solid-state synthesis mentioned above and was used extensively in this research as it is a favoured method for the synthesis of inorganic framework materials such as zeolites, phosphates and sulphates. The technique was developed from an understanding of the natural process by which minerals form in the earth's crust due to elevated temperature and pressure of water. Much of the early synthetic work aimed to produce minerals already occurring naturally, until Barrer produced the first zeolite without a natural equivalent in 1948, this was the beginning of molecular sieves and using the technique to grow crystals with new structures, not previously seen in nature. The hydrothermal technique is also a useful tool in the synthesis of nanomaterials and metal extraction. [2,3]

There are numerous apparatus designs for the hydrothermal reaction technique, but they all revolve around heating the reaction mixture to above ambient temperature and pressure. For this work, 23mL capacity Teflon-lined steel Parr acid-digestion autoclaves as shown in Figure 2.1 were used. The reaction mixture is sealed in the autoclave and placed in an oven at the desired temperature, an autogenous pressure is generated within the sealed autoclave and crystallisation from solution occurs at much lower temperatures than the traditional solid-state methods mentioned above. The maximum operating temperature and pressure of the Teflon lined Parr autoclave is 250 °C and 1800 psi.

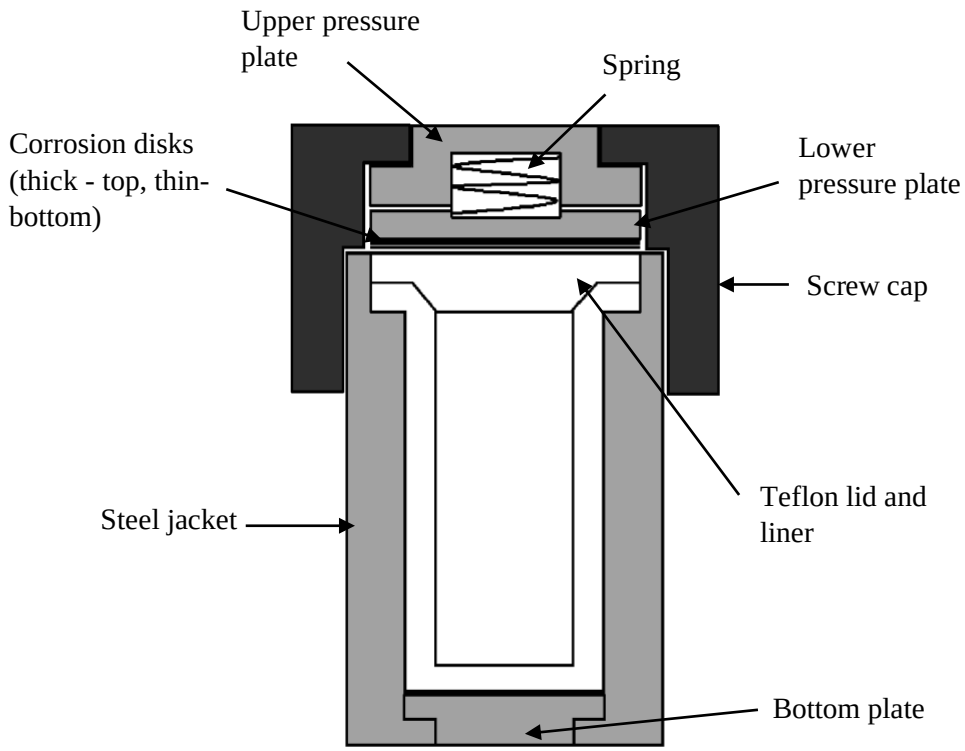

Figure 2.1 Diagram of a Teflon-lined steel Parr autoclave

When solvents other than water (e.g. alcohols and organic solvents) are employed in this method, the technique is termed solvothermal synthesis. As the principle of solvo/hydrothermal synthesis is to increase the rate of reaction by heating the mixture to just above the boiling point of the solvent in use, lower reaction temperatures can be achieved because the temperatures of organic solvent mixtures can be lower than those of water. The pressure created by the solvent transitioning to the vapour phase allows insoluble reagents to become soluble and more reactive, thus driving the reaction forward. The major advantage of the solvo/hydrothermal method over the solid-state method is the fast growth of crystals achieved due to greater ion mobility in solution and the ability to access kinetic products over thermodynamic ones favoured in solid-state synthesis.

The major disadvantage to this method is the difficulty in determining the reaction mechanism which takes place with the sealed vessel. Many variables have been found to have profound effects on the reaction product obtained; these include temperature, starting pH, time of reaction and concentration of reagents prior to reaction. In previous syntheses of fluoride-containing frameworks it was found that OH^- binds competitively with F^- to transition metals, so in order to obtain high fluoride-containing frameworks water is excluded as much as possible. [4–7]

2.2 Analytical techniques

Analytical chemistry is at the heart of understanding the chemical world around us. To a solid-state materials chemist, the analytical tools of choice for structure determination begin with X-ray diffraction techniques (both single crystal and powder) due to the ability to accurately plot atomic positions within the solid-state. Where information from X-ray diffraction is lacking, neutrons can be employed for clarity. And once the structure is known, properties can be investigated using a multitude of analytical techniques such as UV/Vis and IR spectroscopy and thermogravimetric analysis.

X-ray diffraction was employed heavily during the research work of this thesis. Each reaction product was first checked for crystal formation and a sample analysed by powder X-ray diffraction (PXRD) to check for known phases. If the structure was determined to be unknown by PXRD single crystal X-ray diffraction (SXRD) was used to determine the crystal structure. The phase purity of new materials was checked by a comparison of PXRD with simulated patterns from the SXRD data.

Scanning electron microscopy (SEM) in combination with energy dispersive X-ray microanalysis (EDX) was utilised to study morphology and elemental composition of microcrystals.

2.2.1 X-ray Diffraction theory

X-rays were first discovered in 1895 by Wilhelm Röntgen, and diffraction of X-rays by crystals first noted by Max von Laue in 1912. [8,9] The Laue equations describe the diffraction of incident waves by a crystal lattice and were further simplified by William L Bragg and William H. Bragg in 1913.

Electrons scatter X-rays elastically, without a change in energy, and diffraction occurs when X-rays are scattered by a periodic array of electron containing atoms (scattering centres) with separation distances similar to the wavelength of the radiation (~ 100 pm, 1Å). The interference of scattered X-rays from a crystalline material gives rise to a number of diffraction maxima, which is called a diffraction pattern. Unlike spectroscopic techniques, X-ray diffraction uses monochromatic radiation and measures the variation in the intensity of the scattered X-rays in relation to the direction/orientation of the crystalline material being studied.[10,11]

Crystals diffract X-rays because a crystal is a solid material comprising of a regular array of atoms or ions which repeats infinitely in all directions. The unit cell is a parallelepiped

defined by six cell/lattice parameters; lengths *a*, *b* and *c* and angles *α, β and γ* as depicted in Figure 2.2.

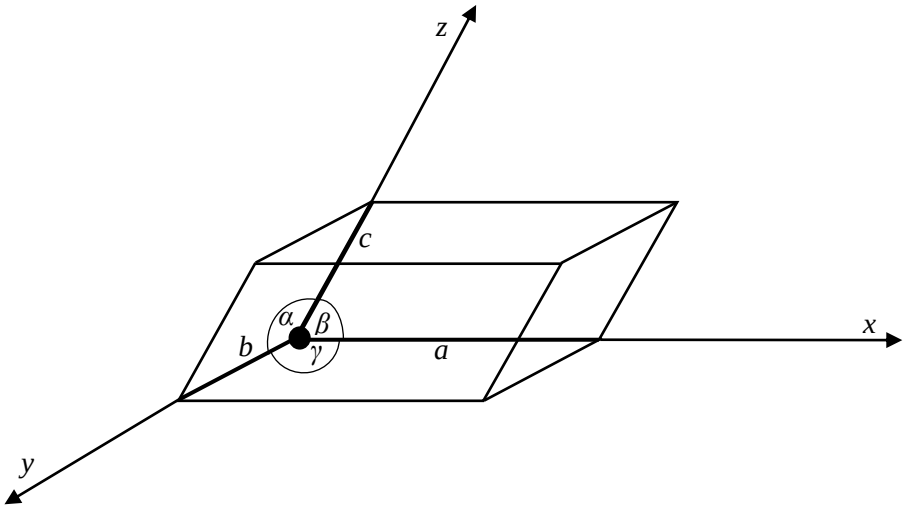

Figure 2.2 The unit cell as defined by the lattice parameters *a*,*b*,*c*, *α*, *β*, and *γ*

Translational repetition of the unit cell along the three axes *x*, *y* and *z* builds up the space-filling structure of the entire crystal, hence the unit cell is the smallest repeat unit of the crystal structure and is usually chosen to exhibit the most symmetry. Seven crystal systems are used to describe the relationship between the lattice parameters and the symmetry of the structure, these are given in Table 2.1.

The highest symmetry system is cubic, in which the lattice parameter lengths are equal and all the angles equal to 90°, the symmetry reduces for each system all the way to triclinic, in which all the lattice parameters are un-related. The only symmetry present in all seven crystal systems is the translational symmetry of the unit cell along the *x*, *y*, *z*-axes (Figure 2.2). This symmetry is a feature of the lattice, which is defined as an array of equivalent points (lattice points), in the case of crystals, in three dimensions.

Table 2.1 The seven crystal systems

Crystal System	**Lattice Parameters**	**Point Group**	**Bravais Lattice**
Triclinic	$a \neq b \neq c$ $\alpha \neq \beta \neq \gamma \neq 90°$	1, $\bar{1}$	P
Monoclinic	$a \neq b \neq c$ $\alpha = \gamma \neq 90° \beta \neq 90°$	2/*m*, *m*, 2	P C
Orthorhombic	$a \neq b \neq c$ $\alpha = \beta = \gamma = 90°$	*mmm*, *mm*2, 222	P C I F
Tetragonal	$a = b \neq c$ $\alpha = \beta = \gamma = 90°$	4/*mmm*, $\bar{4}$2*m*, 4*mm*, 422, 4/*m*, $\bar{4}$, 4	P I
Trigonal/Rhombohedral	$a = b = c$ $\alpha = \beta = \gamma \neq 90°$	$\bar{3}$*m*, 3*m*, 32, $\bar{3}$, 3	P
Hexagonal	$a = b \neq c$ $\alpha = \beta = 90° \gamma = 120°$	6/*mmm*, $\bar{6}$*m*2, 6*mm*, 622, 6/*m*, $\bar{6}$, 6	P
Cubic	$a = b = c$ $\alpha = \beta = \gamma = 90°$	*M*$\bar{3}$*m*, $\bar{4}$3*m*, 432, *m*$\bar{3}$, 23	P I F

The seven crystal systems can be further divided into 14 Bravais lattices (Table 2.1), of which there are four distinct types (depicted in Figure 2.3). The simplest of these lattice types are named primitive (P) and contains only one lattice point, usually placed on the corner or origin of the unit cell, giving equivalent lattice points on all the corners. The second lattice type is named body centred (I) and subsequently has lattice points on all the corners and one in the centre of the unit cell. The third type is an all face centred (F) lattice and has lattice points on all corners and in the centre of all the faces of the unit cell. The fourth lattice type has lattice points on all corners and in the centre of one face of the unit cell, this type is denoted A, B or C depending on which plane the face-centred face lies (A for the *bc* plane, B for the *ac* plane and the most commonly used C for the *ab* plane).

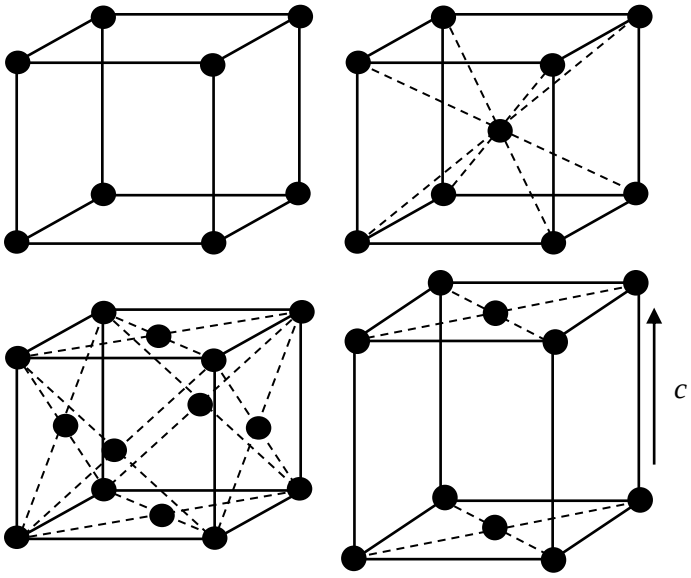

Figure 2.3 Clockwise from top left: primitive cubic unit cell (P), body centred cubic unit cell (I), face centred tetragonal unit cell (C), all face centred cubic unit cell (F)

The combination of symmetry elements for each unit cell gives rise to the 32 crystallographic point groups, these combined with the translational symmetry (14 Bravais Lattices) of the unit cell results in 230 possible space groups which describe the full symmetry of the crystal.

As a crystal can be thought of as a regular array of lattice points in three dimensions, two-dimensional lattice planes can be used to connect the lattice points. Each plane extends infinitely in each direction and belongs to a family of equally spaced planes. These lattice planes are described using Miller indices (*h, k, l*) in three dimensions, which are integer values representative of the intercepts of the plane with the edges of the unit cell. For example, a plane which diagonally bisects the primitive unit cell shown in the top left of Figure 2.3 would have Miller indices of (1,1,0). The separation of the planes is called the d-spacing and given the notation d_{hkl}. The d-spacing can be thought of as the perpendicular distance from the origin of the unit cell to the nearest plane and can be calculated for each of the seven crystal systems as shown in Table 2.2. The equations in Table 2.2 show that d_{hkl} is dependent on the lattice parameters and the crystal system.

Table 2.2 Expressions for d-spacings for the seven crystal systems

Crystal system	*Expression for d (d_{hkl})*
Cubic	$\frac{1}{d^2} = \frac{h^2 + k^2 + l^2}{a^2}$
Tetragonal	$\frac{1}{d^2} = \frac{h^2 + k^2}{a^2} + \frac{l^2}{c^2}$
Orthorhombic	$\frac{1}{d^2} = \frac{h^2}{a^2} + \frac{k^2}{b^2} + \frac{l^2}{c^2}$
Hexagonal	$\frac{1}{d^2} = \frac{4}{3}\left(\frac{h^2 + hk + k^2}{a^2}\right) + \frac{l^2}{c^2}$
Monoclinic	$\frac{1}{d^2} = \frac{1}{\sin^2\beta}\left(\frac{h^2}{a^2} + \frac{k^2 \sin^2\beta}{b^2} + \frac{l^2}{c^2} - \frac{2hl\cos\beta}{ac}\right)$
Triclinic	$\frac{1}{d^2} = h^2\frac{b^2c^2\sin^2\alpha}{V^2} + k^2\frac{a^2c^2\sin^2\beta}{V^2} + l^2\frac{a^2b^2\sin^2\gamma}{V^2} + 2hk\frac{abc^2(\cos\alpha\cos\beta - \cos\gamma)}{V^2} + 2kl\frac{a^2bc(\cos\beta\cos\gamma - \cos\alpha)}{V^2} + 2lh\frac{ab^2c(\cos\gamma\cos\alpha - \cos\beta)}{V^2}$ Where V is the unit cell volume given by: $V = abc(1 - cos^2\alpha - \cos^2\beta - \cos^2\gamma + 2\cos\alpha\cos\beta\cos\gamma)^{1/2}$

When a crystal can be considered as a set of equally spaced parallel lattice planes which contain atoms as shown in Figure 2.4, the diffraction of X-rays by said atoms can be understood in terms of the Bragg equation:

$$2d\sin\theta = n\lambda \qquad \text{Equation 2.1}$$

where n is an integer, λ is the X-ray wavelength and θ is the angle of incidence of the X-ray beam, also known as the Bragg angle. The Bragg equation is derived from the trigonometric relationship between the extra distance travelled by the wave impinging on the lower lattice plane (shown in green in Figure 2.4), the d-spacing between the planes (d_{hkl}) and the angle of impingement of the X-ray beam (θ). To get constructive interference (diffraction) of the scattered waves, the extra distance to the lower lattice point must be an integer number of wavelengths, otherwise, the scattered waves will be out of phase which leads to destructive interference. The accumulation of destructive interference from many

lattice planes within a crystal leads to the sharp/narrow appearance of the diffraction maxima (reflections) generated by the constructive interference.

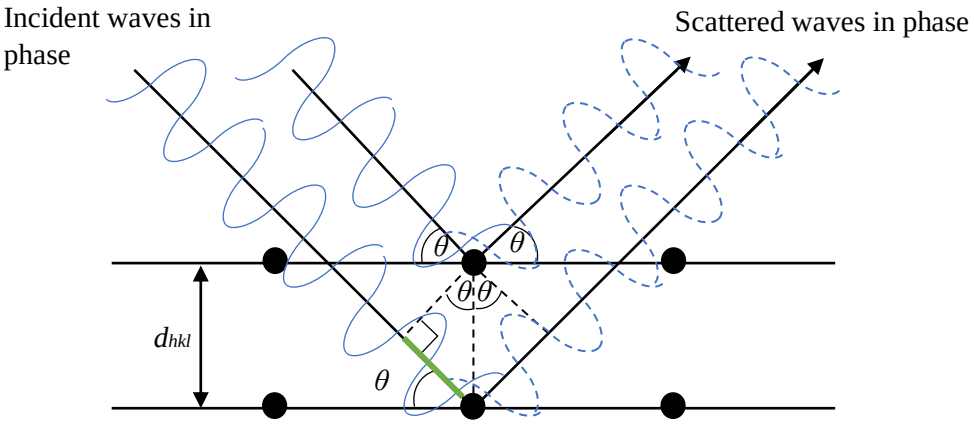

Figure 2.4 Schematic showing derivation of Bragg's law

The angle through with the scattered beam is turned relative to the incident beam is twice that of the Bragg angle and is termed the diffraction angle, as this is what is actually measured in the diffraction experiment.

The position of potential diffraction maxima at a measured diffraction angle (2θ) for a given unit cell/crystal system can be obtained by the combination of the Bragg equation with the expression for the d-spacing. For the cubic crystal system this results in the relationship:

$$\sin^2\theta = \frac{\lambda^2}{4a^2}(h^2 + k^2 + l^2) \qquad \text{Equation 2.2}$$

This gives rise to a large number of possible reflections generated by the scattering of X-rays by a crystal, the positions of which are defined by θ and determined by the lattice parameters, Miller indices and X-ray wavelength. So, by studying the diffraction of X-rays of known wavelengths at known angles to a crystalline solid enables us to calculate the lattice parameters.

2.2.1.1 Powder X-ray Diffraction

A powder sample contains thousands of very small crystallites, generally in the region of 0.1-10 μm in size, all of which randomly adopt a full range of orientations. Hence, an X-ray beam impinging on a polycrystalline sample can be diffracted in all possible directions as determined by the Bragg equation and the d-spacing for all the *h*,*k*,*l* values present within the sample. This means that a cone of diffraction is emitted for each *d*-spacing permitted by the crystal system. Each cone comprises of closely spaced dots which each

represent diffraction from one crystallite within the polycrystalline sample, the more crystallites in the sample the closer these dots are forming the cone.

Historically photographic film sensitive to X-rays was used to capture and measure the diffraction cones emitted from a powder sample, in the form of a Debye-Scherrer camera. In this set up a strip of X-ray sensitive film was placed inside a cylindrical camera with the sample at the centre, usually mounted as a coating on a glass fibre or as the filling of a thin glass capillary. The sample is often rotated around the axis of the fibre to expose as many orientations of the crystallites as possible to the X-ray beam which enter through one side of the camera and is collated onto the sample. After the film is developed it is laid flat and the arcs of the diffraction cones can clearly be seen. Their positions relative to the beam stop in combination with the radius of the camera gives the diffraction angle 2θ for each of the lines.

Modern diffractometers more commonly use scintillation counters to measure the positions of diffracted X-rays (Figure 2.5). Scintillation counters contain detector medium such as sodium iodide doped with thallium which emits a pulse of visible light when struck by X-rays, the intensity of the light is measured and plotted as a function of the 2θ angle. The detector scans a pre-determined 2θ range as the sample plate is rotated at half the speed of the detector, thus cutting through the diffraction cones, generating the two-dimensional diffraction pattern, as shown in Figure 2.6.

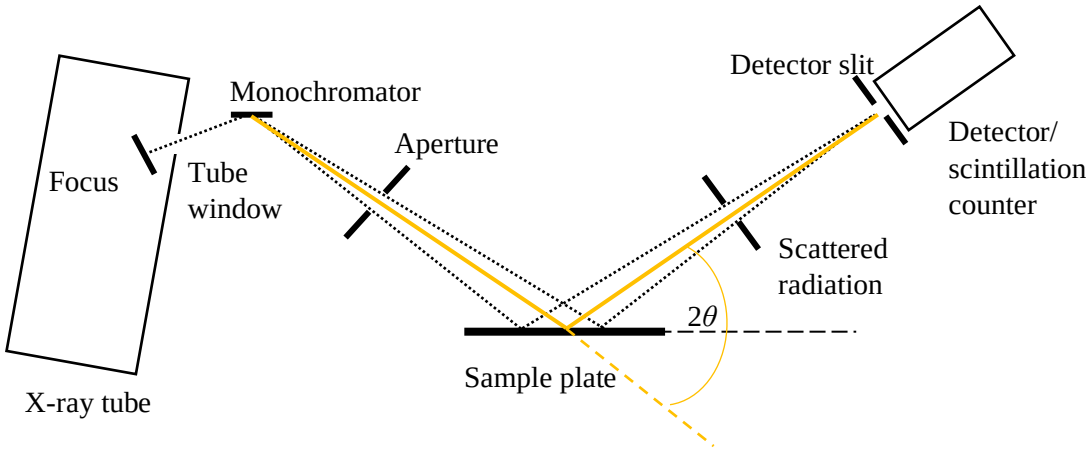

Figure 2.5 Schematic of a powder diffractometer

The PXRD data presented in this work were collected on a Siemens D5000 and a Bruker D8 diffractometer, both fitted with Cu sourced X-ray tubes and germanium monochromators, resulting in X-rays of wavelength λ = 1.54056 Å.

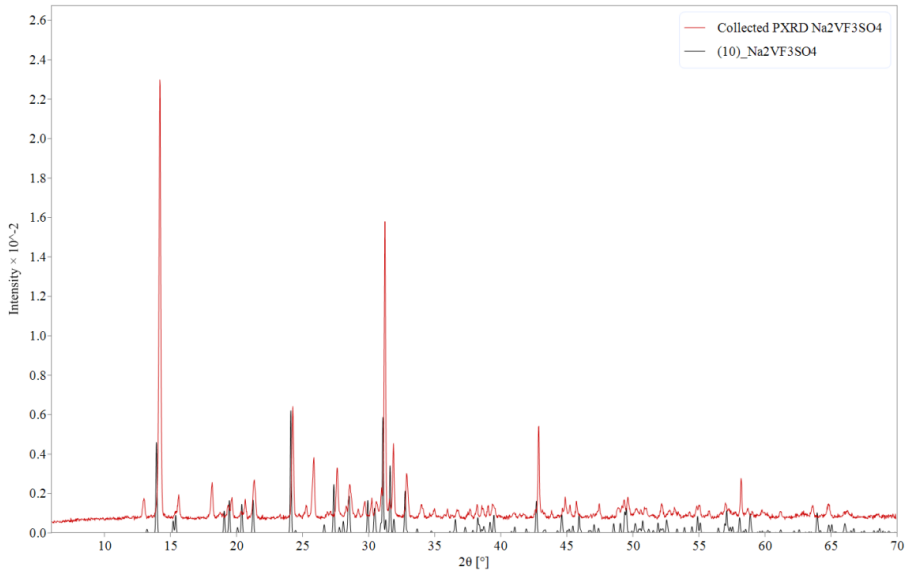

Figure 2.6 Simulated PXRD pattern form SXRD data (black) and collected PXRD data (red) for $Na_2VF_3SO_4$ [12]

The produced PXRD pattern can be used for a wide range of applications, these include: identification of phases both known and unknown, determination of sample purity, particle size determination, refinement of lattice parameters and determination of lattice type, structural refinement, ab initio structure determination, observation of thermal expansion and phase changes and qualitative and quantitative analysis of solid phases. As each compound crystallises with a unique arrangement of atoms within a unique unit cell, a PXRD pattern is generated which is distinctive for that compound and can be used to 'fingerprint' crystalline compounds. PXRD patterns of known compounds (experimentally collected or calculated from known structures) are collated into large databases which can be used to compare to experimentally obtained patterns of unknown samples. The contribution from multiple phases can also be calculated from these comparisons.

The process of identifying the Miller indices for each reflection of a PXRD pattern is known as indexing and is simplest for the cubic crystal system. Equation 2.2 can be simplified as λ and a is constant for the experiment, giving

$$sin^2\theta = A(h^2 + k^2 + l^2) \qquad \text{Equation 2.3}$$

in which A is a constant. Hence, tabulation of the $\sin^2\theta$ values gives A as the common multiplier, and the miller indices for each reflection can be determined as they are integer values. Once the Miller indices are determined, Equation 2.2 can be used to calculate the lattice parameter.

For body-centred and face-centred lattices restrictions apply to the values which *h*, *k* and *l* can take for reflections to have intensity, thus some reflections are not observed in the diffraction pattern. These systematic absences are a result of destructive interference of X-rays scattered out of phase by a plane of lattice points which lie directly between two adjacent lattice planes. For example, in a body centred cubic lattice, the (1,0,0) reflection does not appear on the diffraction pattern due to the destructive interference caused by out of phase scattering of X-rays by the body-centred lattice point which lies exactly halfway between adjacent (1,0,0) lattice planes ($\lambda/2$). Thus, the restrictions on the values of *h, k* and *l* for a body-centred lattice is expressed as $h+k+l=2n+1$ and the expressions for a face-centred lattice are: $h+k=2n$, $k+l=2n$ and $h+l=2n$.

Full structural determination from powder diffraction data is difficult due to the overlap of peaks, especially at high 2θ values. The Rietveld method can be employed for structure refinement, which involves the use of a trial structure to calculate the intensities of various reflections. These calculated intensities combined with variables such as the lattice parameter and radiation wavelength create a ‘calculated' powder pattern. The ‘calculated pattern can be compared with experimentally obtained data and the trial structure amended to obtain the best fit between the calculated and obtained data. As a trial structure is needed to begin this process, completely unknown structures cannot be solved in this way and more information is needed to attempt the structure solution. If the compound forms single crystals of a large enough size single crystal X-ray diffraction can be employed.

2.2.1.2 Single Crystal X-ray Diffraction

As the name suggests, single crystal X-ray diffraction experiments involve a beam of X-rays impinging on a single crystal. The diffraction pattern obtained from a single crystal is a series of spots (Figure 2.7), each corresponding to a different set of Miller indices for the crystal structure. All possible reflections from a single crystal can be measured in terms of their angle of diffraction and intensities as the geometry of the single crystal diffractometer allows rotation of the crystal and the alignment of the detector relative to various crystal positions.

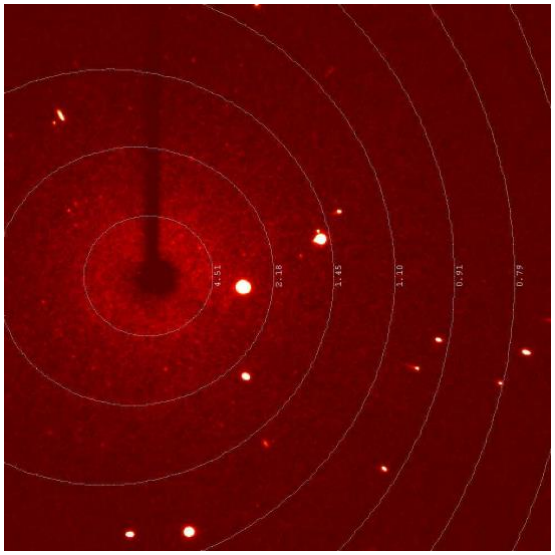

Figure 2.7 Collected frame from an SXRD experiment showing diffraction spots

The mathematical relationship between the positions of the atoms (sites of electron density) within the crystal structure and the diffraction pattern created by these atoms is a Fourier transformation (FT). Two numerical values define a scattered X-ray contributing to the diffraction pattern; these are it's amplitude, $|F|$, and phase, φ. A simple complex number to describe the phase and amplitude of a diffracted wave/ reflection with Miller indices takes the form

$$F_{hkl} = |F_{hkl}|e^{i\varphi_{hkl}} \qquad \text{Equation 2.4}$$

where F_{hkl} is the structure factor of the reflection with Miller indices h,k and l. The measured intensity of a reflection, I_{hkl}, is related to the structure factor as follows

$$I_{hkl} = C_{hkl}{F_{hkl}}^2 \qquad \text{Equation 2.5}$$

where C_{hkl} is a constant dependant on sample absorption and a number of instrumental factors.

The scattering factor of a reflection with Miller indices (h,k,l), F_{khl}, is the sum of the scattering from all the electrons in the unit cell, which repeats many times through the crystal. This summation is mathematically analysed with the following integration

$$F_{hkl} = \int_{unit\ cell} \rho_{xyz}\, e^{2\pi i(hx+ky+lz)}\, dV \qquad \text{Equation 2.6}$$

where ρ_{xyz} is the electron density at coordinates (x,y,z) in the unit cell. Summation of this continuous function is very cumbersome and can be simplified because we know that the scattering electrons are associated with atoms. So, we can assign the electrons to atomic

coordinates within the unit cell, and the number of electrons at those coordinates is equal to the atomic number of the atom. Hence, Equation 2.6 simplifies to

$$F_{hkl} = \sum_j f_j e^{2\pi i(hx+ky+lz)}$$

$$= \sum_j f_j [\cos 2\pi(hx + ky + lz) + i \sin 2\pi(hx + ky + lz)] \qquad \text{Equation 2.7}$$

where f_j is the scattering factor for an atom, j, located at coordinates (x,y,z), and defines how well X-rays are scattered by the atom as a function of Bragg angle. The value taken by f_j is directly proportional to the number of electrons in an atom or ion and at $\theta = 0°$, f_j can be taken as the atomic number of the atom. However, as electron clouds around atomic nuclei are a size on the order of the same magnitude as X-ray wavelengths, scattering from different parts of the electron cloud will not be precisely in phase, except at $\theta = 0°$. This means that f_j is dependent on the angle and will decrease with increasing θ.

The calculation of F_{hkl} for a known crystal structure can readily be carried out using the equations mentioned above resulting in a calculated diffraction pattern, however, the reverse calculation from an experimentally obtained diffraction pattern to an unknown crystal structure is more difficult due to the phase problem. The phase problem arises as the diffraction experiment measures the intensities of reflections, which are proportional to the structure factor squared

$$I_{hkl} \propto {F_{hkl}}^2 \qquad \text{Equation 2.8}$$

The square root of the measured intensity will provide the magnitude of the structure factor $|F_{hkl}|$ but gives no information of the phase. How the phase problem is overcome will be discussed in due course but first is a discussion of how the diffraction data are obtained and manipulated (reduced) into a form from which the structural information can be calculated.

In a single crystal diffraction experiment, a crystal of adequate size and appearing singular in morphology is selected from the sample using a polarising microscope. The selected crystal is mounted on the end of an 'X-ray blind' pip which can be a very fine glass fibre or thin plastic sample mount, both of which are amorphous. The crystal can be held in place with glue or more commonly manipulated and mounted in oil which becomes solid when cooled to 100-150 K on the diffractometer, thus holding the crystal in place. This is also helpful for measuring air sensitive crystal samples as the oil provides a protective coating. The fibre or sample mount with the crystal attached is mounted onto a goniometer head which allows the crystal to be rotated in the X-ray beam with a precision of a few

microns. The goniometer head is adjusted to ensure the crystal lies in the centre of the X-ray beam and facilitates rotations during data collection with an accuracy of one-hundredth of a degree. The four-circle diffractometer is the most widely used type of diffractometer and has three rotation axes for the crystal and one for the diffractometer. A point detector allows one reflection to be measured at a time, but most modern diffractometers employ a plate detector which allows the intensities and positions of several reflections to be measured simultaneously, greatly shortening the data collection time.

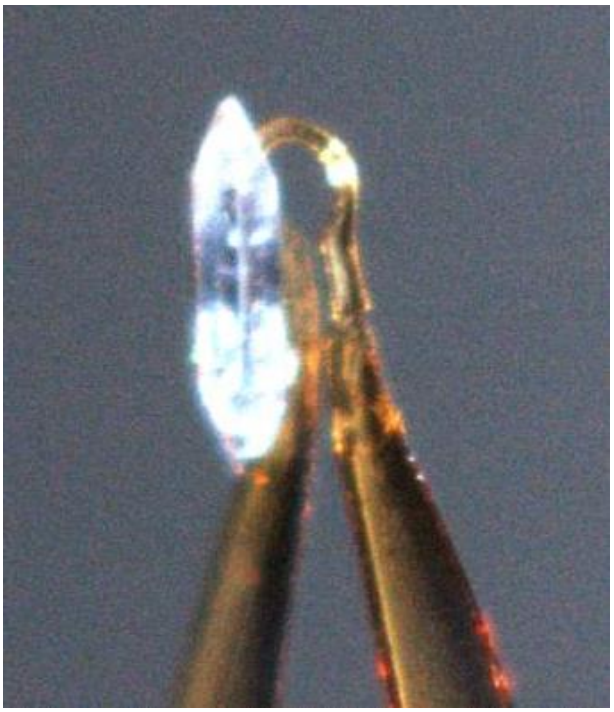

Figure 2.8 Crystal mounted on plastic 'pip'

A quick scan of the mounted crystal in a random orientation is first completed to check for singularity and crystal diffraction/quality by checking the reflections are well-defined spots (Figure 2.7). If the crystal is satisfactory a slightly longer scan is completed from which the crystal orientation and the unit cell can be estimated via the relation of the diffraction intensities to the Bragg equation, this is a complex mathematical process which is carried out computationally in a very short amount of time. With this information, a strategy for data collection can be implemented in which the need to collect the full Ewald sphere is unnecessary for all the space groups with higher symmetry than triclinic. When all the frames are collected, the data need to be refined so that the structure can be accurately calculated. This process is required because the intensities of the reflections measured are affected by a number of factors for which corrections need to be made. These corrections are a function of the geometry of the diffractometer, polarization of reflected radiation, and

absorption effects due to crystal shape. As well as corrections, repeated and symmetry-equivalent reflections are merged and averaged which gives an indication of data quality by calculating a numerical value for the agreement between equivalent reflections.

Once the data are reduced to a list of reflections structure solution can begin. As previously stated, the phase problem must be overcome to solve a crystal structure. The two most common ways of doing this are the Patterson synthesis and direct methods. The Patterson method is most useful for structures containing one or a small number of atoms which scatter significantly more than the rest of the atoms in the structure, e.g. heavy metals coordinated by organic molecules. Direct methods were originally more suited to structures where all the atoms have a similar scattering power but as computer systems have developed greater processing power direct methods is often the chosen method for structure solution as there is no longer much of a time saving from choosing Patterson for heavy atom containing structures.

The Patterson synthesis assumes all waves to be in phase and therefore all phases equal to zero, this results in the following equation:

$$P_{xyz} = \frac{1}{v}\sum_{hkl}|F_{hkl}|^2 e^{-2\pi i(hx+ky+lz)} \qquad \text{Equation 2.9}$$

where P_{xyz} is the Patterson function and is calculated from the experimental data. A Patterson map is produced by calculating the Patterson function for each coordinate in the unit cell (x,y,z), the resultant map is formed of vectors between pairs of atoms in the structure. The height of the peaks in the Patterson map is proportional to the scattering factors of the two atoms multiplied together, hence the highest peaks in a Patterson map correspond to the heaviest atoms. Once the positions of the heavy atoms have been assigned in the unit cell, the amplitudes and phases of the reflections can be calculated, thus the rest of the structure can be determined.

Direct methods utilise constraints or statistical correlations between phases which arise because of the fact that ρ_{xyz} must be a positive real number. This allows trial and error style assignments and calculations to be carried out until the best fitting model is found for the collected data. This is a complex and time-consuming method when carried out by human calculation, but computers can very quickly carry out the numerous statistical calculations to achieve a well-fitting model for the first few atoms within the structure.

Once the positions of some of the atoms have been determined either by Patterson synthesis or direct methods, $|F_{hkl}|_{calc}$ and the associated phase, φ_{hkl} can be calculated using Equation 2.7. Comparison of these calculated values can be compared with the experimentally obtained values, $|F_{hkl}|_{obs}$, by means of calculating a residual or R-factor:

$$R = \frac{\sum_{hkl}\left||F_{hkl}^{obs}| - |F_{hkl}^{calc}|\right|}{\sum_{hkl}|F_{hkl}^{obs}|} \qquad \text{Equation 2.10}$$

The R-factor is a measure of the overall difference between the calculated and observed structure factors and would ideally tend towards zero as the calculated model gets close to representing the electron density which has caused the reflection seen in the X-ray pattern. A good structural model should give R-factors of 0.05 and chemically make sense. It is very common to also calculate the R-factor based on F_{hkl2} values and/or incorporating weighting factors which incorporate the relative reliability of different measurements. This is achieved in the commonly used SHELX program via the following equation:

$$wR_2 = \sqrt{\frac{\sum w((F_{hkl}^{obs})^2 - (F_{hkl}^{calc})^2)^2}{\sum w((F_{hkl}^{obs})^2)^2}} \qquad \text{Equation 2.11}$$

Once all the atoms are correctly assigned within the unit cell the structure needs to be refined. This process involves a least-squares analysis which defines the 'best-fit' between two sets of data ($|F_{hkl}|_{calc}$ and $|F_{hkl}|_{obs}$) and refines the numerical terms describing the atomic positions and vibrations. The numerical values refined are the atom coordinates (x,y,z) and the atomic displacement parameter (U), which combined give an isotropic mean square amplitude of vibration of the atom. A better fit is achieved when six U values are assigned for each atom allowing for vibration of different amounts in different directions, this is termed anisotropic vibration. The scale factor also needs to be refined as the scale of $|F_{hkl}|_{obs}$ is arbitrary at the time of measurement and the scale of $|F_{hkl}|_{calc}$ is relative to the scattering power of one electron. A number of correction factors are also refined during this process and a standard uncertainty (s.u.) is calculated for each parameter which is refined during the least-squares process. The goodness of fit (*GoF* or *S*) is reported as the 'standard deviation of an observation of unit weight' and so is a measure of how reliable the standard deviations of the atomic parameters are.

$$GoF = S = \sqrt{\frac{\sum w((F_{hkl}^{obs})^2 - (F_{hkl}^{calc})^2)^2}{(n-p)}} \qquad \text{Equation 2.12}$$

n = number of measured data and p = number of parameters

The GoF is heavily dependent on the weighting scheme and should tend towards unity for well-matched data.

All single crystal diffraction measurements were carried out at the University of Bath Crystallography suite which is a part of the Chemical Characterisation and Analysis Facility (CCAF). During the period of this research the facility hosted two Bruker Nonius KappaCCD diffractometers which were upgraded to a Rigaku Xcalibur diffractometer operating graphite monochromated Mo K_α (λ = 0.71073 Å) X-ray tube and a Rigaku SuperNova dual tube Eos S2 CCD diffractometer equipped with a Cu K_α (λ = 1.5418 Å) and Mo K_α (λ = 0.71073 Å) micro X-ray source. All the diffractometers were fitted with an Oxford cryostream which enabled data collection at 150K to reduce thermal vibrations of atoms within the crystal analysed. The SuperNova diffractometer was particularly useful for obtaining data for very small crystals which were often obtained during this work. The CrysAlisPro software coupled with the SuperNova and Xcalibur machines was utilised to quick-scan and unit cell determination before planning of full data collections dependent on symmetry determined in the previous stage. Once a full set of data were collected CrysAlisPro was used for data reduction and any absorption corrections applied to give a HKLF format file containing a list of *hkl* values with their related F_{obs2}. Structure solution was completed with the WinGX programme suite running XPREP and SHELXS-2013 for direct methods solution and SHELXL-2013 for structure refinement. [13]

2.2.2 Scanning Electron Microscopy

Scanning electron microscopy is a useful method for obtaining images of materials magnified beyond the ability of optical microscopes and offers higher resolution. A complementary technique to crystallography, SEM coupled with energy dispersive analysis of X-ray (EDAX/EDX) or energy dispersive spectroscopy (EDS) is used to inspect sample morphology and elemental composition. SEM and EDX analyses reported in this work were obtained with a JEOL SEM6480LV microscope equipped with an Oxford INCA X-ray analyser.

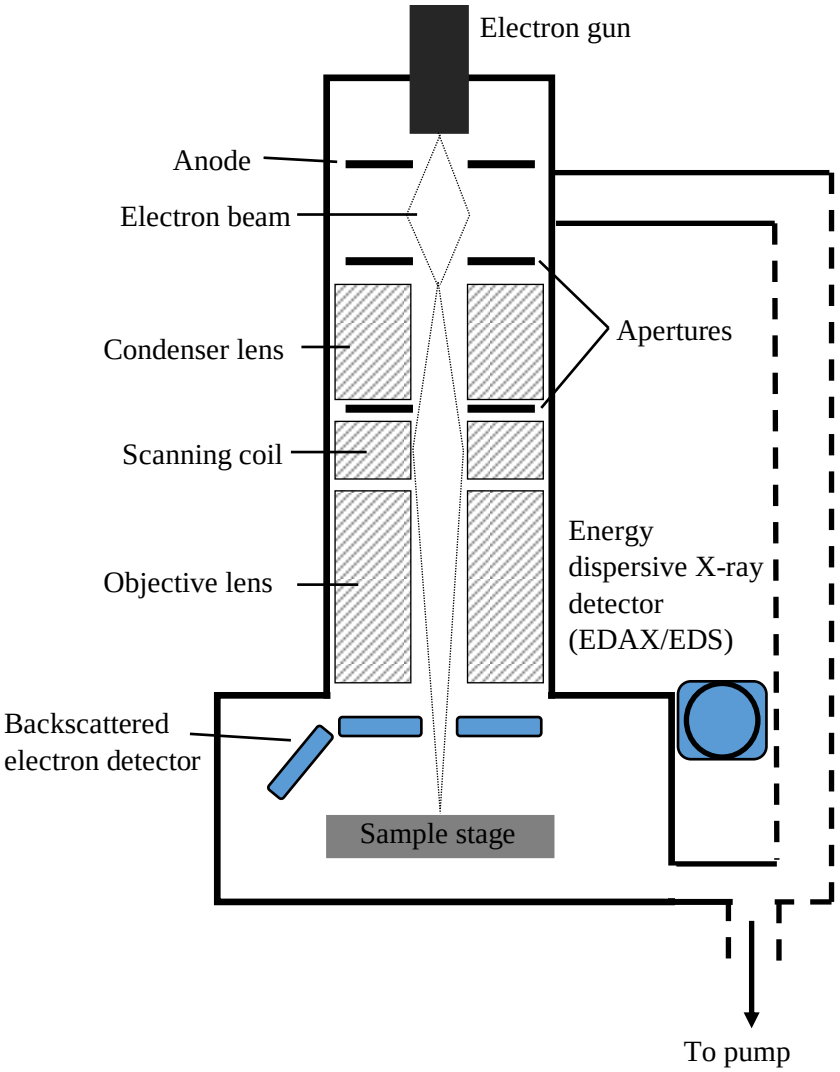

Figure 2.9 Schematic of a scanning electron microscope showing two detector systems

The schematic diagram of an SEM is shown in Figure 2.9 illustrates how an electron beam generated by the electron gun is focussed onto the surface of the sample mounted on the sample stage. The backscattered electrons are detected and compiled into the image of the sample being studied as the beam is scanned over the sample. An example of one such image is shown in Figure 2.10.

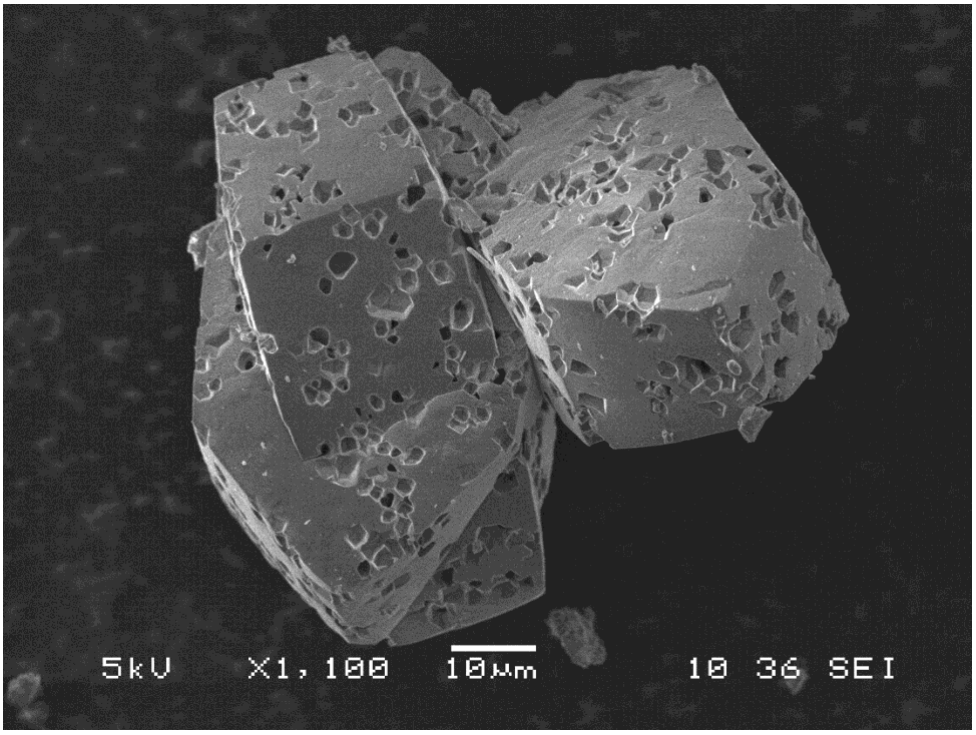

Figure 2.10 Scanning electron micrograph of a $Li_{1.87}Ti_{1.13}F_{1.61}O_{0.39}(SO_4)_2$ crystal cluster

As well as imaging from the backscattered electrons, when the high energy electron beam impinges on the sample, X-rays characteristic of the elements within the sample are generated. This occurs because the high-energy electron beam causes excitation of a core electron from the atoms, and outer shell electrons will fall back into the vacant low-lying energy level. The energy of the X-rays emitted by this process is related to the atomic number and allows the presentation of an EDAX spectrum of peaks derived from the characteristic radiation of the elements present within the sample, as shown in Figure 2.11. The intensities of the X-rays emitted are proportional to the amount of the element present allowing quantitative analysis of the composition of the sample. [14]

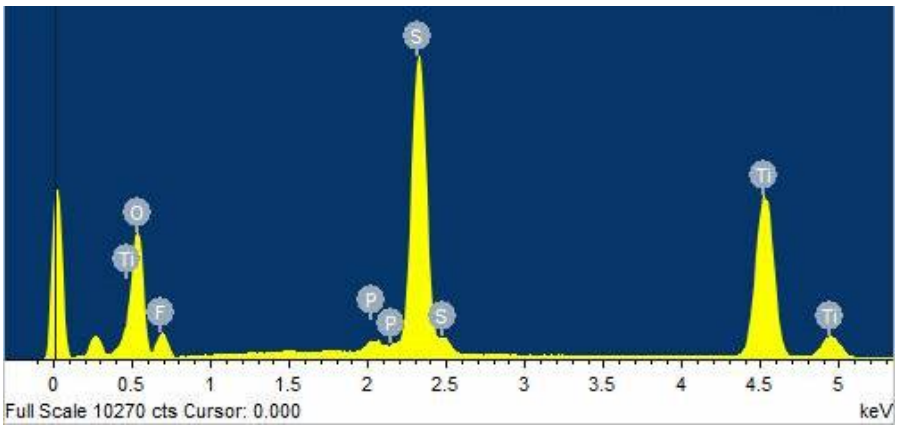

Figure 2.11 EDAX spectrum from $Li_{1.87}Ti_{1.13}F_{1.61}O_{0.39}(SO_4)_2$

2.2.3 Bond Valence Calculations

A common method for confirming crystal structures which contain a mixture of ionic and covalent bonds is the bond valence model. The bond valence model, in terms of Pauling's electrostatic valency principle, predicts the oxidation state of atoms based on the summation of all the individual bond valences surrounding the atom. Firstly, we define the valence sum rule as Equation 2.13:

$$V_i = \sum_j s_{ij} \qquad \text{Equation 2.13}$$

where V_i is the valence of atom i and equates to the sum of all the individual bond valencies (s_{ij}) between atoms i and j. For inorganic compounds, individual bond valences correlate very well with observed bond lengths and can be calculated according to

$$s_{ij} = exp\left(\frac{R_o - R_{ij}}{b}\right) \qquad \text{Equation 2.14}$$

where R_{ij} is the observed bond length, R_o is a tabulated parameter representing the idealised bond length when atom i has a valency of 1, and b is an empirical constant (usually 0.37 Å). Bond valences calculated in this way from bond lengths obtained from solution of single crystal data can be compared with theoretical valence values. Confidence in the solution of the crystal structure can be obtained when the two valences agree.[15] This method was used widely throughout the work reported herein, both for confirmation of transition metal oxidation state and for distinction between oxide and fluoride/hydroxide groups.

2.3 References

(1) Wold, A.; Dwight, K. Synthetic Technicques. In *Solid State Chemistry Synthesis, Structure, and Properties of Selected Oxides and Sulfides*; Springer Science + Business Media Dordrecht/Chapman & Hall, 1993; pp 70–89.

(2) Weller, M. T. *Inorganic Materials Chemistry*; Evans, J., Ed.; Oxford University Press: Oxford, 1994.

(3) Byrappa, K.; Yoshimura, M. Hydrothermal Technology—Principles and Applications. In *Handbook of Hydrothermal Technology*; Elsevier, 2013; pp 1–52.

(4) Armstrong, J. A.; Williams, E. R.; Weller, M. T. Manganese (III) Fluorophosphate Frameworks. *Dalt. Trans.* **2013**, *42*, 2302–2308.

(5) Armstrong, J. A.; Williams, E. R.; Weller, M. T. Fluoride-Rich, Hydrofluorothermal Routes to Functional Transition Metal (Mn, Fe, Co, Cu) Fluorophosphates. *J. Am. Chem. Soc.* **2011**, *133*, 8252–8263.

(6) Wang, Q.; Madsen, A.; Owen, J. R.; Weller, M. T. Direct Hydrofluorothermal Synthesis of Sodium Transition Metal Fluorosulfates as Possible Na-Ion Battery Cathode Materials. *Chem. Commun.* **2013**, *49* (49), 2121–2123.

(7) Marshall, K. L.; Armstrong, J. A.; Weller, M. T. Gallium Fluoroarsenates. *Dalt. Trans.* **2015**, *44*.

(8) Ewald, P. P. Chapter 2- X-Rays. In *50 years of X-ray diffraction*; 1962; pp 6–16.

(9) Ewald, P. P. Chapter 4-Laue's Discovery of X-Ray Diffraction by Crystals. In *50 years of X-ray diffraction*; 1962; pp 31–56.

(10) Clegg, W. *Crystal Structure Determination*; Evans, J., Ed.; Oxford University Press: Oxford, 1998.

(11) Weller, M. T.; Young, N. A. Diffraction Methods and Crystallography. In *Characterisation methods in inorganic chemistry*; Oxford : Oxford University Press: Oxford, 2017; pp 20–55.

(12) Marshall, K. L.; Wang, Q.; Sullivan, H. S. I.; Weller, M. T. Synthesis and Structural Characterisation of Transition Metal Fluoride Sulfates. *Dalt. Trans.* **2016**, *45*.

(13) Sheldrick, G. M. A Short History of SHELX. *Acta Crystallogr. Sect. A Found. Crystallogr.* **2008**, *64* (1), 112–122.

(14) Weller, M. T.; Young, N. A. 6.7 Scanning Electron Microscopy (SEM). In *Characterisation methods in inorganic chemistry*; Oxford : Oxford University Press: Oxford, 2017; pp 217–219.

(15) Brown, I. D. Bond Valences-A Simple Structural Model for Inorganic Chemistry. *Chem. Soc. Rev.* **1978**, No. 7, 359–376.

Chapter 3 : Titanium Fluorophosphates

3.0 Introduction

The original aim of this research was to produce novel titanium-based framework inorganic materials with structural features to promote ion transport alongside the ability for redox activity of the titanium centres. Previous studies have shown that oxopolyhedra such as phosphate and sulfate groups interconnecting transition metal polyhedra form framework structures which can have very good ion transport capabilities. When the transition metal is redox active and Li^+ or Na^+ ions are incorporated into the inter-framework space, the materials become of interest for rechargeable battery electrodes. In particular, $LiFePO_4$ has been studied in great detail for its use as a cathode material in rechargeable lithium-ion batteries. [1–4] Recent studies have shown that a wider variety of structures are available when other anions are incorporated into the polyhedral units. For example, the inclusion of fluoride is thought to promote ion transport in transition metal phosphate materials when included as terminal sites on polyhedral units but may also act as a bridging anion similarly to oxygen, increasing connectivity between polyhedral units. [5–7]

A few titanium fluorophosphates have been previously reported; in particular, $LiTiPO_4F$ has been studied as a potential electrode material by Recham et al in 2010.[8] Various titanium phosphates have been synthesised and studied for a variety of application characteristics from ion transport to catalysis and potassium titanyl phosphate ($KTiOPO_4$) has been studied for nonlinear optical properties.[9] NASICON-type structures (general formula $MTi_2(PO_4)_3$, M= Li^+, Na^+) have been studied for fast ion conduction and low thermal expansion ceramics. [10–13] Initial reactions aimed to produce structures analogous to the NASICON-type but with the inclusion of fluorine.

Water is the primary reaction medium for the hydrothermal method, but to increase the amount of fluoride incorporated into the final products the water content of these reactions was minimised. Traditionally, transition metal fluorides have been employed in the hydrofluorothermal reaction, in the work presented herein hexafluorotitanic acid (60 wt. % in H_2O) and the potassium hexafluorotitanate salt were utilised as high fluoride sources of titanium. Full reaction conditions are summarised in the experimental section of the paper published and in Table 3.2.

The first four novel phases produced from this work were published in Zeitschrift für Anorganische und Allgemeine Chemie (ZAAC) as the article included in section 3.1. The results include two titanium fluorophosphate frameworks, one titanium fluoro-/hydroxy-sulfate and the unexpected result of a salt formed of doubly protonated organic molecular

cations and hexafluorotitanium anions. An additional two titanium fluorophosphate/fluoride hydrogen-phosphate structures were produced after the publication of the article and are reported in sections 3.3 and 3.4 of this chapter. Only reactions from this work which produced novel crystalline structures have been reported. A multitude of reaction conditions and starting materials were also carried out in over 500 reactions but many produced known or amorphous structures or unreacted starting materials hence were not studied further.

3.1 Paper

This declaration concerns the article entitled:									
Synthesis of titanium fluorophosphates and fluorosulfates from hexafluorotitanic acid									
Publication status (tick one)									
draft manuscript		**Submitted**		**In review**		**Accepted**		**Published**	X
Publication details (reference)	Zeitschrift für Anorganische und Allgemeine Chemie (Journal of Inorganic and General Chemistry) Volume 640 Issue 14 Pages 2766-2770 First Published: 9th October 2014								
Candidate's contribution to the paper (detailed, and also given as a percentage).	The candidate predominantly executed the Experimental work: All syntheses and crystallographic data collection, structure solution and refinement. 100% Presentation of data in journal format: 80%								
Statement from Candidate	This paper reports on original research I conducted during the period of my Higher Degree by Research candidature.								
Signed						**Date**			

ARTICLE

DOI: 10.1002/zaac.201400362

Synthesis of Titanium Fluorophosphates and Fluorosulfates from Hexafluorotitanic acid

Kayleigh L. Marshall[a] and Mark. T. Weller*[a]

Dedicated to ProfessorMartin Jansen on the Occasion of His 70th Birthday

Keywords: Hydrothermal; Fluorides; Titanium; Crystal structures

Abstract. Three new titanium-based network structures and an organic tetraazapentacenium $[TiF_6]^{2-}$ salt were synthesized under high fluoride-concentration, hydrothermal conditions utilising hexafluorotitanic acid as a starting material. The compositions of the new connected-structure phases obtained are $CsTi_2F_2(PO_4)(PO_3F)_2$, [Imidazole-H][$Ti_3F_2(PO_3F)$-$(PO_4)_3$]·$0.5H_2O$, and [DABCO-H][$Ti(SO_4)_2$ $(SO_3(OH,F))$]. $CsTi_2F_2(PO_4)(PO_3F)_2$ has a sheet-like structure with interlayer Cs^+ ions coordinated solely by fluoride ions, whereas [Imidazo-le-H][$Ti_3F_2(PO_3F)(PO_4)_3$]·$0.5H_2O$ has a three-dimensional framework structure with elliptical channels containing pairs of organic template molecules. The DABCO templated phase is isostructural with ferrinatrite with chains formed from titanium coordinated by six sulfate groups. Reactions using 1,2-phenylenediamine under these conditions surprisingly generates 5,12-dihydro-5,7,12,14-tetraazapentacenium cati-ons which crystallize as a salt with $[TiF_6]^{2-}$.

Introduction

High fluoride-content hydrothermal (hydrofluoric-thermal) synthesis has proved to be a successful technique for producing new mid- to late- first-row transition metal fluorophosphates and fluorosulfates Such materials are of interest due to the functionality that arises from rigid and stable structures containing channels or pores, for example by making them highly suited to applications as battery cathode and anode materials.[5] Other applications of transition metal framework and layer structures based on linked polyhedral units include catalysis, molecular separations and, potentially, optoelectronic and magnetic material uses. For applications as cathode materials in Li- and Na- ion rechargeable batteries the inclusion of fluoride into transition metal phosphate and sulfate structures has been found to be favourable due to the high electronegativity of fluoride causing an increase in the cell potential.[6] While titanium phosphate materials have previously been investigated with respect to potential applications as non-linear optical materials and in catalysis, very few titanium fluorophosphate structures have been described.[7-11]

* Prof. M. T. Weller
Fax: +44 (0)1225 38
E-Mail: m.t.weller@bath.ac.uk
[a] Department of Chemistry
University of Bath
Claverton Down
Bath, BA2 7AY. UK

In our previously reported hydrofluorothermal syntheses we have used transition metal fluorides as starting materials in order to facilitate the incorporation of fluoride ions into the product structures; hydrofluoric acid may also be used as a fluoride source though this has increased safety concerns.[1-5,14,15] In the work reported herein we have employed hexafluorotitanic acid, H_2TiF_6, instead of titanium fluorides as a reactant to maintain high fluoride ion concentrations in the reaction medium.

Large alkali metal cations and organic amines have previously been used extensively as templating agents within hydrothermal syntheses leading to a vast range of open-framework structures.[15,16] In this work, we have employed these large templating species in combination with hexafluorotitanic acid and oxo-fluoro-tetrahedral species (e.g. PO_4^{3-}, PO_3F^{2-}, SO_3F^-, SO_4^{2-}) to generate four new phases that have been structurally characterized using single crystal X-ray diffraction.

Results and Discussion

Table 3.1 summarizes the compositional and structural data for the new phases reported in this article.

$CsTi_2F_2(PO_4)(PO_3F)_2$ (I)

$CsTi_2F_2(PO_4)(PO_3F)_2$ crystallizes as small, ca. 40×40×10 μm colourless plates adopting a monoclinic unit cell with the space group *P*2/*c*. The structure consists of two-dimensional layers of interconnected TiO_5F octahedra with both PO_4 and

Table 3.1 Summary of compositional and structure refinement data for products **I-IV** obtained in this study

Structure formula	Formula weight /g·mol^{-1}	Space group	Unit cell dimensions /Å,°	Volume /Å^3	Z	Number of reflections measured (unique)	*R* indices observed data	GoF
$CsTi_2F_2(PO_4)(PO_3F)_2$ (**I**)	278.8	*P*2/*c*	*a* = 8.1839(16) *b* = 8.3843(17) *β* = 97.45(3) *c* = 8.7851(18)	597.71(24)	4	2692 (1762)	R_1 = 0.073 wR_2 = 0.121	1.045
[Imidazole-H][$Ti_3F_2(PO_3F)(PO_4)_3$] ·0.5H_2O (**II**)	314.8	*Pnnm*	*a* = 14.4041(2) *b* = 18.3489(3) *c* = 6.3238(1)	1671.38(0)	8	22874(1795)	R_1= 0.051 wR_1 = 0.141	1.074
[DABCO-H][$Ti(SO_4)_2(SO_3(F,OH))$] (**III**)	498.4	*P*2$_1$	*a* = 9.8620(20) *b* = 17.2310(34) *β* = 93.86(3) *c* = 17.1850(0)	2913.68(60)	7	11463 (11445)	R_1 = 0.096 wR_2 = 0.232	1.059
[$C_{18}N_4H_{14}$][TiF_6] (**IV**)	448.2	*C*2/*c*	*a* = 12.6700(25) *b* = 8.7330(17) *β* = 107.01(3) *c* = 15.4090(31)	1630.37(16)	4	3040 (3038)	R_1 = 0.039 wR_2 = 0.107	1.173

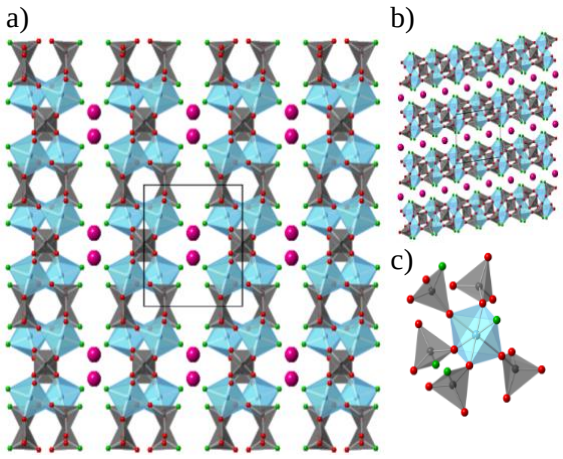

Figure 3.1 (a) Structure **I** viewed down the c axis (b axis vertical). (b) Structure **I** viewed down the b axis. (c) Connectivity of phosphate groups around the titanium centre. Blue octahedra: TiO_5F, grey tetrahedra: PO_4 and PO_3F, and red, green and pink spheres: O, F and Cs respectively.

PO_3F tetrahedra as shown in Figure 3.1a and b. The fluoride ions of the TiO_5F and PO_3F polyhedra are directed into the interlayer spacing and form the coordination environment of the Cs_+ ion of eight fluo-ride ions at distances between 3.09 and 3.46 Å; the PO_4 tetrahedron forms the central unit of the layers and is linked through all vertices to titanium atoms.

[Imidazole-H][$Ti_3F_2(PO_3F)(PO_4)_3$]·0.5H_2O (II)

[Imidazole-H][$Ti_3F_2(PO_3F)(PO_4)_3$]·0.5H_2O **c**rystallizes as transparent, square plates adopting an orthorhombic unit cell and the space group *Pnnm*. The structure consists of a fully interconnected inorganic framework containing three unique titanium environments linked through a mixture of PO_3F and PO_4 tetrahedra (Figure 3.2). Ti(1) is coordinated by six oxygen atoms, while Ti(2) is co-ordinated by four oxygens and two *cis*- fluoride ions; one fluoride ion is terminal to Ti(2) and points into the pore-containing the organic template, the other fluoride ion on Ti(2) is bridging to Ti(3), whose coordination sphere is then completed by five oxygen atoms. The PO_3F group that links two central Ti(1) atoms and one Ti(3) atom is orientationally disordered over two positions with respect to the direction of the P-F bond along the *c* axis. The local orientation of these tetrahedra is probably connected to the partially occupied water molecule site which can have between 0 and 4 P-F units directed towards it - with the potential to form P-F···H_2O hydrogen bonds.

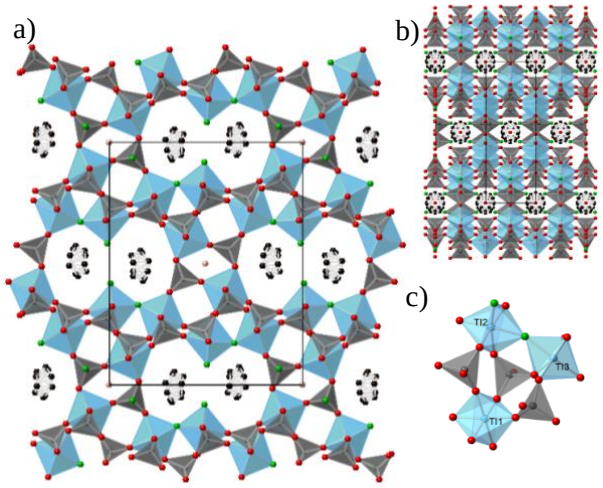

Figure 3.2 (a) Structure **II** viewed down the c axis. (b) Structure II viewed down the a axis. (c) The connectivity between the three unique Ti sites within structure **II**. Blue octahedra: Ti(O, F)$_6$, grey tetrahedra: PO_4 and PO_3F, and red, green and black spheres:O, F and C or N respectively.

This inorganic framework forms large channels which run parallel to the *c* axis and contain the templating H-imidazolium molecular cations. This channel has an unusual "figure of eight" shape with the two lobes separated by the terminal fluoride ions on two central Ti(2) atoms; each lobe of the channel

contains an H-imidazolium cation. The orientation of the H-imidazolium cations within the channels was found to be strongly disordered with two possible positions of the five-membered ring and the nitrogen and carbon atoms could not be distinguished during structure refinement.

[DABCO-H][Ti(SO$_4$)$_2$(SO$_3$(OH,F))] (III)

[DABCO-H][Ti(SO$_4$)$_2$(SO$_3$(OH, F))] crystallizes as large colourless flat needles adopting a monoclinic unit cell and the space group *P*2$_1$. The structure consists of one-dimensional chains of interlinked TiO$_6$ octahedra and SO$_3$(OH, F) tetrahedra (Figure 3.3). Each titanium atom is fully coordinated by, and connected to, the next titanium atom by three (fluoro-/hydrogen-) sulfate groups. The chains run parallel to the *c* axis with a hexagonal spatial distribution (Figure 3.3b) with the [DABCO-H]$^+$ molecular ions in the inter-chain space. Each [DABCO-H]$^+$ molecular ions orientates between two adjacent sulfate groups on one chain and one sulfate unit on a second adjacent chain with N⋯O(F) distances of 2.7-2.9Å indicating weak hydrogen-bonding interactions between the template cation and the inorganic chains.

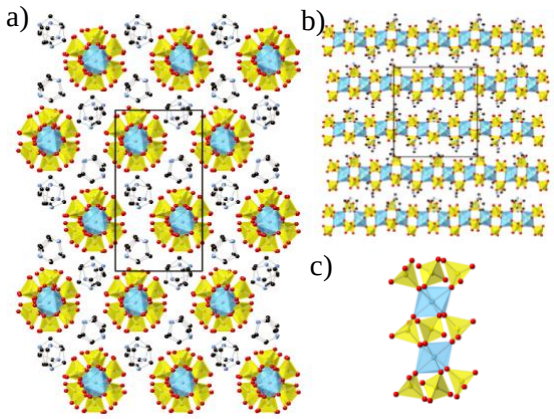

Figure 3.3 (a) Structure **III** viewed down the c axis (b axis vertical). (b) Structure **III** viewed down the a axis (c axis vertical). (c) Intrachain connectivity of structure **III**. Blue octahedra: TiO$_6$, yellow tetrahedra: SO$_2$(O, OH, F)$_2$, red and green spheres: O and F. Carbon and nitrogen in DABCO: black and pale blue spheres respectively.

Refined atomic displacement parameters (ADPs), bond valence calculation results for the terminal anion sites within the chains when coupled with charge balance considerations suggest the disordered presence of partial oxido-, hydroxide or fluoride ions at these sites, i.e. [(Ti-O-)$_2$S*X*$_2$] units, where *X* is a mixture of OH$^-$, F$^-$, and O$_2^-$. However, a definitive assignment of the nature of these anions was not possible.

[C$_{18}$N$_4$H$_{14}$][TiF$_6$] (IV), Tetraazapentacenium Hexafluorotitanate.

This product was obtained from a reaction that aimed to incorporate 1,2-phenylenediamine as a templating amine into a titanium fluorophosphate framework. However, under the reaction conditions, the diamine underwent a reaction to produce tetraazapentacene, possibly catalysed by the central titanium atoms or hydrofluoric acid. Following the surprising isolation of this product in reasonably good yields, the quality of the reactant 1,2-phenylenediamine was checked by solution NMR and shown to be of high purity - demonstrating that the conversion to tetraazapentacene takes place under the hydrofluorothermal reaction conditions.

[C$_{18}$N$_4$H$_{14}$]$^{2+}$[TiF$_6$]$^{2-}$ was obtained as orange, lustrous triangular blocks. The compound crystallizes in a monoclinic unit cell with the space group *C*2/*c*. The salt-like structure comprises of layers of doubly protonated 5,12-dihydro-5,7,12,14-tetraazapentacene molecular cat-ions and near regular [TiF$_6$]$^{2-}$ octahedral anions (Figure 4). Ti-F distances lie in the range 1.816-1.894 Å. The [TiF$_6$]$^{2-}$ octahedral anions lie in the *ab* plane and are separated by parallel layers of tetraazapentacenium molecular cations; these units are stacked such that the 1 and 2 rings of one molecule lie above the 4 and 5 rings in the adjacent layer at a distance of ca. 3.4Å. Four of the fluoride ions in each [TiF$_6$]$^{2-}$ molecular anion are forming hydrogen bonds with N-H groups at distances NH⋯F of 1.786 Å (×2) and 1.858 Å (×2).

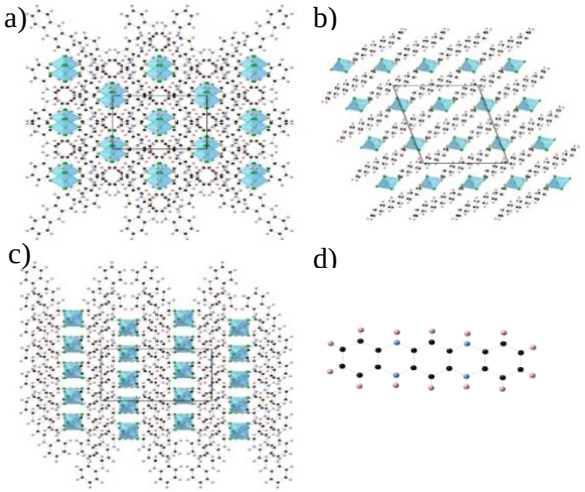

Figure 3.4 (a) Structure **IV** viewed down the c axis (a axis vertical). (b) Structure **IV** viewed down the b axis (a axis vertical). (c) Structure **IV** viewed down the a axis (c axis horizontal). (d) Doubly protonated 5,12-dihydro-5,7,12,14-tetrazapentacene in structure IV. Blue octahedra: TiF$_6$. Carbon, nitrogen and hydrogen in tetrazapentacene: black, pale blue and pale pink spheres respectively.

Conclusions

Reactions undertaken in fluoride-rich, low water content media produced by using hexafluorotitanic acid, H_2TiF_6 as a reactant with phosphoric or sulphuric acids allow the formation of new network structures based on linked $Ti(O, F)_6$ octahedral and $T(O, F)_4$, T = S, P tetrahedral units.

$CsTi_2F_2(PO_4)(PO_3F)_2$ demonstrates structural features seen previously in many transition metal fluoro-phosphates by adopting a sheet-like structure in which fluoride ions terminating the Ti-centred octahedra and P-centred tetrahedra are directed into the interlayer space and coordinate to a counter cation. [1-5] Similar structural features are seen in $[Imidazole\text{-}H][Ti_3F_2(PO_3F)(PO_4)_3]\cdot 0.5H_2O$, though in this compound the inorganic framework is three-dimensionally connected. One unusual feature of this material is the presence of two directly opposed Ti-F bonds which bisect a large cavity that contains the pairs of templating $[Imidazole\text{-}H]^+$ cations.

The titanium fluorophosphate previously reported vary from 3D structures resembling Tavorite ($LiTiPO_4F$), through 2D layers ($Ti^{III}Ti^{IV}(OH)F_4(HPO_4)(PO_4)(N\text{-}((CH_2)_2NH_3)_3)$ and $Na_3[Ti_2P_2O_{10}F]\cdot xH_2O$) to 1D chains ($(NH_4)_xK_{4-x}[Ti_2PO_4F_9]$ (x = 0, 0.70, 1.00, 1.25)). In all but the tavorite-like structure, the fluoride ions are terminal and orient towards inter-framework space or counter cations, as with the 2D structure reported here (structure **I**). In $LiTiPO_4F$ the fluoride acts as a bridging ion between two titanium metal centres, as also observed in the 3D framework reported herein (structure **II**). [12, 13, 15, 22]

The inorganic chains in $[DABCO\text{-}H][Ti(SO_4)_2(SO_3(OH, F))]$ are isostructural with those found in ferrinatrite, $Na_3Fe(SO_4)_3\cdot 3H_2O$ and with a similar hexagonal spatial distribution.[17] The higher charge on titanium (4+) compared with Fe^{3+} in ferrinatrite is compensated for by the lower level of the larger, monovalent DABCO. This appears to be the first reported titanium fluorosulfate structure and interestingly forms 1D chains as opposed to 3D frameworks seen for the titanium oxysulfates $TiOSO_4$ and $TiOSO_4\cdot H_2O$. [20-21]

The formation of reasonably high yields of $[C_{18}N_4H_{14}]^{2+}[TiF_6]^{2-}$ from reaction media containing 1,2-phenylenediamine is surprising but might provide a simple route to the synthesis of this tetraazapentacene species.

Experimental Section

All materials used were purchased commercially and of reagent grade requiring no further purification.

Warning! Possible violent nature of the reactions, with the generation of HF gas.

Synthesis of $CsTi_2F_2(PO_4)(PO_3F)_2$ (I): H_2TiF_6 (60% wt in H_2O, 0.16 mL), CsF (0.3035 g, 2.00 mmol) and HPF_6 (~50% wt in H_2O, 0.64 mL) were combined and sealed in a 23mL Teflon™-lined Parr autoclave. The mixture was heated at 210 °C for 3 days before cooling to room temperature. The product was filtered under vacuum and air dried in an oven; the titanophosphate phase was found as a minor constituent, ~ 5%, of the solid. Washing with warm phosphoric acid (85% wt in H_2O) dissolved the amorphous matrix to leave a purer sample whose powder X-ray diffraction pattern showed a good match to that calculated from the structure determined for this phase (Appendix – Figure 1).

Synthesis of $[Imidazole\text{-}H][Ti_3F_2(PO_3F)(PO_4)_3]\cdot 0.5\text{-}H_2O$ (II): H_2TiF_6 (60% wt in H_2O, 0.16 mL), H_3PO_4 (85% wt in H_2O, 0.20 mL) and imidazole (0.0681 g, 1 mmol) were combined and sealed in a 23 mL Teflon™-lined Parr autoclave. The mixture was heated at 200 °C for 4 days before cooling to room temperature. The product was filtered under vacuum and air dried in a drying oven. The major peaks in the powder X-ray diffraction pattern match those calculated from the determined crystal structure, indicating a crystalline phase purity of over 50% (Appendix – Figure 2).

Synthesis of $[DABCO\text{-}H][Ti(SO_4)_2(SO_3(OH,F))]$ (III): H_2TiF_6 (60% wt in H_2O, 0.16 mL), H_2SO_4 (95-98%, 0.17 mL) and DABCO (0.1121 g, 1 mmol) were combined, agitated and sealed in a 23 mL Teflon™-lined Parr autoclave. The mixture was heated at 210 °C for 4 days before cooling to room temperature. The product was filtered under vacuum and air dried in a drying oven, ~40% phase purity (Appendix – Figure 3).

Synthesis of $[C_{18}N_4H_{14}][TiF_6]$ (IV): H_2TiF_6 (60% wt in H_2O, 0.16 mL), H_3PO_4 (85% wt in H_2O, 0.20 mL) and 1,2-phenylenediamine (0.1085 g, 1 mmol) were combined, agitated and sealed in a 23 mL Teflon™-lined Parr autoclave. The mixture was heated at 175 °C for 4 days before cooling to room temperature. The product was filtered under vacuum and air dried in a drying oven; ~50% phase purity. Pure crystals were obtained by stirring the sample in excess warm phosphoric acid (85% wt in H_2O) for 15 minutes before filtering under vacuum and washing with water (Appendix – Figure 4).

X-ray diffraction: Single-crystal X-ray diffraction data were collected at 150 K on an Oxford Diffraction Gemini A Ultra CCD diffractometer operating Mo Kα (λ = 0.7093 Å) radiation. Single-crystal X-ray diffraction data for structure II were collected at 150 K on an Agilent Supernova, dual tube Eos S2 CCD diffractometer operating Cu K_α (λ = 1.54178 Å) radiation. All structures were solved using the WinGX programme suite, implementing XPREP[18] and SHELXS-2013[19] to solve structures by direct methods and SHELXL-2013[19] to refine the structures along with charge balancing and bond

valence calculations to assign atoms as oxygen or fluorine. Single-crystal refinement data are summarised in Table 1.

During the refinement for structure **II**, the imidazole molecule was refined over two disordered positions with half site occupancies and all sites were assigned as carbon. Restraints were also used during the refinement of structure **III** due to anion disorder within the inorganic chains and some local positional disorder of the DABCO-H cations. Some carbon-carbon and carbon-nitrogen distances in DABCO molecules had soft restraints applied at 1.54(2)Å ADPs of the terminal anions of the (fluoro-/hydrogen-) sulfate groups were restricted to isotropic values.

Further details of the crystal structure investigations may be obtained from the Fachinformationszentrum Karlsruhe, 76344 Eggenstein- Leopoldshafen, Germany (Fax: +49-7247-808-666;E-Mail:crysdata@fiz-karlsruhe.de, http://www.fiz-karlsruhe.de/request for deposited data.html) on quoting the depository numbers CSD-428150 (compound **I**), CSD-428151 (compound **II**), CSD-428152 (compound **III),** CSD-428153 (Compound **IV**).

Acknowledgements

The authors would like to thank the University of Bath for funding including a studentship for KM, and Kim Gallagher for the solution NMR data.

References

[1] J. A. Armstrong, E. R. Williams and M. T. Weller, *J. Am. Chem. Soc.*, **2011**, *133*, 8252-8263.
[2] J. A. Armstrong, E. R. Williams and M. T. Weller, *Dalt. Trans.*, **2012**, *41*, 14180-14187.
[3] A. C. Keates, J. A. Armstrong and M. T. Weller, *Dalt. Trans.*, **2013**, *42*, 10715-10724.
[4] E. R. Williams, S. A. Morris and M. T. Weller, *Dalt. Trans.*, **2012**, *41*, 10845-10853.
[5] J. A. Armstrong, E. R. Williams and M. T. Weller, *Dalt. Trans.* **2013**, *42*, 2302-2308.
[6] R. Tripathi, G. Popov, B. L. Ellis, A. Huq and L. F. Nazar, *Energy Environ. Sci.*, **2012**, *5*, 6238-6246.
[7] R. Essehli, B. El Bali, S. Benmokhtar, K. Fejfarová and M. Dusek, *Mat. Res. Bull.*, **2009**, *44*, 1502-1510.
[8] S. Y. Guo, S. Han, B. Chi, J. Pu and J. Li, *Int. J. Hydrogen Energy* **2014**, *39*, 2446-2453.
[9] C. Serre and G. Ferey, *Inorg. Chem.*, **1999**, *23*, 5370-5373.
[10] Y. Liu, Z. Shi, Y. Fu, W. Chen, B. Li, J. Hua, W. Liu, F. Deng and W. Pang, *Chem. Mater.*, **2002**, *14*, 1555-1563.
[11] A. Bhaumik, *Chemi. Sci.*, **2002**, *114*, 451-460.
[12] S. H. Yang, G. B. Li, L. Li, S. J. Tian, F. H. Liao, M. Xiong and J. H. Lin, *Inorg. Chem.*, **2007**, *46*, 11431-11436.
[13] N. Recham, J. N. Chotard, J. C. Jumas, L. Laffont, M. Armand and J. M. Tarascon, *Chem. Mater.*, **2010**, *22*, 1142-1148.
[14] a) Q. Wang, A. Madsen, J. R. Owen and M. T. Weller, *Chem. Comm.*, **2013**, *49*, 2121.
[15] C. Serre, M. Haouas, F. Taulelle, W. Van Beek and G. Férey, *C. R. Chim.*, **2010**, *13*, 336-342.
[16] J. Rouse, K. V. Redrup, E. Kotsapa and M. T. Weller, *Chem. Comm.*,**2009**, 7209-7211.
[17] F. Scodari, *Mineral. Mag.*, **1977**, *41*, 375-383.
[18] G. Sheldrick, *XPREP. Space Group Determination and Reciprocal Space Plots*, **1991**
[19] G. M. Sheldrick, *Acta Crystollagr., Sect. A: Fundam. Crystallogr.*, **2008**, *64*, 112-122.
[20] B. M. Gatehouse and S. N. Platts, *Acta. Cryst.*, **1993**, *B49*, 428-435.
[21] M. A. K. Ahmed, H. Fjellvåg and A. Kjekshus, *Acta. Chem. Scand.*, **1996**, *50*, 275-283.
[22] S. H. Yang, G. B. Li, L. P. You, J. L. Tao, C. K. Loong, S. J. Tian, F. H. Liao and J. H Lin, *Chem. Mater.*, **2007**, *19*, 942-247.

Received: August 1, 2014
Published online: October 9, 2014

3.2 Unpublished Titanium Fluorophosphates

After the publication of the article in section 3.1, one further titanium fluoro/hydrogen-phosphate and one titanium fluoride hydrogen-phosphate were synthesised from high fluoride hydrothermal reactions. The reaction conditions are summarised in Table 3.2.

Table 3.2 Summary of reaction conditions for the two additional titanium fluoro-/hydrogen-phosphate phases reported herein

Reagents	**Temp (°C)**	**Time (h)**	**Crystal Morphology**	**Product Formula**	**Section**
H_2TiF_6 (1 mmol, 0.16 mL) LiF (1 mmol, 0.0259 g) H_3PO_4 (3 mmol, 0.20 mL)	210	72	Colourless needles	$Ti(HPO_4)(PO_3F)$	3.3
K_2TiF_6 (1 mmol, 0.2401 g) H_3PO_4 (3 mmol, 0.20 mL)	210	72	Colourless plates	$K_2Ti_2F_2(PO_4)(H[PO_4]_2)$	3.4

3.3 Structure V: $Ti(PO_3[OH/F])(PO_3F)$

The product crystallised as colourless needle crystals, a suitable sample of which was selected for an SXRD study carried out at 150 K on a Bruker Nonius Kappa CCD diffractometer operating Mo Kα (λ = 0.7073 Å) radiation. Collected data were refined to a three-dimensional structure of interconnected titanium centred octahedra and hydrogen phosphate and fluorophosphate tetrahedra. The solved structure showed a monoclinic unit cell in space group $P2_1/c$; the crystallographic information for structure **V** is summarised in Table 3.3.

Table 3.3 Single crystal diffraction structure solution summary for structure **V**.

Empirical Formula	$Ti_2P_4O_{14}FH$
Formula Weight ($gmol^{-1}$)	241.81
Temperature (K)	150
Appearance	Colourless needles
Crystal size (mm)	0.01 × 0.02 × 0.06
Crystal system	Monoclinic
Space group	$P2_1/c$
Unit cell dimensions	a = 5.061 (1) Å b = 7.521 (2) Å c = 16.164(3) Å β = 90.88(3) °
λ/Å	0.71703 (Mo Kα)
Volume ($Å^3$)	615.19 (4)
Z	3
Density (gcm^{-3})	2.61
Reflections collected	2579
Unique reflections	1414
R_1 (all)	0.078
wR_2 (all)	0.170
GoF	1.205

The structure comprises of one unique titanium coordination environment, Ti1, which is six-fold coordinated by oxygen atoms from two distinct fluoro-/hydrogen-phosphate tetrahedra as shown in Figure 3.5 (c). During the initial structure solution, there was a small excess of electron density approximately 1Å from the terminal oxygen of the P1 phosphate group (O7). This was attributed to a partially occupied hydrogen site and the presence of hydrogen bonding checked via infra-red spectrometry (Figure 3.6). The presence of a broad peak at 3258 cm^{-1} suggests weak O-H···F hydrogen bonding as reported by Emsley and is expected of the 2.808 Å O-H···F distance. [14] As the hydrogen bond lies on the inversion centre of the unit cell the structure was modelled on a 50:50 split occupancy OH/F terminal site of the P1 phosphate group. The other crystallographically

distinct phosphorous, P2, is the centre of a fluoro-phosphate tetrahedra in which the terminal fluoride points into the lobe-like cavities created by the hydrogen bonding of the P1 hydroxy-/fluoro-phosphate through the centre of the crystal structure (Figure 3.5 (a)).

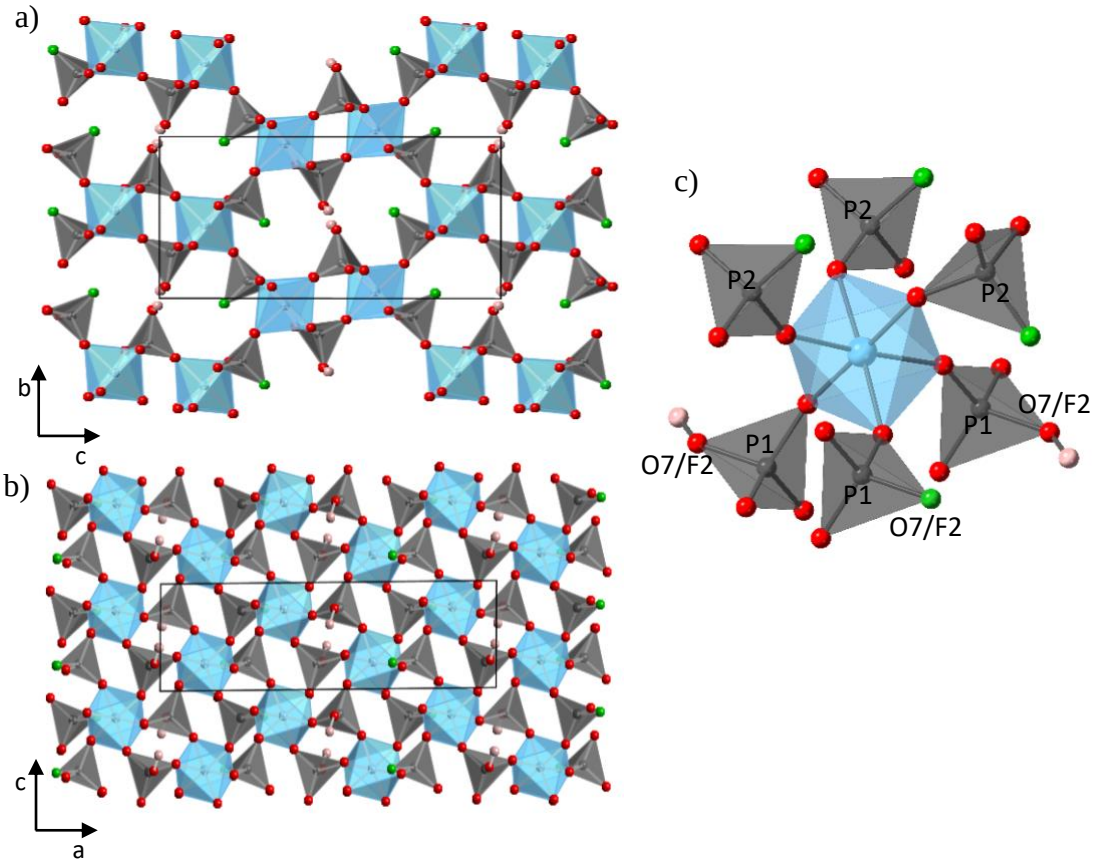

Figure 3.5 (a) Structure **V** viewed along the a-axis, (b) b-axis and (c) the coordination environment/connectivity of the Ti atom with $PO_3(F/OH)$ groups. Ti octahedra are shown in pale blue, PO_4H and PO_3F tetrahedra in grey and O, F, H atoms in red, green and pale pink respectively. The unit cell is outlined in black.

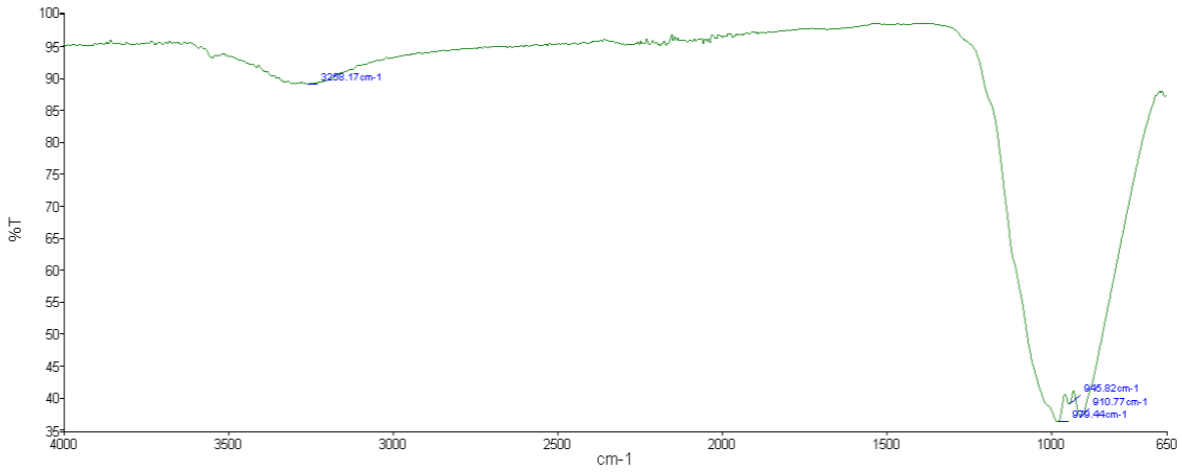

Figure 3.6 Infra-red spectra of Structure **V**.

As previously stated, the Ti(IV) centre is coordinated by six oxygens forming a regular octahedral geometry with Ti-O bond lengths all being approximately equal (~1.9 Å). The P-O bond lengths are also typical for the atoms involved as shown in Table 3.4, with elongation seen for the P-F/OH bonds.

Table 3.4 Table of bond lengths in structure **V**

Bond	Bond Length (Å)	Bond	Bond Length (Å)
Ti1-O1	1.967(4)	P1-O5	1.513(4)
Ti1-O2	1.917(4)	P1-O6	1.513(4)
Ti1-O3	1.907(4)	P1-O7/F2	1.573(4)
Ti1-O4	1.900(4)	P2-O1	1.519(4)
Ti1-O5	1.939(4)	P2-O2	1.509(4)
Ti1-O6	1.932(4)	P2-O4	1.524(4)
P1-O3	1.519(4)	P2-F1	1.554(4)

The partial occupation of the OH/F site is additionally supported by bond valence calculations as shown in Table 3.5 with P1 having a standard deviation of -0.23 v.u. and the O7/F2 site having a bond valence value of -2.33 v.u. This represents a deviation from the standard covalent/ionic bonding model used for bond valence calculations and further confirms the hydrogen bonding system suggested from SXRD structure solution.

Table 3.5 Table of bond valence values for atoms in Structure V

Atom Label	Bond Valence (v.u.)	Atom Label	Bond Valence (v.u.)
O1	1.92-	O7/F2	2.33-
O2	2.02-	F1	0.93-
O3	2.03-	P1	4.77+
O4	2.01-	P2	5.06+
O5	2.00-	Ti1	4.21+
O6	2.03-	H1	1.23+

The comparative PXRD shown in Figure 3.7 shows a good correlation between the SXRD model and the collected PXRD pattern, further confirming the solved SXRD model and showing very high phase purity of the sample.

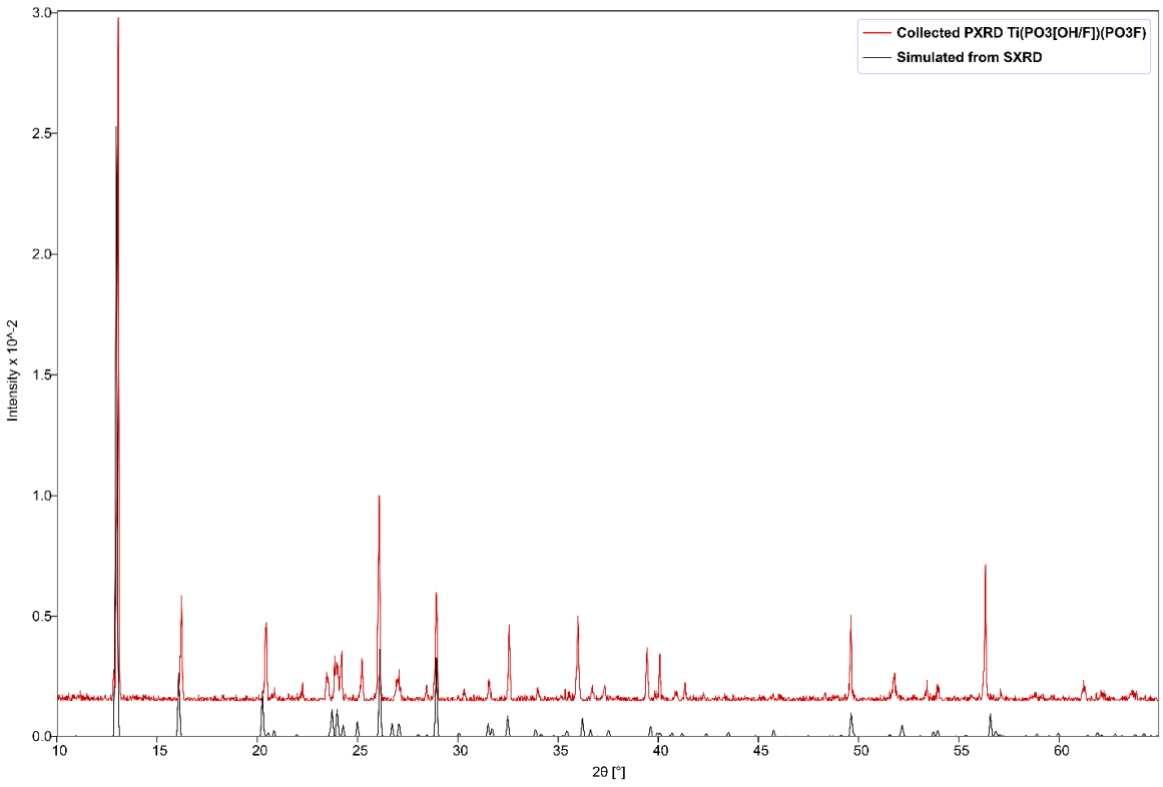

Figure 3.7 Comparison of collected PXRD pattern (red) with a simulated PXRD pattern from SXRD data (black) structure **V**.

3.4 Structure VI: $K_2Ti_2F_2(PO_4)(H[PO_4]_2)$

The product crystallised as colourless plate crystals, a suitable sample of which was selected for an SXRD study carried out at 150 K on a Bruker Nonius Kappa CCD diffractometer operating Mo Kα (λ = 0.7073 Å) radiation. Data collected were refined to a two-dimensional structure containing hydrogen-bonded layers of interconnected TiO_5F octahedra and PO_4 tetrahedra with potassium cations in the interlayer space (Figure 3.8). The solved structure shows a monoclinic unit cell in space group *C*2/*c*, the crystallographic information for structure **VI** is summarised in Table 3.6.

Table 3.6 Single crystal diffraction structure solution summary for structure **VI**

Empirical Formula	$K_2Ti_2F_2P_3O_{12}H$
Formula Weight ($gmol^{-1}$)	497.8439
Temperature (K)	150
Appearance	Colourless plates
Crystal size (mm)	0.02 x 0.04 x 0.05
Crystal system	Monoclinic
Space group	*C*2/*c*
Unit cell dimensions	a = 16.3325(3) b = 8.2898(2) c = 8.8089(2) β = 103.088(2)
λ/Å	0.71703 (Mo Kα)
Volume ($Å^3$)	1161.68(6)
Z	4
Density (gcm^{-3})	2.85
Reflections collected	12625
Unique reflections	1504
R_1 (all)	0.031
wR_2 (all)	0.076
GoF	1.087

The structure comprises of one crystallographically unique titanium centre which is octahedrally coordinated by five bridging oxide ions (1.894(4) to 1.950(4)Å) and one terminal fluoride ion (1.882(3)Å). The five oxygen atoms bridge to two unique phosphorous centres, P2 is the central phosphate group of the layers with bridging to 4 titanium atoms. P1 is the 'outer' phosphate group with three bridging oxygens and one terminal oxygen (O3) which points to the inter-layer space. The layers are stacked in an alternating configuration along the a-axis and are offset in the *c*- direction with the terminal oxygens of the P1 phosphate group hydrogen bonding at an interlayer distance of 2.51 Å. The inter-layer potassium cation is 9 co-ordinate with K-O distances of 2.643(4) to 3.053(5) Å and K-F distances of 2.643(3) to 2.782(3) Å and runs in zig-zag channels in between the layers.

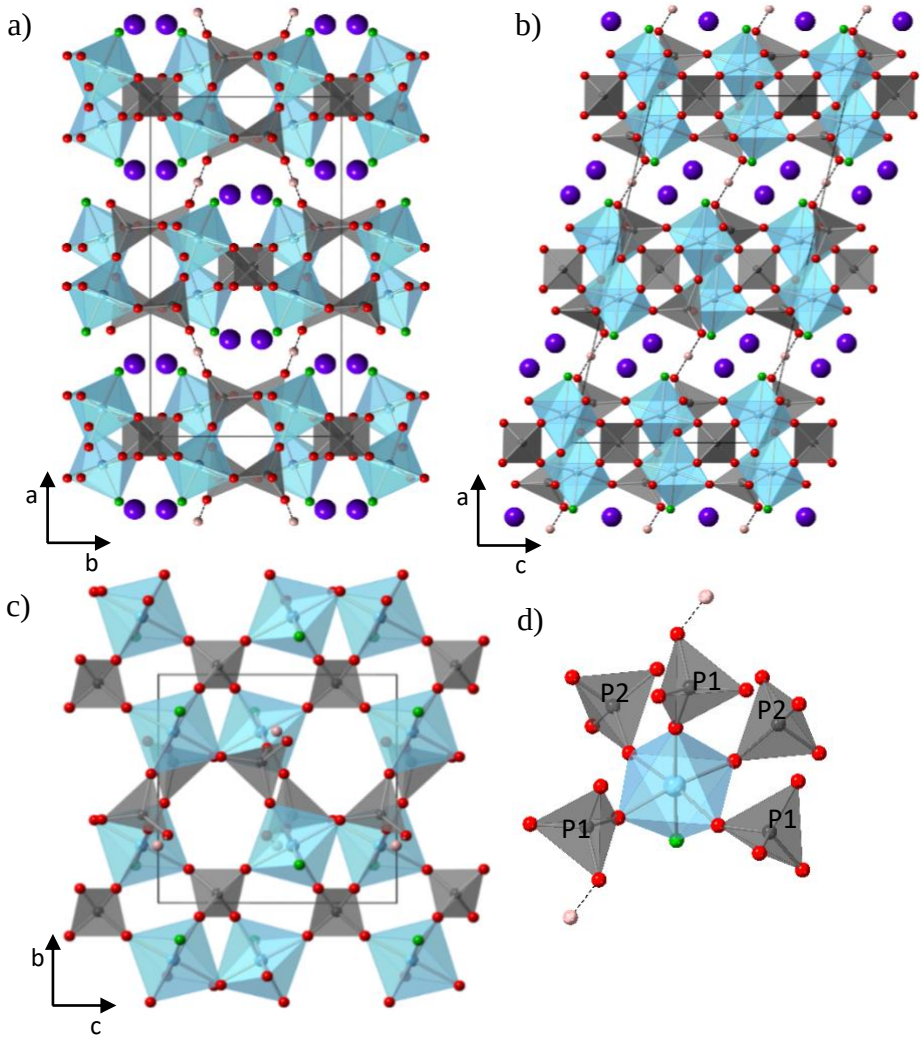

Figure 3.8 (a) Structure **VI** viewed along the c-axis, (b) b-axis, (c) a-axis (single layer) and (d) the coordination environment of the Ti octahedra. Ti octahedra shown in pale blue, PO_4 tetrahedra in grey and O, F, H atoms in red, green and pale pink respectively. The unit cell is outlined in black.

The layers of structure **VI** are isostructural with the layers of structure **I** but the difference between the interlayer cations (K^+ 2.20 Å vs Cs^+ 2.60 Å) and the additional hydrogen bonding between the hydrogen-phosphates rather than terminal fluorophosphates affects the stacking of the layers. The shortest O-O/F-F distances are 2.51 and 2.58 Å for structures **VI** and **I** respectively which shows that the hydrogen bonding and slightly smaller cation results in minimal shortening of the inter-layer distance.

The bond lengths shown in Table 3.7 are all typical for the atoms involved with the expected shortening of the Ti1/F1 bond.

Table 3.7 Table of bond lengths for structure **VI**

Bond	Bond Length (Å)	Bond	Bond Length (Å)
Ti1-O1	1.927(4)	P2-O1	1.522(4)
Ti1-O2	1.950(4)	P2-O4	1.524(4)
Ti1-O4	1.908(4)	K1-O1	2.820(4)
Ti1-O5	1.917(4)	K1-O2	2.939(4)
Ti1-O6	1.894(4)	K1-O3	2.821(4) 3.053(5)
Ti1-F1	1.882(3)		
P1-O2	1.528(4)	K1-O4	2.814(4)
P1-O3	1.535(4)	K1-O5	2.980(4)
P1-O5	1.530(4)	K1-F1	2.643(3) 2.714(4) 2.782(4)
P1-O6	1.532(4)		

The structure solution is supported by the bond valence values given in Table 3.8, with the hydrogen bonding model supported by the lower bond valence value calculated for O3.

Table 3.8 Bond valence values for atoms in structure **VI**

Atom Label	Bond Valence (v.u.)	Atom Label	Bond Valence (v.u.)
O1	2.12-	F1	1.07-
O2	2.04-	P1	5.00+
O3	1.93-	P2	5.12+
O4	2.12-	K1	1.15+
O5	2.05-	Ti1	4.18+
O6	2.03-	H1	0.93+

Comparative PXRD patterns displayed in Figure 3.9 show that there is a strong correlation between the solved crystal structure and the collected PXRD data and that the phase purity of the sample is high.

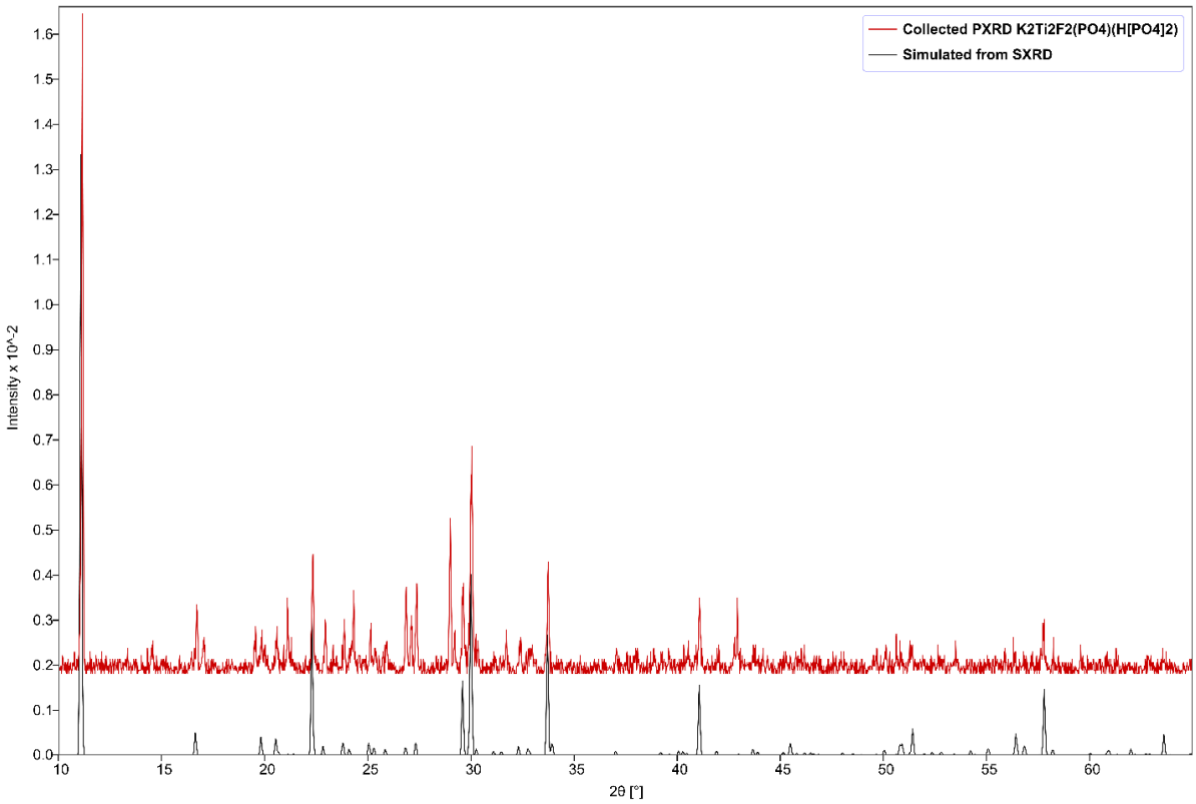

Figure 3.9 Comparison of collected PXRD pattern (red) with a simulated PXRD pattern from SXRD data (black) for structure **VI**.

Potassium titanyl phosphate ($KTiOPO_4$: KTP), was first discovered in 1974 by Tordjman *et al*. Since its discovery, KTP has been widely investigated for its non-linear optical properties, high thermal stability and a wide optical transmission window incorporating both UV and IR spectra. Similar properties are found in some isostructural $MTiOXO_4$ materials, for those where M = K, Rb, Cs or Tl and X = P or As. The KTP structure forms an orthorhombic unit cell in space group $Pna2_1$ with lattice parameters a = 12.814 Å, b = 6.404 Å and c = 10.616 Å. It is thought that the large non-linear optical and electro-optic coefficients in KTP is due to the net z-direction polarization formed within chains of alternating long and short Ti-O bonds. [9,15,16] As structure **VI** does not contain directly connected titanium octahedra, it is postulated that such non-linear optical and electro-optic properties would be diminished in this structure, the same assumption should be made of structure **I**.

3.5 Summary

An assortment of structural motifs and chemical compositions have been obtained from high fluoride hydrothermal reaction conditions utilising hexafluorotitanic acid and potassium hexafluorotitanate. The use of high fluoride reaction media resulted in successful incorporation of fluoride into the six new structures reported. All structures were fully solved from SXRD data collected and phase purity/structural solution checked with PXRD.

Most of the reactions required relatively harsh hydrothermal conditions of 200-210 °C for 3-4 days with structure **IV** produced under milder conditions of 175 °C for 4 days. It is noted that milder conditions were used in the very early reactions of this work but yielded mostly known amorphous products. Harsher reaction conditions were favoured as they more readily gave crystalline novel structures with the high fluoride titanium framework system. It appears that to drive the connectivity of the titanium frameworks, higher temperatures are required in this synthetic method.

Of the frameworks containing hydroxy-/fluoro-/phosphate tetrahedra, only two- and three-dimensional structures were obtained in this work. Lower dimensionality was observed in the hydroxy-/fluoro-/sulfate containing structure. In all structures, the titanium adopts the +4-oxidation state and regular octahedral co-ordination $Ti(O/F)_6$. Only structure **II** shows μ_2-bridging fluorides between titanium centres, whereas structures **I**, **IV** and **VI** contain titanium centres with terminal co-ordinated fluorides connected by hydroxy-/fluoro-/phosphate tetrahedra.

In terms of potential uses for these novel structures, structure **II** has the potential for good ion transport properties if the imidazolium cations could be removed from within its channels and replaced with lithium or sodium ions. The layered structures **I** and **VI** May also be of interest for ion-transport properties, again if the caesium and potassium cations can be deintercalated and replaced with lithium or sodium ions. Lithium and sodium intercalation could be tested by electrolysis

The article reported herein was cited twice since publication in 2014: by Slater *et.al.* in their article in October 2016 which reports the effect of oxoanion doping of $Na_2M(SO_4)_2{\cdot}2H_2O$ (M = transition metal) with selenite/fluorophosphate and by Zhang *et.al.* in June 2016 which reports a new mixed anion transition metal fluoride. [17,18]

3.6 References

(1) Rousse, G.; Tarascon, J. M. Sulfate-Based Polyanionic Compounds for Li-Ion Batteries: Synthesis, Crystal Chemistry, and Electrochemistry Aspects. *Chem. Mater.* **2014**, *26* (1), 394–406.

(2) Tajimi, S.; Ikeda, Y.; Uematsu, K.; Toda, K.; Sato, M. Enhanced Electrochemical Performance of $LiFePO_4$ Prepared by Hydrothermal Reaction. *Solid State Ionics* **2004**, *175* (1–4), 287–290.

(3) Armand, M.; Tarascon, J.-M. Building Better Batteries. *Nature* **2008**, *451* (7179), 652–657.

(4) Goodenough, J. B.; Kim, Y. Challenges for Rechargeable Li Batteries. *Chem. Mater.* **2010**, *22* (3), 587–603.

(5) Rouse, J.; Redrup, K. V; Kotsapa, E.; Weller, M. T. Controlling Dimensionality in Templated Layer, Chain and Framework Structures by Combining Metal Fluorides with Oxotetrahedra. *Chem. Commun.* **2009**, 7209–7211.

(6) Armstrong, J. A.; Williams, E. R.; Weller, M. T. Fluoride-Rich, Hydrofluorothermal Routes to Functional Transition Metal (Mn, Fe, Co, Cu) Fluorophosphates. *J. Am. Chem. Soc.* **2011**, *133*, 8252–8263.

(7) Armstrong, J. A.; Williams, E. R.; Weller, M. T. Manganese (III) Fluorophosphate Frameworks. *Dalt. Trans.* **2013**, *42*, 2302–2308.

(8) Recham, N.; Chotard, J. N.; Jumas, J. C.; Laffont, L.; Armand, M.; Tarasco, J. M. Ionothermal Synthesis of Li-Based Fluorophosphates Electrodes. *Chem. Mater.* **2010** .

(9) Canalias, C.; Nordlöf, M.; Pasiskevicius, V.; Laurell, F. A KTiOPO4 Nonlinear Photonic Crystal for Blue Second Harmonic Generation. *Appl. Phys. Lett.* **2009**, *94* (8).

(10) Delmas, C.; Nadiri, A.; Soubeyroux, J. L. The Nasicon-Type Titanium Phosphates Ati2(PO4)3(A=Li, Na) as Electrode Materials. *Solid State Ionics* **1988**, *28–30* (PART 1), 419–423.

(11) Essehli, R.; Bali, B. El; Benmokhtar, S.; Fejfarová, K.; Dusek, M. Hydrothermal Synthesis, Structural and Physico-Chemical Characterizations of Two Nasicon Phosphates: $M_{0.50}IITi_2(PO_4)_3$(M = Mn, Co). *Mater. Res. Bull.* **2009**, *44* (7), 1502–1510.

(12) Bamberger, C. E.; Begun, G. M.; Cavin, O. B. Synthesis and Characterization of Sodium-Titanium Phosphates, $Na_4(TiO)(PO_4)_2$, $Na(TiO)PO_4$, and $NaTi_2(PO_4)_3$. *J. Solid State Chem.* **1988**, *73* (2), 317–324.

(13) Sun, F.; Wang, R.; Jiang, H.; Zhou, W. Synthesis of Sodium Titanium Phosphate at Ultra-Low Temperature. In *Research on Chemical Intermediates*; 2013.

(14) Emsley, J. Very Strong Hydrogen Bonding. *Chem. Soc. Rev.* **1980**, *9* (1), 91.

(15) Norberg, S. T.; Ishizawa, N. K-Site Splitting in KTiOPO 4 at Room Temperature. *Acta Crystallogr. Sect. C Cryst. Struct. Commun.* **2005**, No. 61, 99–102.

(16) Bierlein, J. D.; Vanherzeele, H. Potassium Titanyl Phosphate : Properties and New Applications. **1989**, *6* (4), 622–633.

(17) Driscoll, L. L.; Kendrick, E.; Wright, A. J.; Slater, P. R. Investigation into the Effect on Structure of Oxoanion Doping in $Na_2M(SO_4)_2{\cdot}2H_2O$. *J. Solid State Chem.* **2016**, *242*, 103–111.

(18) Xu, D.; Zhang, F.; Sun, Y.; Yang, Z.; Dong, X.; Pan, S. Hydrogen Bond-Assisted Crystallization: Structure, Growth and Characterization of a New Mixed-Anion Transition Metal Fluoride $Na_3NH_4(TiF_6)(SO_4){\cdot}H_2O$. *New J. Chem.* **2016**, *40* (9), 7407–7413.

Chapter 4 : Titanium Fluorosulfates

4.0 Introduction

In Fe-based NASICON structures the replacement of $(PO_4)^{3-}$ with $(SO_4)^{2-}$ has been shown to improve the redox potential by 800mV which is attributed to the higher inductive effect on the iron centre. [1,2] As with the phosphates in the previous chapter, the addition of fluoride is thought to also increase the redox potential by the increased ionization of the M-F bond over the M-O bond. Many transition metal fluorosulfates have been synthesised and studied for their potential uses as Li-ion and Na-ion battery cathodes. By far the most studied is the $LiFeSO_4F$ tavorite phase with sodium and alternate 1st row transition metal analogues (Co, Cu and Ni) also being produced. [1,3–9]

Though a few titanium fluorophosphates have been reported, titanium fluorosulfates appear to be quite rare. The only reported synthesis for the binary titanyl fluorosulfate, $Ti(SO_3F)_4$, describes it as "a greenish-yellow resin-like material of limited thermal stability" for which the infrared spectra suggested an excess of HSO_3F present within the sample. In the same paper the authors refer to the synthesis of $Cs_2[Ti(SO_3F)_6]$ as a thermally stable salt which decomposes at 60-65 °C.[10] Titanium sulfates are also relatively under reported, $Ti_2(SO_4)_3$ and $TiO(SO_4)$ have both been investigated for sodium intercalation/deintercalation.[11,12] The titanium alums with general formula $ATi(SO_4)_2{\cdot}xH_2O$ were of interest for paramagnetic properties, in particular, the potassium and caesium analogues appear the most in the literature.[13–15]

The first new titanium (fluoro-/hydrogeno-)sulfate structure produced from this work was included in the article used as part of the previous chapter and showed one-dimensional chains of TiO_6 octahedra connected by SO_3(OH, F) groups with $[DABCO\text{-}H]^+$ molecular cations in the inter-chain space. This chapter will look at the further investigation of the high fluoride titanium sulfate system in pursuit of novel framework structures and reports the four novel phases published in a paper in the RSC journal Dalton Transactions entitled 'Synthesis and structural characterisation of transition metal fluoride sulfates'. As with the previous chapter these phases were produced under 'hydrofluorothermal' conditions which are reported in Table 4.1.

Table 4.1 Summary of reaction conditions for the titanium sulfates presented herein

Reagents	Temp (°C)	Time (h)	Crystal Morphology	Product formula	Section
H_2TiF_6 (5 mmol, 0.815 mL) Li_2SO_4 (5 mmol, 0.5497 g) H_2SO_4 (2.9 mmol, 0.28 mL)	210	72	Colourless tablets	$Li_{1.87}Ti_{1.13}F_{1.61}O_{0.39}(SO_4)_2$	4.1
TiF_3 (1 mmol, 0.10407 g) H_2SO_4 (5 mmol, 0.28 mL) NaF (3 mmol, 0.12614 g)	180	96	Colourless prisms	$Na_4TiF_4(SO_4)_2$	4.2
H_2TiF_6 (1 mmol, 0.16 mL) H_2SO_4 (3 mmol, 0.17 mL) 4,4'-bipy (1 mmol, 0.15630 g) NaF (2 mmol, 0.08900 g)	200	96	Colourless columns	$(C_{10}N_2H_{10})TiF_2(SO_4)_2$	4.3
H_2TiF_6 (1 mmol, 0.16 mL) H_2SO_4 (3 mmol, 0.17 mL) 4,4'-bipy (1 mmol, 0.15617 g) LiF (2 mmol, 0.05199 g)	200	96	Colourless prisms	$(C_{10}N_2H_{10})TiF_4SO_4$	4.4

4.1 Structure VII: $Li_{1.87}Ti_{1.13}F_{1.61}O_{0.39}(SO_4)_2$

The product crystallised as colourless tablets, a suitable sample of which was selected for an SXRD study carried out at 150 K on an Agilent SuperNova dual source EosS2 diffractometer operating Mo Kα (λ = 0.7073 Å) radiation. Data collected were initially refined to a one-dimensional chain structure of interconnected TiO_4F_2 octahedra and SO_4 tetrahedra with lithium cations in the inter-chain space. (Figure 4.1) with stoichiometric formula $Li_2TiF_2(SO_4)_2$. The solved structure showed am orthorhombic unit cell in space group *Cmca*. The crystallographic information for structure **VII** is summarised in Table 4.2.

Table 4.2 Single crystal diffraction structure solution summary for structure **VII**

Empirical Formula	$Li_{1.87}Ti_{1.13}F_{1.16}O_{8.39}S_2$
Formula Weight (gmol-1)	300.6
Temperature (K)	150
Appearance	Colourless tablets
Crystal size (mm)	0.111 x 0.073 x 0.030
Crystal system	Orthorhombic
Space group	*Cmca*
Unit cell dimensions	a = 5.1591(2) Å b = 13.6978(4) Å c = 9.4631(3) Å
λ/Å	0.71703 (Mo Kα)
Volume (Å3)	668.74 (4)
Z	4
Density (gcm-3)	2.99
Reflections collected	2300
Unique reflections	566
R1 (all)	0.031
wR2 (all)	0.080
GoF	1.166

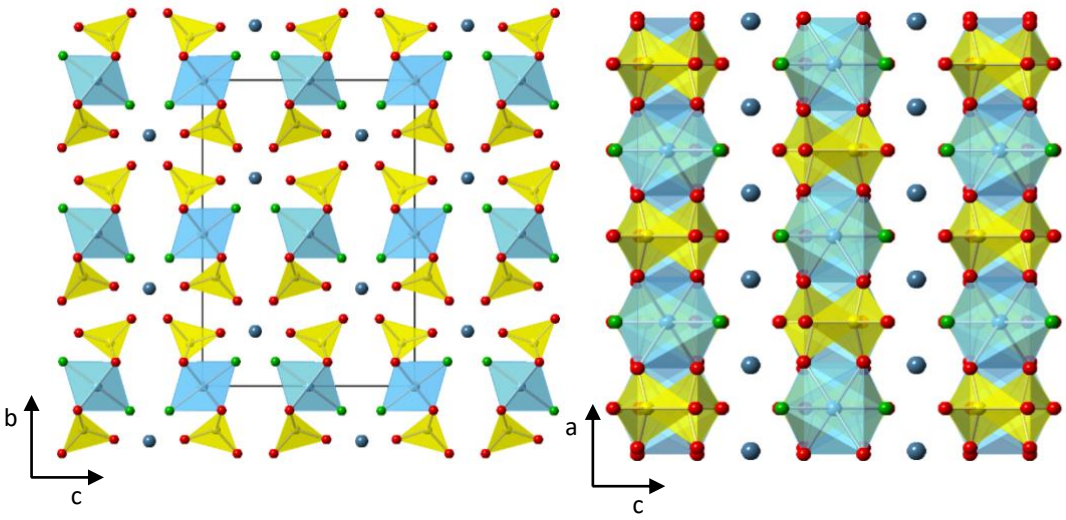

Figure 4.1 $Li_2TiF_2(SO_4)_2$ viewed down the a-axis (left) and b-axis (right). Ti octahedra are shown in pale blue, SO_4 tetrahedra in yellow and O, F and Li atoms in red, green and dark blue respectively. The unit cell is outlined in black.

The one-dimensional chains are comprised of *trans*-TiO_4F_2 octahedra each connected to the next in the chain by corner sharing with two sulfate tetrahedra. The terminal oxygens and fluorines of the chains form the octahedral coordination environment of the lithium cations. The *cis*-LiO_4F_2 octahedra face share with one another in the *a*-direction running parallel with the titanium fluoride sulfate chains as shown in Figure 4.2.

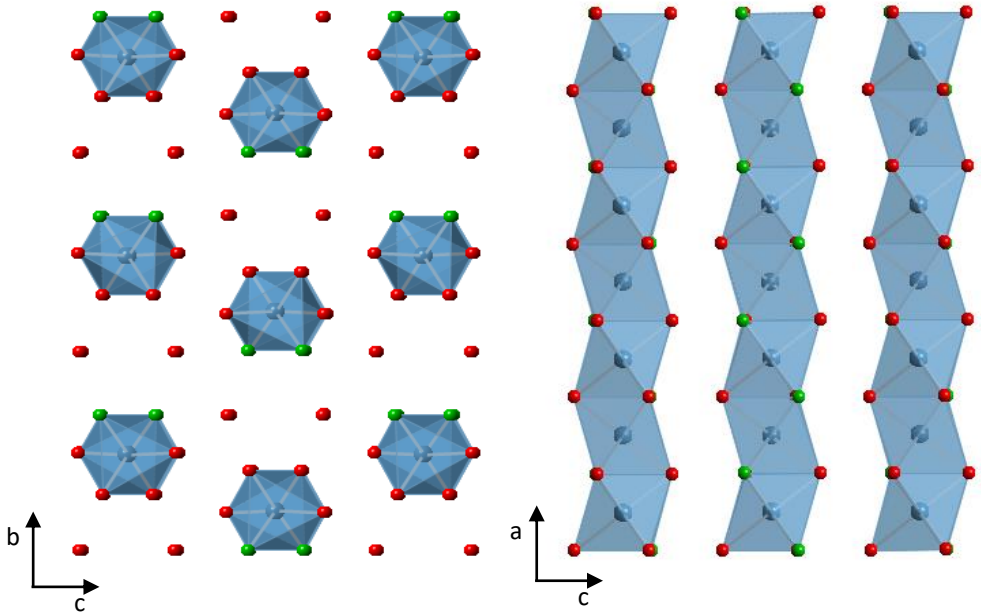

Figure 4.2 Face sharing chains of cis-LiO_4F_2 octahedra in $Li_2TiF_2(SO_4)_2$ with titanium and sulphur atoms removed. Li octahedra are shown in dark blue with oxygen and fluorine atoms in red and green respectively.

Table 4.3 Bond valence values for atoms in $Li_2iF_2(SO_4)_2$

Atom Label	Bond Valence (v.u.)	Atom Label	Bond Valence (v.u.)
Li1	1.14+	O1	2.01-
Ti1	4.16+	O2	2.01-
S1	6.07+	O3	2.11-
F1	1.04-		

Upon closer inspection of the lithium cation site and bond valence calculations (Table 4.3), it became apparent there was a very slight excess of electron density unaccounted for. This was attributed to a small percentage of cation disorder whereby a similarly sized Ti^{4+} cation (0.068 nm) substitutes the Li^{+} cation (0.060 nm).[16] This was successfully modelled and the Li:Ti ratio refined to 93:7. The resulting lithium poor stoichiometry was confirmed by Li atomic absorption spectroscopy (AAS). AAS measurements were taken by Alan Carver: Elemental analysis instrument technician, Department of Chemistry, Univesity of Bath. The instrument was calibrated with 5 and 10 ppm lithium solutions, and a curve fit used for the data. A solution was created by dissolving 0.0196 g of pure sample in 25 mL $HF/HNO_3/H_2O$ and 2 mL of this solution was diluted into 25 mL. Calculations for Li concentrations in ppm for the stoichiometric and the lithium poor compositions are shown in Equation 4.1 – 4.4.

$Li_2TiF_2(SO_4)_2$:

$$Concentration = \frac{0.0196\ g}{291.857\ gmol^{-1}} \times 40 = 2.70 \times 10^{-3} M \quad \text{Equation 4.1}$$

$$Mass\ (Li) = 2.70 \times 10^{-3}\ M\ \times\ (2 \times 6.941\ gmol^{-1}) = 0.037\ gL^{-1}\ = \mathbf{37\ ppm} \quad \text{Equation 4.2}$$

$Li_{1.87}Ti_{1.13}O_{0.39}F_{1.61}(SO_4)_2$:

$$Concentration = \frac{0.0196\ g}{296.020\ gmol^{-1}} \times 40 = 2.65 \times 10^{-3} M \quad \text{Equation 4.3}$$

$$Mass\ (Li) = 2.65 \times 10^{-3}\ M\ \times\ (2 \times 6.941\ gmol^{-1}) = 0.034\ gL^{-1}\ = \mathbf{34\ ppm} \quad \text{Equation 4.4}$$

The reading from the spectrometer gave a concentration of 2.6 ppm, multiplying by the dilution factor (12.5) gives a concentration of 33 ppm. This strongly correlates with the lithium poor stoichiometry calculation, confirming the stoichiometry calculated from the single crystal data. The excess positive charge created by replacing 7% of the Li^{+} cations with Ti^{4+} cations was balanced by partial substitution of terminal F^{-} anions by O^{2-} anions with an F:O ratio of 81:19.

The bond lengths for structure **VII** (Table 4.4) are as expected for the elements involved with shorter bonds for M-F than M-O (M=Ti/Li) due to the higher electronegativity and smaller ionic radius of fluorine.

Table 4.4 Bond lengths within structure **VII**

Bond	Bond Length (Å)	Bond	Bond Length (Å)
Ti/Li1-O2	2.092(3)	Ti2-O4/F2	1.852(2) x2
Ti/Li1-O3	2.039(2)	Ti2-F1	1.852(2) x2
Ti/Li1-F2/O4	2.025(3)	S1-O1	1.499(2) x2
Ti/Li1-F1	2.025(3) x2	S1-O2	1.499(3)
Ti2-O1	1.941(2) x2	S1-O3	1.460(3)

A PXRD pattern simulated from the solved SXRD data matched very well with the PXRD pattern collected from a ground sample, as shown in Figure 4.3. This further confirms the single crystal structure solution and suggests high sample purity is obtained from the synthetic reaction.

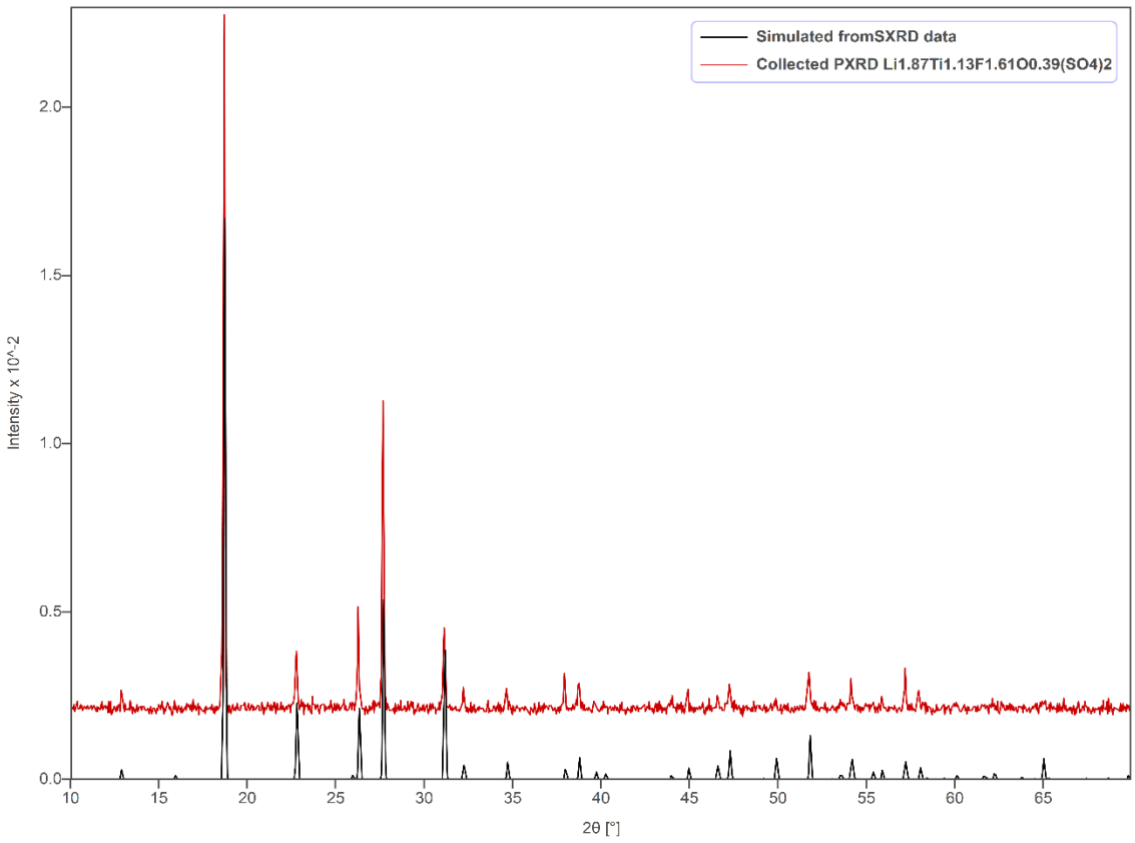

Figure 4.3 Comparison of collected PXRD pattern (red) with simulated PXRD pattern from SXRD data (black) for $Li_{1.87}Ti_{1.13}O_{0.39}F_{1.61}(SO_4)_2$

Figure 4.4 shows collected SEM images of selected crystals of $Li_{1.87}Ti_{1.13}O_{0.39}F_{1.61}(SO_4)_2$. The image on the left of Figure 4.4 shows a smooth and a defected crystal next to one another, and the image on the right shows a x2 magnification of a defected crystal. Defects in these crystals are likely due to disorder caused by the partial substitution of lithium by titanium.

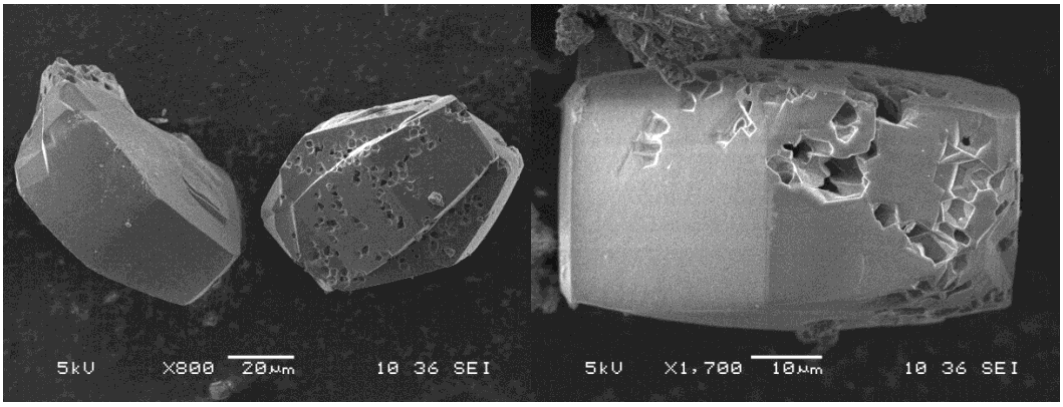

Figure 4.4 SEM images of crystals of $Li_{1.87}Ti_{1.13}O_{0.39}F_{1.61}(SO_4)_2$

The one-dimensional nature originally attributed to this structure ruled out the interest in ion-transport due to lack of stability of the de-intercalated material but the partial substitution of some lithium sites with titanium has the possibility of extending the connectivity to a three-dimensional framework.

4.2 Structure VIII: $Na_4TiF_4(SO_4)_2$

The product crystallised as colourless prismatic crystals, a suitable sample of which was selected for an SXRD study carried out at 150 K on an Agilent SuperNova dual source EosS2 diffractometer operating Mo Kα (λ = 0.71073 Å) radiation. Data collected were refined to a structure containing discreet polyanionic units of formula $[TiF_4(SO_4)_2]_{4-}$ separated by sodium cations. The structure shows a triclinic unit cell in space group $P\bar{1}$, the crystallographic information for structure **VIII** is summarised in Table 4.5.

Table 4.5 Single crystal diffraction structure solution summary for structure **VIII**

Empirical Formula	$Na_4TiF_4S_2O_8$
Formula Weight (gmol-1)	407.95
Temperature (K)	150
Appearance	Colourless prism
Crystal size (mm)	0.078 x 0.082 x 0.136
Crystal system	Triclinic
Space group	*P*-1
Unit cell dimensions	a = 5.5997(10) Å b = 6.6012(12) Å c = 6.6657(12) Å α = 86.361(15) ° β = 82.230 (15) ° γ = 74.777(16) °
λ/Å	0.71703 (Mo Kα)
Volume (Å3)	235.47 (8)
Z	1
Density (gcm-3)	2.88
Reflections collected	1075
Unique reflections	957
R1 (all)	0.040
wR2 (all)	0.096
GoF	1.093

The single crystallographically distinct titanium atom is six-fold coordinated by four terminal fluoride ions and two bridging oxygens of two SO_4 tetrahedra as shown in Figure 4.5. Thus, the discreet polyanion is formed from one TiF_4O_2 octahedron bonded to two SO_4 tetrahedra through corner sharing oxygen atoms. These discreet polyanion units are aligned above one another in each of the three cell dimensions. There are two crystallographically distinct sodium environments in this structure, each being seven-fold coordinated. Na1 is coordinated by three oxygens (2.335(2) to 2.661(3) Å) and three fluorines (2.294(2) to 2.490(2) Å), while Na2 is coordinated by four oxygens (2.375(2) to 2.762(3) Å) and two fluorines (2.376(2) to 2.422(2) Å).

Table 4.6 shows that the bond lengths within structure **VIII** are typical for the atoms involved with slightly shorter Ti-F bonds (1.837/1.878 Å) compared to Ti-O (1.944 Å). The bond valence values reported in Table 4.7 support the formula produced from the SXRD structure solution with Ti in the common +4 oxidation state.

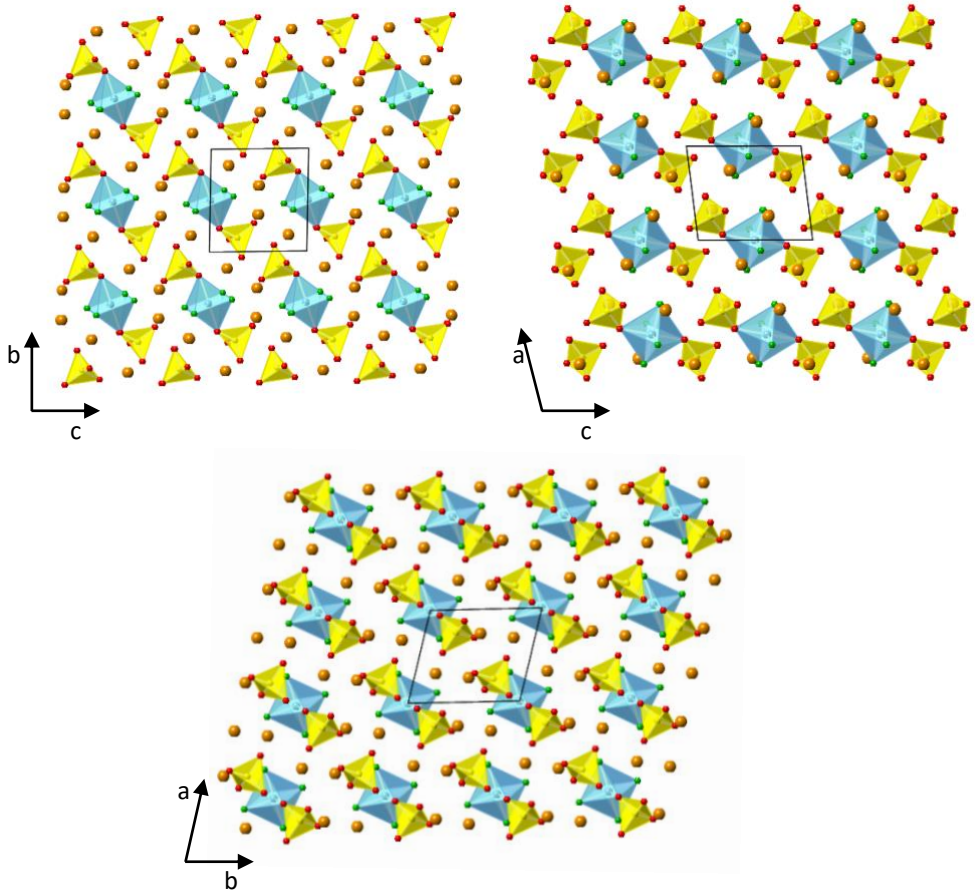

Figure 4.5 Structure **VIII** viewed down the a-axis (top left), b-axis (top right) and c-axis(bottom). Ti octahedra are shown in pale blue, SO_4 tetrahedra in yellow and Na, O, F atoms in orange, red and green respectively. The unit cell is outlined in black.

Table 4.6 Table of bond lengths in structure **VIII**

Bond	Bond Length (Å)	Bond	Bond Length (Å)
Ti1-F1	1.837(2) x2	Na1-F1	2.490(2)
Ti1-F2	1.878(2) x2	Na1-F2	2.294(2)
Ti1-O4	1.944(2) x2		2.383(2)
S1-O1	1.445(2)	Na2-O1	2.427(3)
S1-O2	1.459(2)	Na2-O2	2.375(2)
S1-O3	1.467(2)		2.545(3)
S1-O4	1.527(2)	Na2-O3	2.398(2)
Na1-O1	2.335(2)	Na2-O4	2.762(3)
Na1-O2	2.611(3)	Na2-F1	2.376(2)
Na1-O3	2.349(2)	Na2-F2	2.422(2)
	2.545(2)		

Table 4.7 Bond valence values for atoms in structure **VIII**

Atom Label	Bond Valence (v.u.)	Atom Label	Bond Valence (v.u.)
Na1	1.16+	O4	2.11-
Na2	1.12+	F1	1.02-
O1	2.03-	F2	1.10-
O2	2.00-	S1	5.99+
O3	2.08-	Ti1	4.13+

The phase purity of this sample was high and the collected PXRD pattern matches very well with the pattern simulated from the solved SXRD data as shown in Figure 4.6, confirming the structure solution from SXRD data.

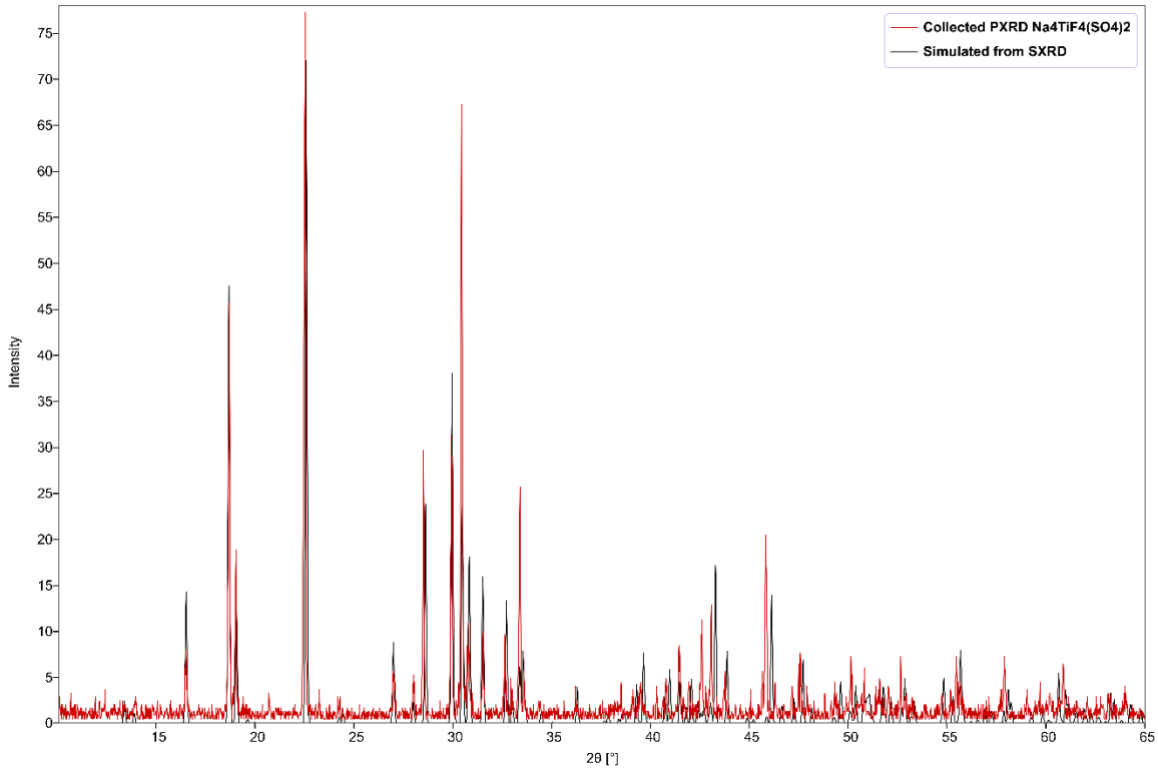

Figure 4.6 Comparison of collected PXRD pattern (red) with simulated PXRD pattern from SXRD data (black) for structure **VIII**.

4.3 Structure IX: $[C_{10}N_2H_{10}][TiF_2(SO_4)_2]$

The product crystallised as colourless columns/rod-shaped crystals, a suitable sample of which was selected for an SXRD study carried out at 150 K on an Agilent Xcalibur EosS2 diffractometer operating Mo Kα (λ = 0.71073 Å) radiation. Data collected were refined to a structure containing one-dimensional chains of interconnected TiO_4F_2 octahedra and SO_4 tetrahedra with double protonated 4,4'-bipyridine molecular cations in the interchain space (Figure 4.7). The structure shows a triclinic unit cell in space group $P\bar{1}$. The crystallographic information for structure **IX** is summarised in Table 4.8.

Table 4.8 Single crystal diffraction structure solution summary for structure **IX**

Empirical Formula	$C_{10}N_2H_{10}TiF_2S_2O_8$
Formula Weight (gmol-1)	436.19
Temperature (K)	150
Appearance	Colourless columns
Crystal size (mm)	0.041 x 0.046 x 0.198
Crystal system	Triclinic
Space group	*P*-1
Unit cell dimensions	a = 4.5768(3) Å b = 8.9162(6) Å c = 10.1236(9) Å α = 112.888(7) ° β = 95.196(6) ° γ = 98.706(5) °
λ/Å	0.71703 (Mo Kα)
Volume (Å3)	371.11(14)
Z	1
Density (gcm-3)	1.46
Reflections collected	5670
Unique reflections	1772
R1 (all)	0.045
wR2 (all)	0.079
GoF	1.043

As in the initial structure solution for structure **VII**, there is one crystallographically unique titanium centre within the structure which is octahedrally coordinated by four oxygens and two *trans*-fluorines. One crystallographically unique sulfur forms sulfate tetrahedra which vertex shares with the titanium centres forming one-dimensional chains which run infinitely in the *a*-direction. The Ti-Ti distance is shorter in structure **IX** than in structure **VII**, as shown in Figure 4.8. The doubly protonated 4,4'-bipyridyl cations form hydrogen bonds with the terminal oxygens of the sulfate groups with C/N-H···O distances of 1.89(3) to 2.38(1) Å and stack directly above one another in the *a*-direction (Figure 4.7). The

hydrogen bonding of the organo-cation is likely the cause of the shorter Ti-Ti distance in structure **VII**.

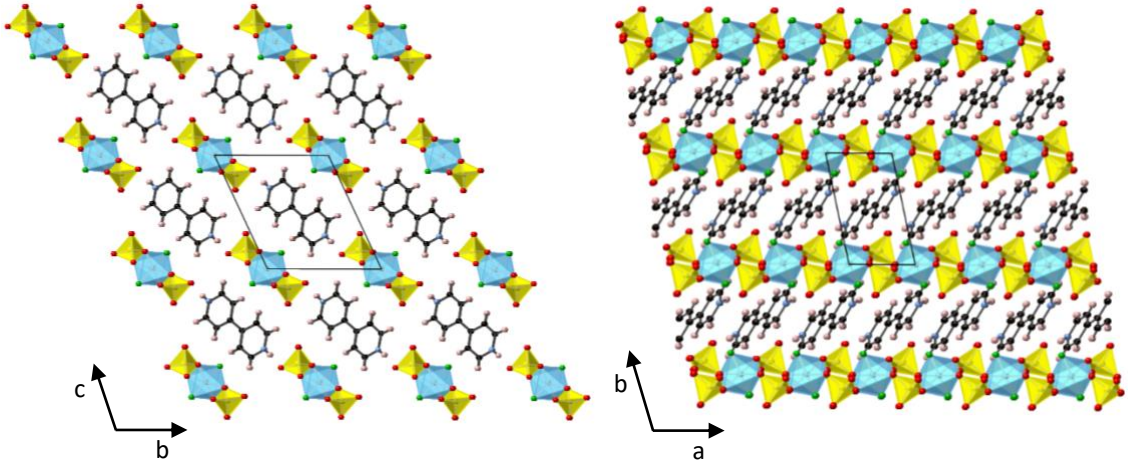

Figure 4.7 Structure **IX** viewed along the a-axis (left) and c-axis (right). Ti octahedra are shown in pale blue, SO_4 tetrahedra in yellow and O, F, C, N, H atoms in red, green, black, blue and pale pink respectively. The unit cell is outlined in black.

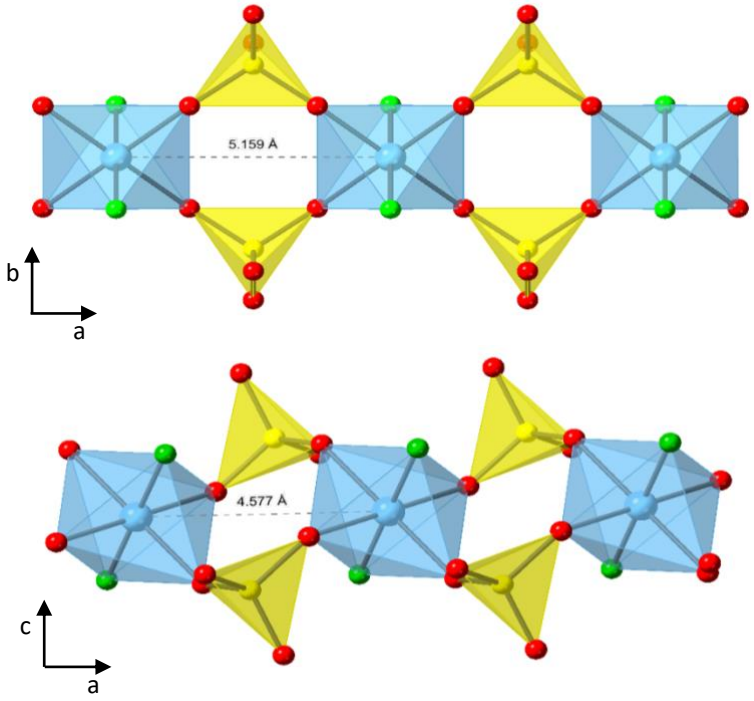

Figure 4.8 Comparison of titanium fluoride sulfate chains in structure **VII** (top) with structure **IX** (bottom). Titanium octahedra in pale blue, sulphate tetrahedra in yellow and oxygen and fluorine atoms in red and green respectively.

The bond lengths within the structure are all typical for the elements involved (

Table 4.9) and as seen in the previous structures shorter Ti-F bonds result in slightly distorted Ti octahedra. It is also noted that the terminal S-O bonds of the sulfate group are

shorter than the titanium bridging S-O bonds which is attributed to the attraction of electron density towards the hydrogen bond with the N-H of the doubly protonated 4,4'-bipyridyl molecular cations.

Table 4.9 Table of bond lengths in structure **IX**

Bond	Bond Length (Å)	Bond	Bond Length (Å)
Ti1-F1	1.810(1) x2	N1-C6	1.330(3) x2
Ti1-O1	1.963(2) x2	N1-C1	1.339(3) x2
Ti1-O2	1.967(2) x2	C1-C3	1.377(3) x2
S1-O1	1.510(2)	C4-C3	1.397(3) x2
S1-O2	1.503(2)	C4-C4	1.493(4)
S1-O4	1.455(2)	C4-C5	1.388(3) x2
S1-O5	1.436(2)	C5-C6	1.377(3) x2

The comparison of the collected PXRD with the powder pattern simulated from the solved SXRD data (Figure 4.9) shows low sample purity which was approximated to be 40% from visual inspection during single crystal selection.

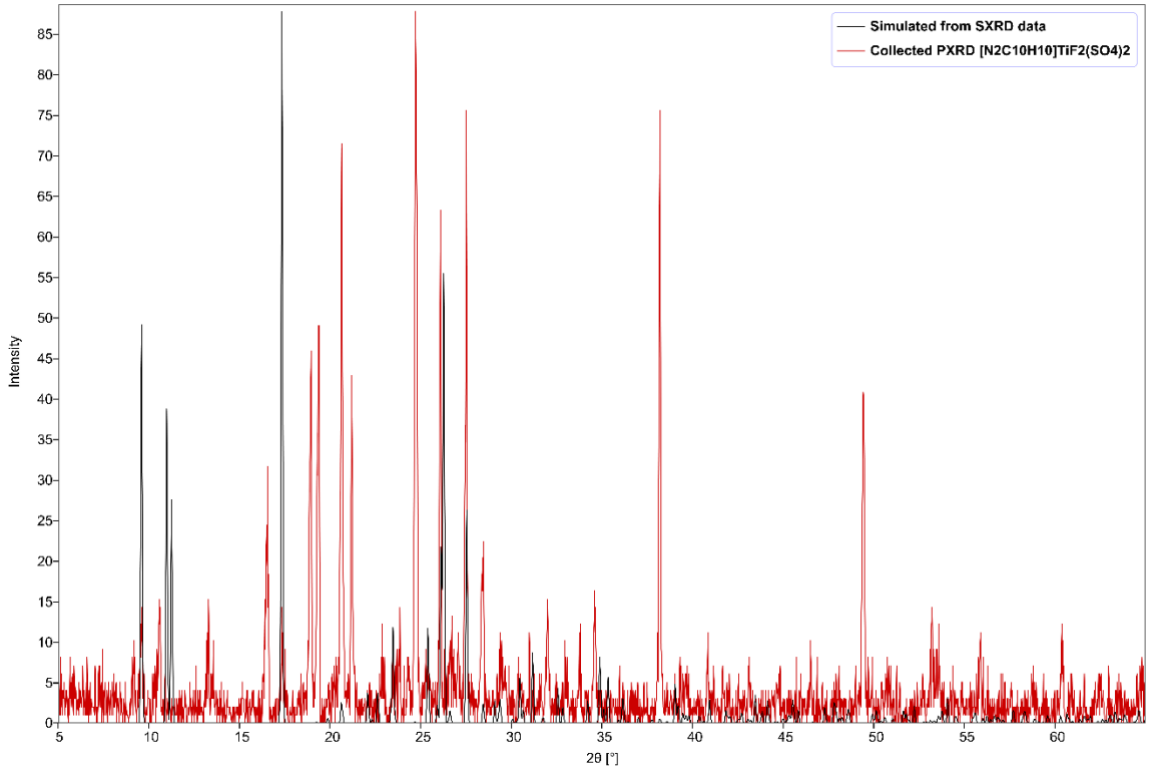

Figure 4.9 Comparison of collected PXRD pattern (red) with simulated PXRD pattern from SXRD data (black) for structure **IX**.

4.4 Structure X: $[C_{10}N_2H_{10}]TiF_4SO_4$

The product crystallised as colourless prismatic crystals, a suitable sample of which was selected for an SXRD study carried out on an Agilent Xcalibur EosS2 diffractometer operating Mo Kα (λ = 0.71073 Å) radiation. Data collected were refined to a one-dimensional structure containing discreet polyanionic units of formula $[(TiF_4SO_4)_2]_{4-}$ separated by doubly protonated 4,4'-bipyridine molecular cations in a twisted conformation as shown in Figure 4.10. The structure shows a triclinic unit cell in space group $P\bar{1}$. The crystallographic information is summarised in Table 4.10.

Table 4.10 Single crystal diffraction structure solution summary for structure **X**

Empirical Formula	$C_{10}N_2H_{10}TiF_4SO_4$
Formula Weight (gmol-1)	378.1
Temperature (K)	150
Appearance	Colourless prism
Crystal size (mm)	0.043 x 0.061 x 0.126
Crystal system	Triclinic
Space group	*P*-1
Unit cell dimensions	a = 8.691(2) Å b = 9.208(2) Å c = 9.289(2) Å α = 68.56(2) ° β = 84.30(2) ° γ = 81.59(2) °
λ/Å	0.71703 (Mo Kα)
Volume (Å3)	683.6(7)
Z	2
Density (gcm-3)	1.84
Reflections collected	5816
Unique reflections	3133
R1 (all)	0.103
wR2 (all)	0.136
GoF	1.029

The discreet complex polyhedral anion is comprised of two *cis*-TiF_4O_2 octahedra bridged by two sulfate tetrahedra. There is one crystallographically distinct titanium and sulphur centre within the structure which is bridged by a μ_2-oxygen. As with structure **VIII** the discreet units align directly above one another in all three directions. The twisted doubly protonated 4,4'-bipyridyl molecular cations lie between the discreet complex polyanion units and form hydrogen bonds with the terminal oxide and fluoride ions with N-H···O/F distances between 2.04(5) to 2.38(4) Å.

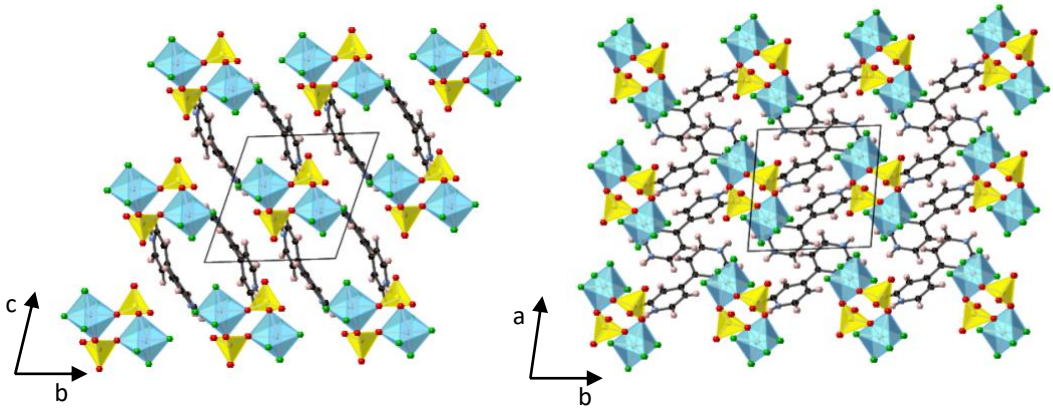

Figure 4.10 Structure **X** viewed along the a-axis (left) and c-axis (right). Ti octahedra are shown in pale blue, SO_4 tetrahedra in yellow and O, F, C, N, H atoms in red, green, black, blue and pale pink respectively. The unit cell is outlined in black.

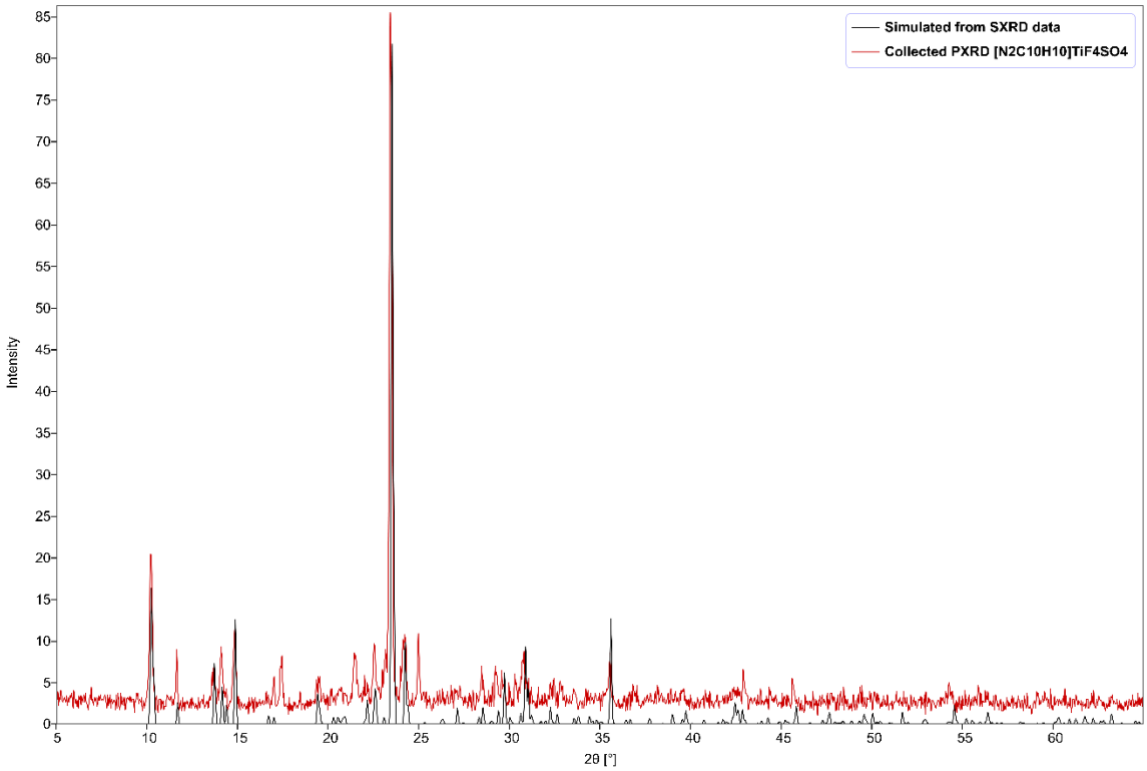

Figure 4.11 Comparison of collected PXRD pattern (red) with simulated PXRD pattern from SXRD data (black) for structure **X**.

High sample purity and good match between the collected PXRD and simulated from SXRD powder patterns is shown in Figure 4.11. The bond lengths reported in Table 4.11 are all typical for the elements involved, with the shorter terminal S-O bonds due to hydrogen bonding with the doubly protonated 4,4'-bipyridine molecular cations as previously seen in structure **IX**.

Table 4.11 Table of bond lengths in structure **X**

Bond	Bond Length (Å)	Bond	Bond Length (Å)
Ti1-F1	1.851(2)	N2-C9	1.340(6)
Ti1-F2	1.808(3)	N2-C10	1.331(6)
Ti1-F3	1.821(2)	C1-C2	1.488(6)
Ti1-F4	1.812(2)	C1-C7	1.392(6)
Ti1-O5	2.057(3) x2	C1-C8	1.384(6)
S1-O1	1.504(3)	C2-C3	1.385(6)
S1-O5	1.510(3)	C2-C6	1.397(6)
S1-O7	1.447(3)	C3-C4	1.370(6)
S1-O8	1.447(3)	C5-C6	1.372(6)
N1-C4	1.336(6)	C7-C10	1.374(6)
N1-C5	1.330(6)	C8-C9	1.378(6)

4.5 Conclusion

Four new structures based on the titanium fluoride sulfate system have been successfully synthesised and their crystal structures determined via single crystal X-ray diffraction. Phase purity and structure solution from SXRD was checked with PXRD for each sample. As seen in the previous chapter, relatively harsh hydrofluorothermal conditions were utilised (approx. 200 °C for three or four days) to achieve novel crystalline phases from reaction mixtures containing hexafluorotitanate reagents, while structure **VIII** was prepared in slightly milder conditions (170 °C for four days) from TiF_3.

$Na_4TiF_4(SO_4)_2$ is the only phase produced from this work which did not utilise hexafluorotitanic acid, or potassium hexafluorotitanate. Rather, the reaction mixture $Na_4TiF_4(SO_4)_2$ contained TiF_3, NaF and H_2SO_4. It is worth noting that many reactions were trialled with TiF_3 and TiF_4 as the titanium source but most of these reactions produced known or uncollectable samples due to dissolution on filtration. It is postulated that these products were simple salts which explained why they dissolved so readily in water; therefore, effort was not made to re-produce or crystallise dissolved phases.

Of the four phases reported herein, the highest dimensionality was seen for structure **VII** $Li_{1.87}Ti_{1.13}O_{0.39}F_{1.61}(SO_4)_2$ which is considered as one-dimensional chains additionally linked by partial occupation of the lithium site by titanium(IV) cations. A true one-dimensional chain structure was reported for structure **VIII** with protonated organoamine molecular cations in the interchain space. The other two structures show zero dimensionality with discreet polyhedral units separated by sodium ions and molecular cations. It would appear from these results that lower dimensionality is favoured by the titanium fluoride sulfate system.

Unlike some of the structures in the previous chapter in which fluoride was incorporated into the phosphate group, none of the structures reported here is a true fluorosulfate but rather all are fluoride sulfates where the fluoride ions are coordinated to the titanium centres rather than the sulfate group. This likely explains the tendency for lower dimensionality within these systems as it is quite rare for fluorine atoms to bridge between polyhedral units.

4.6 References

(1) Ati, M.; Dupont, L.; Recham, N.; Chotard, J. N.; Walker, W. T.; Davoisne, C.; Barpanda, P.; Sarou-Kanian, V.; Armand, M.; Tarascon, J. M. Synthesis, Structural, and Transport Properties of Novel Bihydrated Fluorosulphates $NaMSO_4F\ 2H_2O$ (M=Fe, Co, and Ni). *Chem. Mater.* **2010**, *22* (13), 4062–4068.

(2) Padhi, A. K.; Nanjundaswamya, K. S.; Masquelier, C.; Goodenough, J. B. Mapping of Transition Metal Redox Energies in Phosphates with NASICON Structure by Lithium Intercalation. *J. Electrochem. Soc.* **1997**, *144* (8), 2581–2586.

(3) Melot, B. C.; Rousse, G.; Chotard, J. N.; Ati, M.; Rodríguez-Carvajal, J.; Kemei, M. C.; Tarascon, J. M. Magnetic Structure and Properties of the Li-Ion Battery Materials $FeSO_4F$ and $LiFeSO_4F$. *Chem. Mater.* **2011**, *23* (11), 2922–2930.

(4) Sun, M.; Rousse, G.; Corte, D. D.; Saubanère, M.; Doublet, M. L.; Tarascon, J. M. A Fully Ordered Triplite, $LiCuSO_4F$. *Chem. Mater.* **2016**, *28* (6), 1607–1610.

(5) Ati, M.; Sougrati, M. T.; Rousse, G.; Recham, N.; Doublet, M. L.; Jumas, J. C.; Tarascon, J. M. Single-Step Synthesis of $FeSO_4F_{1-y}OHy(0 \leq y \leq 1)$ Positive Electrodes for Li-Based Batteries. *Chem. Mater.* **2012**, *24* (8), 1472–1485.

(6) Lander, L.; Reynaud, M.; Rousse, G.; Sougrati, M. T.; Laberty-Robert, C.; Messinger, R. J.; Deschamps, M.; Tarascon, J. M. Synthesis and Electrochemical Performance of the Orthorhombic $Li_2Fe(SO_4)_2$ polymorph for Li-Ion Batteries. *Chem. Mater.* **2014**, *26* (14), 4178–4189.

(7) Tripathi, R.; Gardiner, G. R.; Islam, M. S.; Nazar, L. F. Alkali-Ion Conduction Paths in $LiFeSO_4F$ and $NaFeSO_4F$ Tavorite-Type Cathode Materials. *Chem. Mater.* **2011**, *23* (8), 2278–2284.

(8) Recham, N.; Rousse, G.; Sougrati, M. T.; Chotard, J. N.; Frayret, C.; Mariyappan, S.; Melot, B. C.; Jumas, J. C.; Tarascon, J. M. Preparation and Characterization of a Stable $FeSO_4F$-Based Framework for Alkali Ion Insertion Electrodes. *Chem. Mater.* **2012**, *24* (22), 4363–4370.

(9) Recham, N.; Chotard, J.-N.; Dupont, L.; Delacourt, C.; Walker, W.; Armand, M.; Tarascon, J.-M. A 3.6 V Lithium-Based Fluorosulphate Insertion Positive Electrode for Lithium-Ion Batteries. *Nat. Mater.* **2010**, *9* (1), 68–74.

(10) MISTRY, F.; AUBKE, F. The Synthesis and Vibrational-Spectra of Fluorosulfate Derivatives of Titanium, Zirconium and Hafnium. *J. Fluor. Chem.* **1994**, *68* (3), 239–248.

(11) Senguttuvan, P.; Rousse, G.; Vezin, H.; Tarascon, J.-M.; Palacín, M. R. Titanium(III) Sulfate as New Negative Electrode for Sodium-Ion Batteries. *Chem. Mater.* **2013**, *25* (12), 2391–2393.

(12) Gnanavel, M.; Raveau, B.; Pralong, V. Electrochemical Li/Na Intercalation in $TiOSO_4$, First Member of the Phosphate Tungsten Bronze-Type Family. *J. Electrochem. Soc.* **2015**, *162* (3), A465–A469.

(13) Sygusch, J. Refinement of Beta-Alum $CsTi(SO_4)_2.12H_2O$. *Acta Crystallogr. Sect. B* **1974**, *30* (3), 662–665.

(14) Best, S. P.; Beattie, J. K.; Armstrong, R. S. Vibrational Spectroscopic Studies of Trivalent Hexa-Aqua-Cations: Single-Crystal Raman Spectra between 275 and 1200 Cm-1 of the Caesium Alums of Titanium, Vanadium, Chromium, Iron, Gallium and Indium. *J. Chem. Soc. Dalt. Trans.* **1984**, 2611–2624.

(15) Domenech-Carbo, A. Electrochemistry of Aluminosilicates. In *Electrochemistry of Porous Materials*; CRC Press, 2009; pp 69–94.

(16) Guo, Q.; Wang, Q.; Chen, G.; Shen, M.; Li, B. Molten Salt Synthesis of Different Ionic Radii Metallic Compounds Doped Lithium Titanate Used in Li-Ion Battery Anodes. *Mater. Trans.* **2017**, *58* (3), 383–389.

Chapter 5 : Manganese Frameworks

5.0 Introduction

As well as titanium, manganese-based frameworks are of interest due to the possibility of accessing the (+4/+3) redox potential for electrode materials. In particular, A_2MnPO_4F (A = Na/Li) has been investigated as a potential two cation transfer cathode material, though only one cation was feasibly transferred in the working voltage window.[1] Though several lithium and sodium manganese framework structures have been reported and studied for their electrochemical performance, it was theorised that new and interesting properties may arise from manganese frameworks incorporating a mixture of lithium and sodium ions in a similar manner to the $LiNaFe(PO_4)F$ phase reported by BenYahia *et. al*.[2] The reactions for this work were carried out by an undergraduate project student (Stefanie Zekoll) and all SXRD data collection and data refinement carried out by the author of this work. The syntheses involved high fluoride reaction meadia treated under hydrothermal conditions. Three novel structures were obtained and are reported herein in sections 5.1-5.3.

Further investigation of manganese frameworks was carried out by the author under classical high temperature synthetic conditions with the aim of mixing the polycationic system to create manganese borate/phosphate frameworks with mobile lithium and sodium cations. Open framework borophosphate and borate phosphate structures have been reported for cobalt, manganese, iron and titanium, all obtained via hydrothermal synthesis techniques.[3–8] Of particular interest in terms of electrochemically active materials, $Li_{0.8}Fe(H_2O)_2[BP_2O_8]\cdot H_2O$ was investigated as a Li- and Na- battery anode material, showing promising ion mobility and voltage from electrochemical impedance spectroscopy (EIS).[9] Though over twenty ceramic synthetic reactions were carried out only two of these reactions yielded novel structures as shown in sections 5.4 and 5.5. Some hydrothermal reactions containing both borate and phosphate starting materials were also carried out but none of these systems yielded novel crystalline phases. A summary of the reaction conditions for the five phases reported in this chapter is presented in Table 5.1.

Table 5.1 Summary of reaction conditions for the manganese frameworks presented herein

Reagents	Temp (°C)	Time (h)	Crystal morphology	Product formula	Section
MnF_3 (1 mmol, 0.1119 g) NaF (1 mmol, 0.0420 g) LiF (1 mmol, 0.0259 g) H_2SO_4 (1 mmol, 0.05 mL)	175	72	Pink plates	$LiNa_2MnF_2(SO_4)_2$	5.1
MnF_3 (1 mmol, 0.1119 g) LiF (1 mmol, 0.0259 g) Na_2FPO_3 (1 mmol, 0.1440 g) HPF_6 (0.5 mmol, 0.07 mL)	175	72	Dark pink/red plates	$(H/Li)Na_6Mn_3F_{12}(HPO_4)_2$	5.2
MnF_3 (0.5 mmol, 0.0559 g) $LiOH{\cdot}H_2O$ (1 mmol, 0.0420 g) NaF (2 mmol, 0.0840 g) H_3PO_4 (0.9 mmol, 0.06 mL)	175	72	Pink needles	$Na_2MnF_2(PO_2[O,OH,F]_2)_2$	5.3
$NaBF_4$ (1 mmol, 0.1039 g) MnF_3 (2 mmol, 0.2244 g) H_3BO_3 (1 mmol, 0.0616 g) H_3PO_4 (1 mmol, 0.07 mL)	800	24	Pink prisms	$Na_2Mn_5(PO_4)_4$	5.4
$NaBF_4$ (2 mmol, 0.2078 g) MnF_3 (4 mmol, 0.5598 g) H_3BO_3 (1 mmol, 0.0623 g) H_3PO_4 (5 mmol, 0.34 mL)	800	24	Pink tablets	$Na_2Mn_3(P_2O_7)_2$	5.5

5.1 Structure XI: $LiNa_2MnF_2(SO_4)_2$

The product crystallised as pink plate crystals, a suitable sample of which was selected for an SXRD study carried out at 150 K on a Bruker Nonius Kappa CCD diffractometer operating Mo Kα (λ = 0.71073 Å) radiation. Data collected were refined to a structure containing one-dimensional chains of interconnected MnO_4F_2 octahedra and SO_4 tetrahedra with lithium and sodium cations in the inter-chain space, Figure 5.1. The structure shows a triclinic unit cell in the space group $P\bar{1}$, the crystallographic information for structure **XI** is summarised in Table 5.2.

Table 5.2 Single crystal diffraction structure solution summary for structure **XI**

Empirical Formula	$LiNa_2MnF_2S_2O_8$
Formula Weight ($gmol^{-1}$)	341.0
Temperature (K)	150
Appearance	Pink plate
Crystal size (mm)	0.06 x 0.05 x0.01
Crystal system	Triclinic
Space group	*P*-1
Unit cell dimensions	a = 5.2786(11) b = 5.5500(11) c = 6.8760(14) α = 106.113(30) β = 101.205(30) γ = 104.161(30)
λ/Å	0.701073 (Mo Kα)
Volume ($Å^3$)	180.06(35)
Z	1
Density (gcm^{-3})	3.14
Reflections collected	2599
Unique reflections	1300
R_1 (all)	0.060
wR_2 (all)	0.153
GoF	1.040

Structure **XI** comprises of one crystallographically distinct manganese centre which is six-fold coordinated by four oxygens and two fluorines. Each manganese centre is connected to the next in the chain by two SO_4 tetrahedra through vertex sharing of oxygens forming Mn-O-S-O-Mn linkages. The remaining two oxygens of the SO_4 tetrahedra are terminal and are oriented towards the inter-chain space to form the six-fold coordination environments of the sodium and lithium cations along with the terminal fluorines of the *trans*-MnO_4F_2. There are two crystallographically distinct sodium sites and one crystallographically distinct lithium site. The lithium cation lies directly between the terminal fluorines of two neighbouring chains which results in the *trans*-LiO_4F_2

coordination while Na1 is coordinated by six oxygens and one fluorine and Na2 is coordinated by seven oxygens and one fluorine.

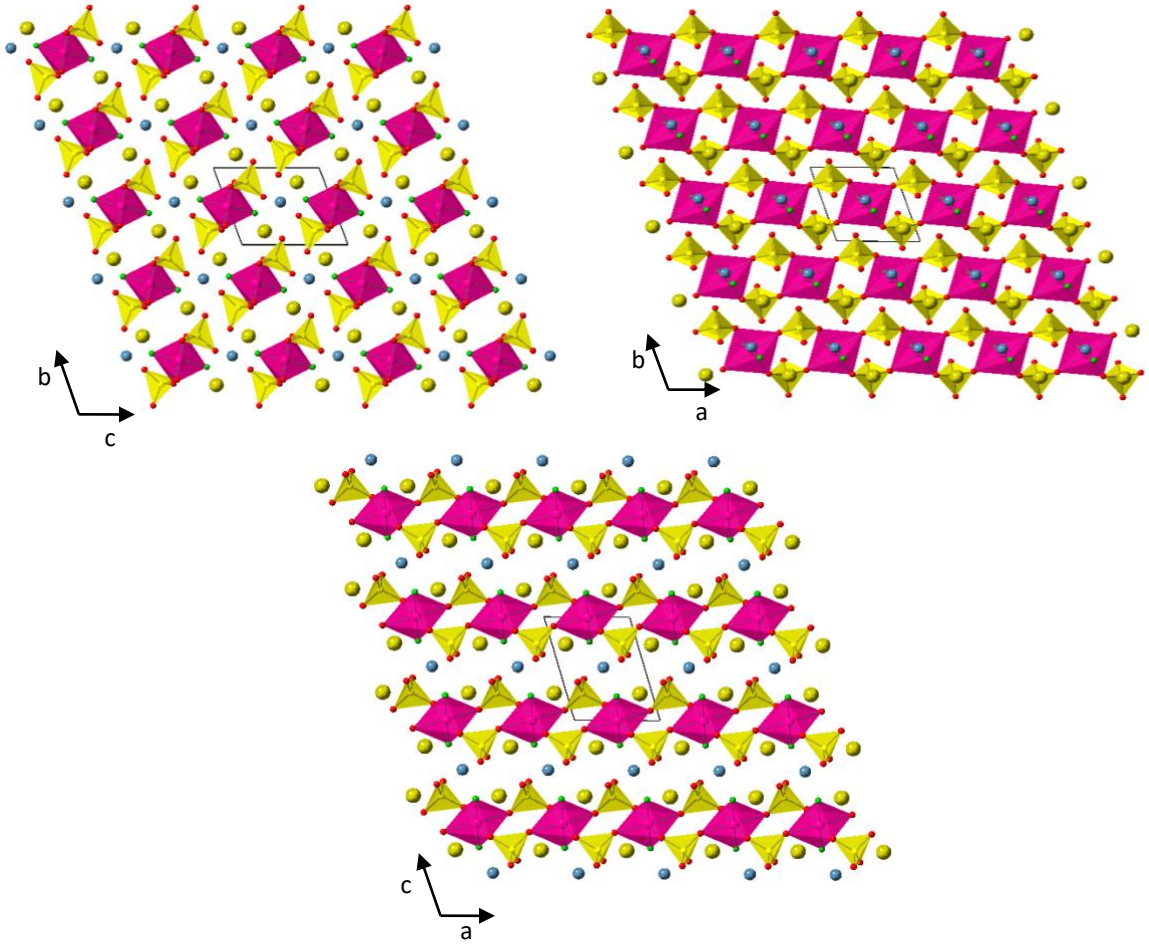

Figure 5.1 Structure **XI** viewed down the a-axis (top left), c-axis (top right) and b-axis (bottom). Mn octahedra are shown in pink, sulfate tetrahedra in yellow and Li, Na, O, F atoms in blue, yellow, red and green respectively. The unit cell is outlined in black.

Bond lengths shown in Table 5.3 are all typical for the atoms involved with marginally shorter distances for M-F bonds in comparison to M-O bonds due to the smaller atomic radius and higher electronegativity of F in comparison with O. The longer Mn-O5/O8 bond lengths of 2.19/2.15 Å respectively are attributed to weak Jahn-Teller distortion caused by the +3 oxidation state of the Mn centre (d_4 – uneven occupation of e_g orbitals).

Table 5.3 Table of bond lengths in structure **XI**

Bond	Bond Length (Å)	Bond	Bond Length (Å)	Bond	Bond Length (Å)
Mn1-F1	1.82(2)	S2-O7	1.44(2)	Na2-O5	2.99(2)
Mn1-F2	1.80(2)	S2-O8	1.48(2)	Na2-O6	2.47(2)
Mn1-O1	1.95(2)	Na1-O1	2.58(2)	Na2-O7	2.35(2)
Mn1-O3	2.02(2)	Na1-O2	2.35(2)	Na2-O8	2.44(2)
Mn1-O5	2.16(2)	Na1-O3	2.88(2)	Na2-F2	2.22(2)
Mn1-O8	2.19(2)	Na1-O4	2.45(3)	Na2-O8	2.43(2)
S1-O1	1.54(2)	Na1-O5	2.55(2)	Li1-F1	1.90(8)
S1-O2	1.47(3)	Na1-O6	2.44(3)	Li1-F2	1.84(8)
S1-O4	1.48(2)	Na1-F1	2.18(2)	Li1-O2	2.13(7)
S1-O6	1.50(2)	Na2-O1	2.83(3)	Li1-O4	2.27(8)
S2-O3	1.49(2)	Na2-O2	2.55(2)	Li1-O6	2.27(7)
S2-O6	1.46(2)	Na2-O3	2.53(2)	Li1-O7	2.14(8)

Bond valence values obtained for all the atoms are shown in Table 5.4 and confirm the +3 oxidation state of the manganese present within the structure. S1 and O4 are also slightly lower in bond valence than expected which might suggest that O4 is partially occupied by fluorine and that manganese would adopt the +2 oxidation state to balance this partial occupation.

Table 5.4 Bond valence values for atoms in structure **XI**

Atom Label	Bond Valence (v.u.)	Atom Label	Bond Valence (v.u)
Mn1	3.05+	O1	2.10-
Li1	1.08+	O2	2.04-
Na1	1.21+	O3	2.09-
Na2	1.23+	O4	1.85-
S1	5.76+	O5	1.97-
S2	6.08+	O6	2.00-
F1	1.11-	O7	2.07-
F2	1.11-	O8	2.08-

5.2 Structure XII: (H/Li)$Na_6Mn_3F_{12}(PO_3F)_2$

The product crystallised as pink plate crystals, a suitable sample of which was selected for an SXRD study carried out at 150 K on a Bruker Nonius Kappa CCD diffractometer operating Mo Kα (λ = 0.71073 Å) radiation. Data collected were refined to a structure containing two-dimensional layers of interconnected MnF_4O_2/MnF_6 octahedra and PO_3F tetrahedra with sodium, lithium and hydrogen cations in the interlayer space, Figure 5.2. The structure shows a triclinic unit cell in the space group $P\bar{1}$, the crystallographic information for structure **XII** is summarised in Table 5.5.

Table 5.5 Single crystal diffraction structure solution summary for structure **XII**

Empirical Formula	$H/LiNa_6Mn_3F_{14}P_2O_6$
Formula Weight ($gmol^{-1}$)	198.8
Temperature (K)	150
Appearance	Pink plate
Crystal size (mm)	0.05 x 0.04 x 0.01
Crystal system	Triclinic
Space group	P-1
Unit cell dimensions	a = 5.6060(11) b = 7.5150(15) c = 10.1730(20) α = 70.531 (30) β = 85.021(30) γ = 79.881(30)
λ/Å	0.701073 (Mo Kα)
Volume ($Å_3$)	397.60(49)
Z	2
Density (gcm^{-3})	1.66
Reflections collected	2850
Unique reflections	1803
R_1 (all)	0.051
wR_2 (all)	0.131
GoF	0.756

The layers within structure **XII** are formed from three crystallographically distinct Mn centres (Figure 5.3); one MnF_6 and two *trans*-MnF_4O_2 octahedra linked directly in the *b*-direction via vertex sharing fluorines and further linked via vertex sharing oxygens of PO_3F tetrahedra. The terminal oxygens and fluorines form the coordination environments for the inter-layer sodium and hydride/lithium cations. There are three crystallographically distinct sodium cations within structure **XII**; Na1 and Na2 are both six-fold coordinated with octahedral and trigonal prismatic environments respectively and Na3 is seven-fold coordinated. The lithium/hydride site is octahedrally coordinated with axial elongation of the Li1/H1-F4 bonds.

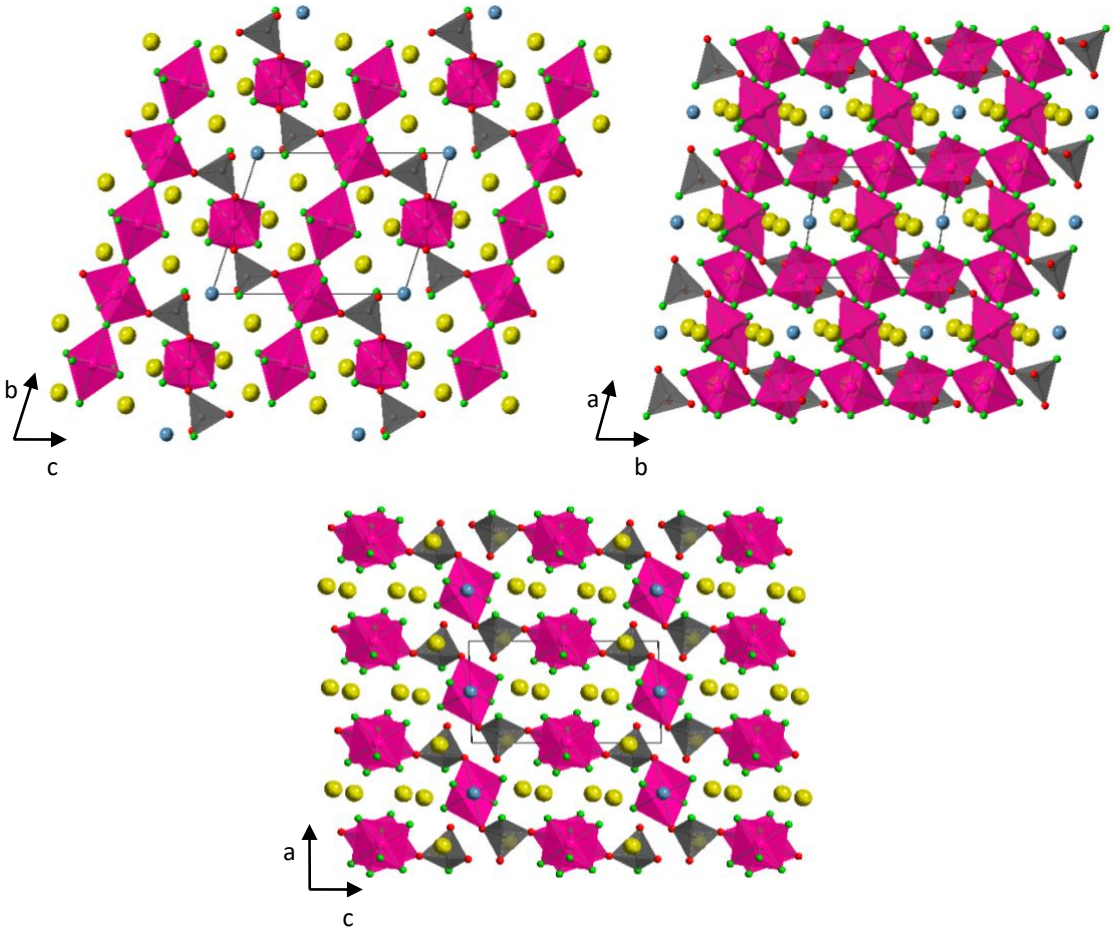

Figure 5.2 Structure **XII** viewed along the a-axis (top left), c-axis (top right) and b-axis (bottom). Mn octahedra are shown in pink, PO_3F tetrahedra in grey and Li, Na, O, F atoms in blue, yellow red and green respectively. The unit cell is outlined in black.

The bond lengths reported in Table 5.6 are all typical for the atoms involved with elongation seen for the axial Mn-O bonds due to Jahn Teller distortion caused by Mn being in the +3 oxidation state.

Table 5.6 Table of selected bond lengths in structure **XII**

Bond	Bond Length (Å)	Bond	Bond Length (Å)	Bond	Bond Length (Å)
Mn1-F2	1.842(3) x2	P1-O1	1.500(4)	Na2-F3	2.442(4)
Mn1-F3	1.855(3) x2	P1-O2	1.498(4)	Na2-F5	2.252(3)
Mn1-F6	2.107(3) x2	P1-O4	1.527(4)	Na2-F6	2.348(4)
Mn2-F1	1.826(3) x2	P1-F7	1.541(4)	Na2-O2	2.448(4)
Mn2-F6	1.939(3) x2	Na1-F1	2.297(3)	Na3-F2	2.342(4)
Mn2-O2	2.098(4) x2	Na1-F2	2.277(3)	Na3-F3	2.419(3)
Mn3-F4	1.853(3) x2	Na1-F3	2.414(4)	Na3-F4	2.252(4)
Mn3-F5	1.846(3) x2	Na1-F4	2.282(3)	Na3-F5	2.307(3)
Mn3-O1	2.191(3) x2	Na1-F7	2.321(5)	Na3-O1	2.647(4)
Li1/H1-O4	2.212(4) x2	Na1-O4	2.323(4)		2.334(4)
Li1/H1-F7	2.054(4) x2	Na2-F1	2.285(3)	Na3-O2	2.880(5)
Li1/H1-F4	2.582(3) x2	Na2-F2	2.418(3)		

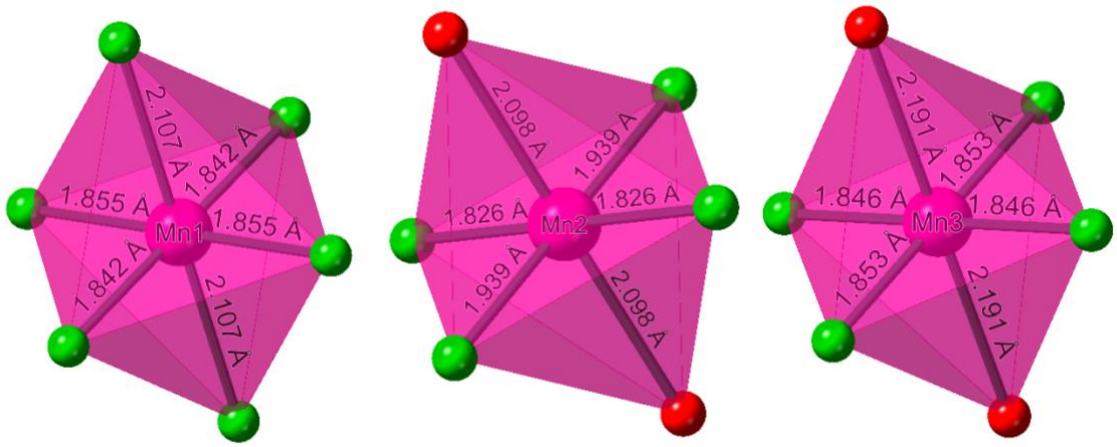

Figure 5.3 Three manganese coordination environments including bond lengths in structure **XII**

The bond valence calculations reported in Table 5.7 confirm that all three Mn centres adopt the +3 oxidation state and support the structure solution. Li1/H1 is slightly low due to bond valence calculations modelled on a fully occupied lithium site rather than the partial substitution of hydride. The terminal oxygen of the PO_3F unit is lower than expected (-0.47 v.u.) which suggests partial substitution by either fluorine atoms or hydroxyl groups.

Table 5.7 Bond valence values for all atoms in structure **XII**

Atom Label	Bond Valence (v.u)	Atom Label	Bond Valence (v.u.)
Mn1	2.96+	O2	1.95-
Mn2	2.97+	O4	1.53-
Mn3	2.97+	F1	1.00-
P1	4.38+	F2	1.05-
Li1/H1	0.64+	F3	0.98-
Na1	0.99+	F4	1.00-
Na2	1.03+	F5	1.00-
Na3	1.07+	F6	1.00-
O1	1.95-	F7	1.13-

5.3 Structure XIII: $Na_2MnF_2(PO_2[O, OH, F]_2)_2$

The product crystallised as pink needles, a suitable sample of which was selected for an SXRD study 150 K on a Bruker Nonius Kappa CCD diffractometer operating Mo Kα (λ = 0.71073 Å) radiation. Data collected were refined to a structure containing one-dimensional chains of interconnected MnO_4F_2 octahedra and $PO_2[O, OH, F]_2$ tetrahedra with sodium cations in the inter-chain space, Figure 5.4. The structure shows a monoclinic unit cell in space group $P2_1/c$, the crystallographic information for structure **XIII** is summarised in Table 5.8.

Table 5.8 Single crystal diffraction structure solution summary for structure **XIII**

Empirical Formula	$Na_2MnF_2(PO_2[O,OH,F]_2)_2$
Formula Weight ($gmol^{-1}$)	172.2
Temperature (K)	150
Appearance	Pink needle
Crystal size (mm)	0.07 x 0.02 x 0.01
Crystal system	Monoclinic
Space group	$P2_1/c$
Unit cell dimensions	a = 4.6874(6) b = 8.1124(7) c = 10.0437(9) β = 89.793(2)
λ/Å	0.701073 (Mo Kα)
Volume ($Å^3$)	381.92 (1)
Z	2
Density (gcm^{-3})	1.50
Reflections collected	1143
Unique reflections	761
R_1 (all)	0.127
wR_2 (all)	0.171
GoF	0.945

As in structure **XI**, there is one crystallographically distinct manganese centre in structure **XIII** which is six-fold coordinated by four oxygens and two fluorines forming *trans*-MnO_4F_2 octahedra. The *trans*-MnO_4F_2 are connected to one another by two $PO_2(O, OH, F)_2$ tetrahedra (one crystallographically distinct phosphorus) infinitely in the *a*-direction. There is one crystallographically distinct sodium cation which is seven-fold coordinated by the terminal oxygens and fluorines of the manganese fluoride fluoro-/hydrogeno-phosphate chains.

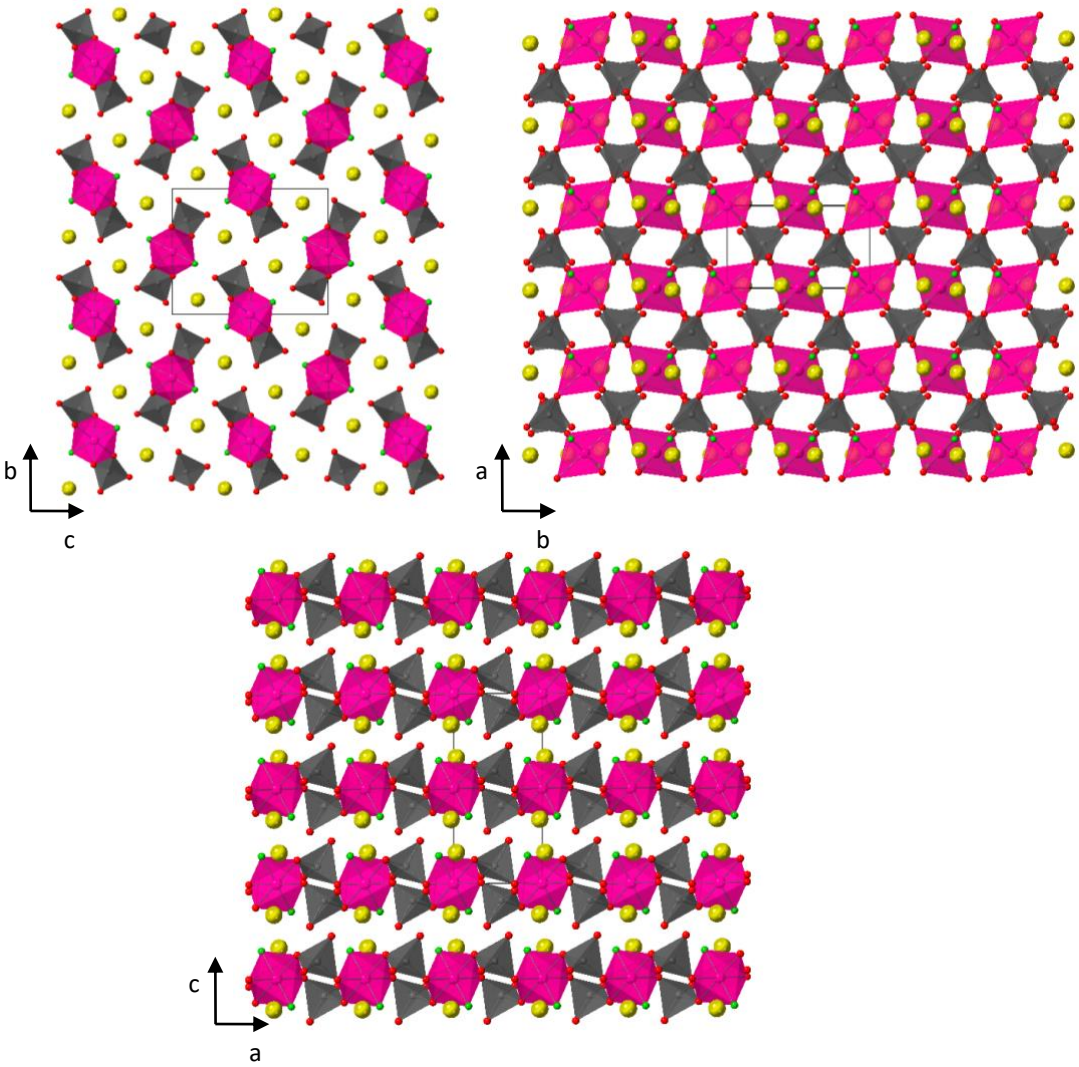

Figure 5.4 Structure **XIII** viewed along the a-axis (top left), c-axis (top right) and b-axis (bottom). Mn octahedra are shown in pink, phosphate tetrahedra in grey and Na, O, F atoms in yellow, red and green respectively. The unit cell is outlined in black.

Bond lengths reported in Table 5.9 are typical for the atoms involved, with axial elongation seen for Mn1-O4 due to Jahn-Teller distortion caused by the uneven d-orbital electronic configuration of +3 oxidation state manganese ions in octahedral environments, as previously reported for other manganese fluorophosphate phases published and structures **XI** and **XII**.[10]

Table 5.9 Table of bond lengths in structure **XIII**

Bond	Bond Length (Å)	Bond	Bond Length (Å)
Mn1-F1	1.842(5) x2	Na1-O1	2.446(7)
Mn1-O2	1.946(5) x2	Na1-O2	2.459(8)
Mn1-O4	2.154(6) x2	Na1-O3	2.477(7)
P1-O1	1.585(6)		2.603(6)
P1-O2	1.527(7)	Na1-O4	2.568(7)
P1-O3	1.551(6)	Na1-F1	2.497(6)
P1-O4	1.486(7)		2.676(6)

Bond valence values calculated for the atoms in structure **XIII** shown in Table 5.10 below, confirm the +3 oxidation state of the manganese centre and show reduced values for the terminal oxygens of the phosphate group, suggesting that these sites are partially occupied by fluorines and hydroxyls.

Table 5.10 Bond valence values for all atoms in structure **XIII**

Atom Label	Bond Valence (v.u.)	Atom Label	Bond Valence (v.u.)
Mn1	3.07+	O1	1.34-
P1	5.02+	O2	1.99-
Na1	1.02+	O3	1.50-
F1	0.86-	O4	1.88-

The formula $Na_2MnF_2(PO_2[O, OH, F]_2)_2$ has previously been reported by the Weller group as a one-dimensional chain-like structure with sodium cations in the interchain space but the orientation of the chains in the reported structure are parallel to one another rather than in the herring-bone configuration seen above.[10] This difference in structure for an identical formula could be due to the disorder of the terminal anions of the phosphate group between O^{2-}, OH^- and F^-. The isostructural $K_2MnF_2(PO_2[O, OH, F]_2)_2$ was reported in the same paper and shows the herringbone chain packing with potassium cations in the interchain space. Both structures reported in the paper show triclinic unit cells whereas structure **XIII** shows a monoclinic unit cell, most likely due to the herringbone orientation and the closer packing of the chains due to the smaller sodium ion in comparison to the potassium ion.[10]

5.4 Structure XIV: $Na_2Mn_5(PO_4)_4$

The product crystallised as pink prisms, a suitable sample of which was selected for an SXRD study carried out at 150 K on an Agilent SuperNova dual source EosS2 diffractometer operating Mo Kα (λ = 0.71073 Å) radiation. Data collected were refined to a structure containing a three-dimensional framework of interconnected MnO_6 polyhedra and PO_4 tetrahedra with sodium cations in the inter-framework space, Figure 5.5. The structure shows a monoclinic unit cell in space group $P2_1/c$, the crystallographic information for structure **XIV** is summarised in Table 5.11.

Table 5.11 Single crystal diffraction structure solution summary for structure **XIV**

Empirical Formula	$Na_2Mn_5(PO_4)_4$
Formula Weight ($gmol^{-1}$)	350.3
Temperature (K)	150
Appearance	Pale pink prism
Crystal size (mm)	0.047 x 0.068 x 0.081
Crystal system	Monoclinic
Space group	$P2_1/c$
Unit cell dimensions	a = 9.3060(4) b = 9.0493(3) c = 8.0218(4) β = 111.628(5)
λ/Å	0.701073 (Mo Kα)
Volume ($Å^3$)	627.98(13)
Z	4
Density (gcm^{-3})	3.70
Reflections collected	2632
Unique reflections	1441
R_1 (all)	0.034
wR_2 (all)	0.067
GoF	1.054

Structure **XIV** comprises of three crystallographically distinct manganese centres; all three are six-fold coordinated by oxygen atoms. Mn1 shows a trigonal pyramidal coordination environment, Mn2 octahedral and Mn3 distorted octahedral as shown in Figure 5.6. There are two distinct phosphorus centres within structure **XIV** which form PO_4 tetrahedra which connect via vertices and edges to the Mn polyhedra. P1 shares one edge with Mn3 and shares through its remaining two vertices to Mn1 and a neighbouring Mn3. P2 edge shares with Mn1 and shares through its remaining two vertices to Mn2 and Mn3. Mn1 also edge shares with neighbouring Mn3, while Mn2 only vertex shares. This is probably the cause of the different orientations of the coordination environment as the increased sharing of oxygens between multiple centres and edges sharing pulls the coordination environments

from the desirable octahedral coordination environment. There is one crystallographically unique sodium environment within structure **XIV** which is seven-fold coordinated.

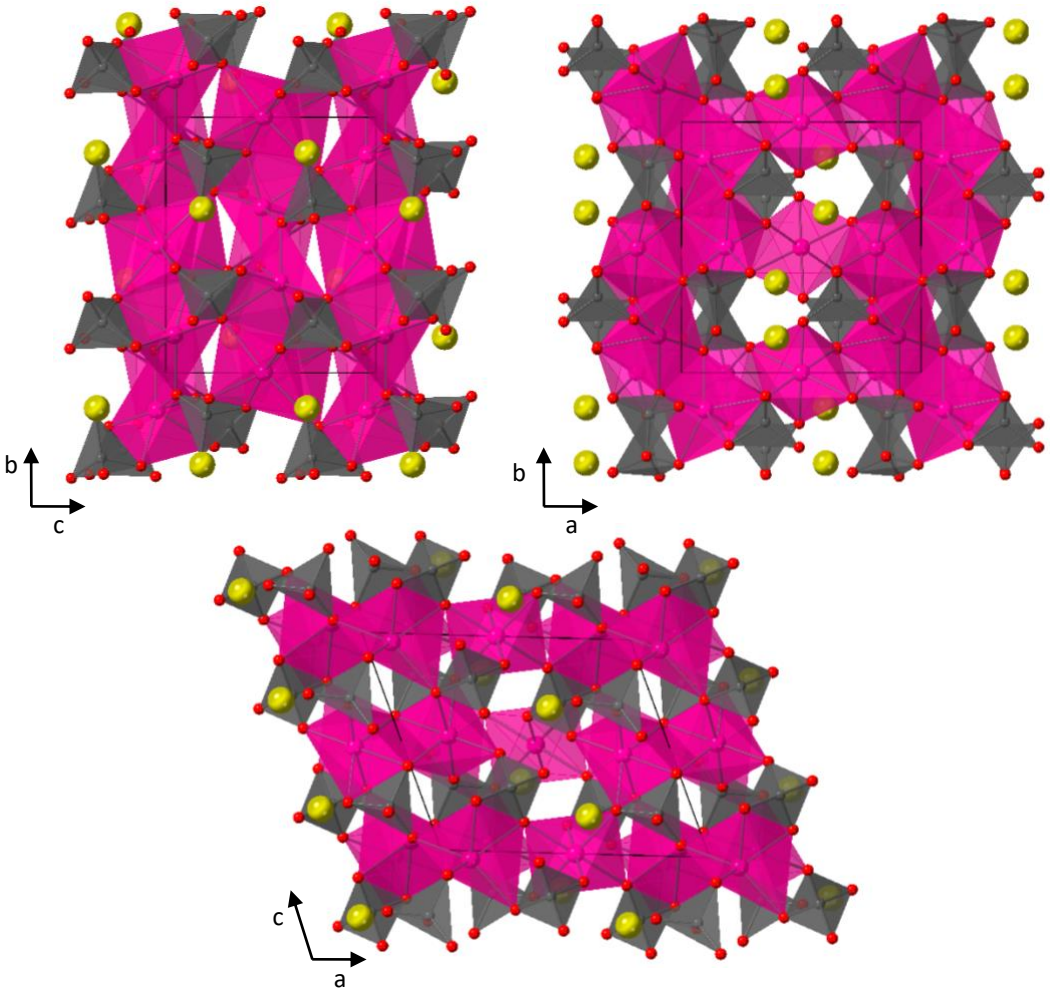

Figure 5.5 Structure **XIV** viewed along the a-axis (top left), c-axis (top right) and b-axis (bottom). Mn polyhedra are shown in pink, PO_4 tetrahedra in grey and Na and O atoms in yellow and red respectively. The unit cell is outlined in black.

The bond lengths within structure **XIV** reported in Table 5.12 below, are all as expected for the elements involved with slight lengthening and shortening seen for distorted polyhedra.

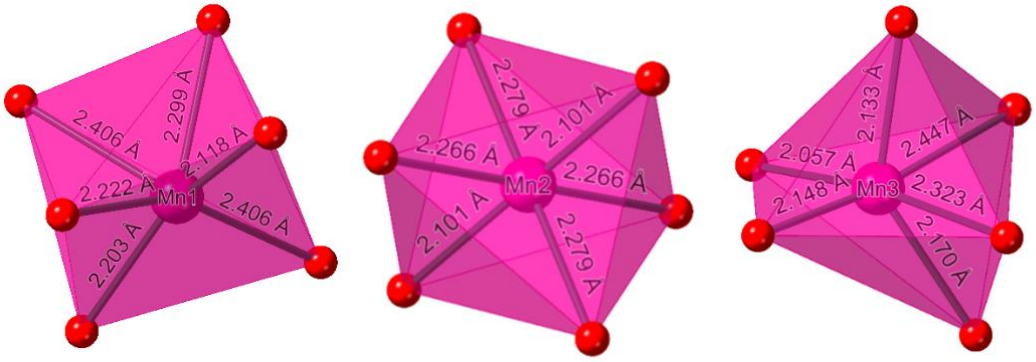

Figure 5.6 Three distinct Mn coordination environments within structure **XIV**

Table 5.12 Table of bond lengths in structure **XIV**

Bond	Bond Length (Å)	Bond	Bond Length (Å)	Bond	Bond Length (Å)
Mn1-O1	2.203(3)	Mn3-O1	2.133(3)	P2-O1	1.563(3)
Mn1-O3	2.118(3)		2.323(3)	P2-O2	1.552(3)
	2.222(3)	Mn3-O2	2.170(3)	P2-O3	1.524(3)
Mn1-O6	2.406(3)	Mn3-O5	2.057(3)	P2-O7	1.529(3)
Mn1-O8	2.299(3)	Mn3-O6	2.447(3)	Na1-O2	2.531(4)
	2.582(4)	Mn3-O7	2.148(3)	Na1-O4	2.246(3)
Mn2-O2	2.266(3) x2	P1-O4	1.532(3)		2.689(4)
Mn2-O4	2.101(3) x2	P1-O5	1.542(3)	Na1-O5	2.387(3) x2
Mn2-O8	2.279(3) x2	P1-O6	1.556(3)	Na1-O7	2.373(3)
		P1-O8	1.544(4)	Na1-O8	2.582(4)

The calculated bond valence values shown in Table 5.13 confirm the +2 oxidation state of the Mn centres and further supports the structure solution from SXRD data.

Table 5.13 Bond valence values for all atoms in structure **XIV**

Atom Label	Bond Valence (v.u.)	Atom Label	Bond Valence (v.u.)
Mn1	1.89+	O2	1.97-
Mn2	1.94+	O3	2.01-
Mn3	1.99+	O4	2.02-
P1	4.88+	O5	2.04-
P2	4.92+	O6	1.85-
Na1	1.25+	O7	1.97-
O1	2.10-	O8	1.92-

5.5 Structure XV: $Na_2Mn_3(P_2O_7)_2$

The product crystallised as pink tablets, a suitable sample of which was chosen for an SXRD study carried out at 150 K on an Agilent Xcalibur EosS2 diffractometer operating Mo Kα (λ = 0.71073 Å) radiation. Data collected were refined to a structure containing layers of interconnected MnO_6 polyhedra and P_2O_7 double tetrahedra units with sodium cations in the interlayer space, Figure 5.7. The structure shows a triclinic unit cell in space group $P\bar{1}$, the crystallographic information for structure **XV** is shown in Table 5.14.

Table 5.14 Single crystal diffraction structure solution summary for structure **XV**

Empirical Formula	$Na_2Mn_3(P_2O_7)_2$
Formula Weight ($gmol^{-1}$)	279.3
Temperature (K)	150
Appearance	Pale pink tablets
Crystal size (mm)	0.039 x 0.081 x 0.121
Crystal system	Triclinic
Space group	*P*-1
Unit cell dimensions	a = 5.3618(3) b = 6.5622(4) c = 16.2740(9) α = 21.233(5) β = 82.744(5) γ = 72.348(5)
λ/Å	0.701073 (Mo Kα)
Volume ($Å^3$)	357.32(10)
Z	4
Density (gcm^{-3})	3.45
Reflections collected	8057
Unique reflections	2559
R_1 (all)	0.038
wR_2 (all)	0.063
GoF	1.093

Structure **XV** contains three crystallographically distinct manganese centres; all three are six-fold coordinated distorted octahedra which are connected via edge sharing to one another to form layers of interconnected manganese polyhedra, Figure 5.8. The layers of manganese polyhedra are interconnected by four crystallographically distinct phosphorus centres in pairs of P_2O_7 thus forming a 'double layered' structure. Between these double layers there are two crystallographically distinct sodium ions which are both seven-fold coordinated by oxygens. The bond lengths shown in Table 5.15 are typical for the atoms involved with slight elongation seen for the bridging P-O bonds in the pyrophosphate groups (P1 and P4 to O12; P2 and P3 to O9).

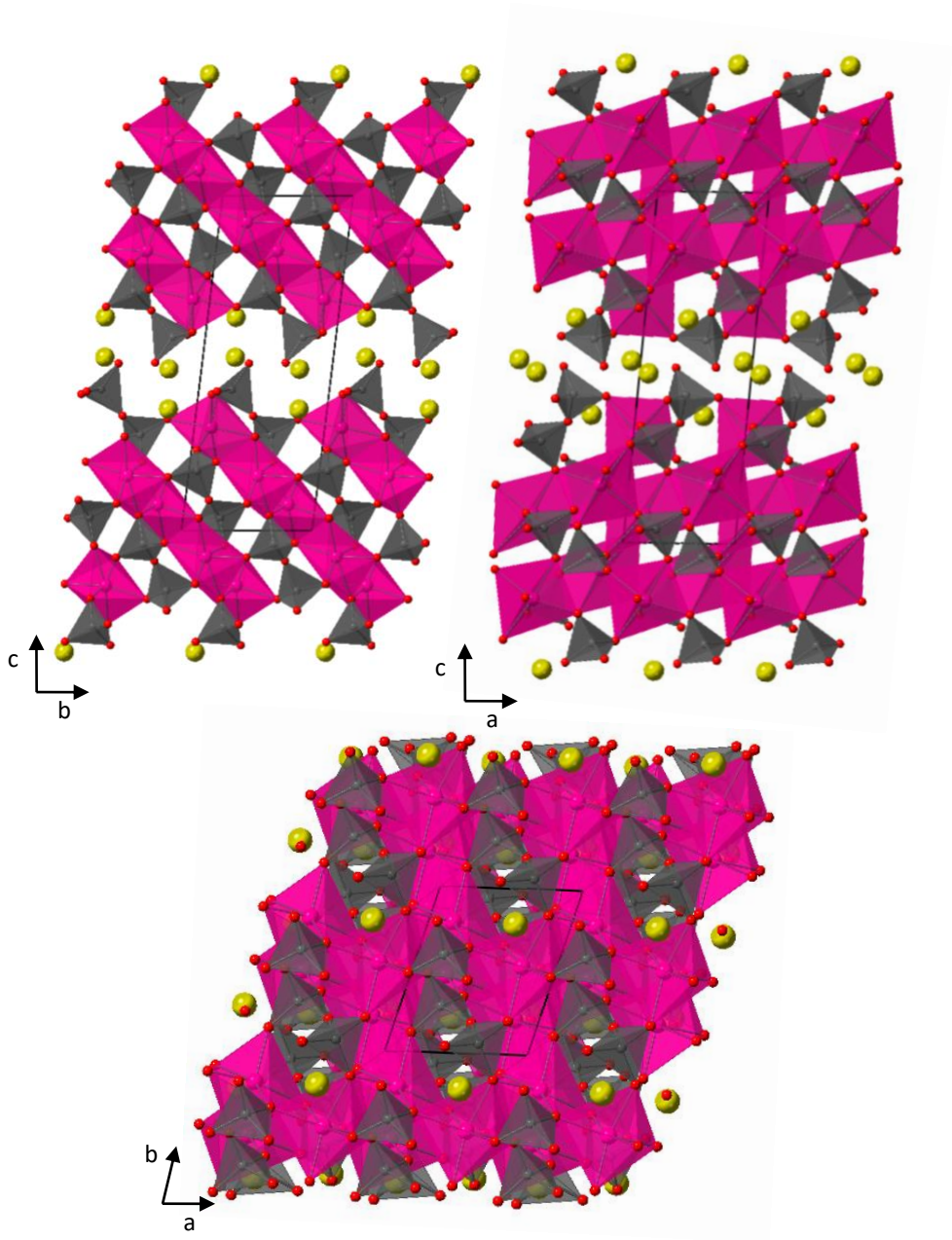

Figure 5.7 Structure **XV** viewed along the a-axis (top left), b-axis (top right) and c-axis (bottom). Mn polyhedra are shown in pink, PO_4 tetrahedra in grey and Na and O atoms in yellow and red respectively. The unit cell is outlined in black.

Table 5.15 Table of bond lengths for structure **XV**

Bond	Bond Length (Å)	Bond	Bond Length (Å)	Bond	Bond Length (Å)
Mn1-O1	2.159(3)	Mn3-O14	2.153(3)	P4-O14	1.519(3)
Mn1-O2	2.116(3)	P1-O5	1.521(3)	Na1-O5	2.431(3)
	2.535(3)	P1-O8	1.531(3)	Na1-O10	2.363(3)
Mn1-O3	2.138(3)	P1-O11	1.514(3)		2.843(3)
Mn1-O7	2.142(3)	P1-O12	1.600(3)	Na1-O13	2.493(3)
Mn1-O11	2.311(3)	P2-O1	1.520(3)		2.450(3)
Mn2-O1	2.194(3)	P2-O2	1.515(3)	Na1-O14	2.515(3)
Mn2-O3	2.177(3)	P2-O7	1.522(3)		2.864(3)
Mn2-O6	2.130(3)	P2-O9	1.597(3)	Na2-O4	2.545(3)
Mn2-O7	2.174(3)	P3-O3	1.524(3)	Na2-O5	2.403(3)
Mn2-O11	2.161(3)	P3-O4	1.493(3)	Na2-O8	2.755(3)
Mn3-O4	2.147(3)	P3-O6	1.530(3)	Na2-O10	2.867(3)
Mn3-O5	2.169(3)	P3-O9	1.590(3)	Na2-O12	2.868(3)
Mn3-O6	2.169(3)	P4-O10	1.517(3)	Na2-O13	2.332(3)
Mn3-O8	2.192(3)	P4-O12	1.630(3)	Na2-O14	2.453(3)
Mn3-O10	2.223(3)	P4-O13	1.512(3)		

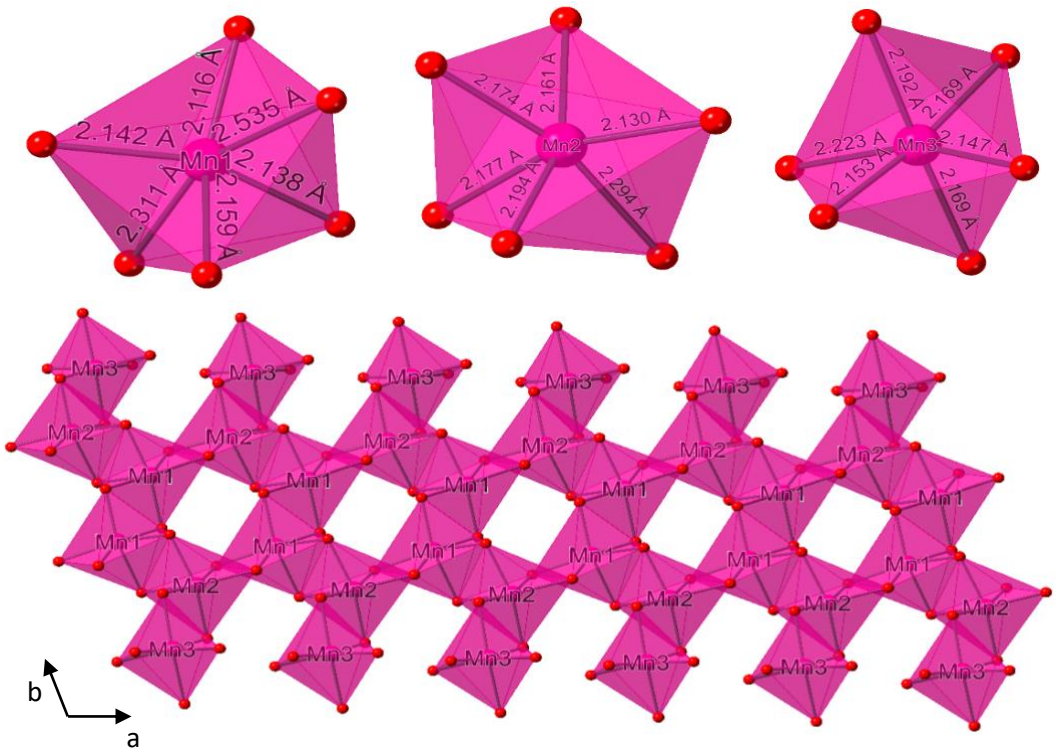

Figure 5.8 Three distinct Mn coordination environments (top) and their connectivity within the layers of structure **XV** (bottom).

Bond valence values were calculated for all atoms within the structure and are shown in Table 5.16, these values confirm the +2 oxidation state of the manganese centres. In addition, the central bridging oxygens of the pyrophosphate groups have a higher than expected bond valence (+0.25/0.29).

Table 5.16 Bond valence values for structure **XV**

Atom Label	Bond Valence (v.u.)	Atom Label	Bond Valence (v.u)
Mn1	2.00+	O4	1.92-
Mn2	2.07+	O5	2.02-
Mn3	2.07+	O6	1.99-
P1	4.96+	O7	2.01-
P2	5.01+	O8	1.94-
P3	5.02+	O9	2.29-
P4	4.90+	O10	1.94-
Na1	1.06+	O11	1.95-
Na2	1.04+	O12	2.24-
O1	2.01-	O13	1.89-
O2	1.88-	O14	2.02-
O3	2.04-		

5.6 Conclusion

Five new manganese-based framework structures have been successfully synthesised utilising a mixture of 'hydrofluorothermal' synthesis and classic ceramic synthetic methods. All structures were solved from SXRD data collected and the structural solution checked/rationalised with bond valence calculations. In structures **XI** – **XIII**, the manganese adopts the common +3 oxidation state with ocatahedral coordination environments which show Jahn-Teller distortion. However, in structures **XIV** and **XV** the manganese adopts the +2 oxidation state and exhibits irregular/distorted coordination environments.

The structural motifs reported herein vary in dimensionality from one-dimensional chains (structures **XI** and **XIII**) through two-dimensional layers (structures **XII** and **XV**) to a three-dimensional framework (structure **XIV**). As seen previously with the titanium fluoride sulfate systems (chapters 3 and 4), the manganese fluoride sulfate phase reported in this chapter also shows a low framework dimensionality in comparison with the manganese fluoride phosphates/fluorophosphates. Two-dimensional layered transition metal fluoride sulfates have been synthesised within the Weller group and indeed the three-dimensional Li_2FeSO_4F has been investigated as a potential battery cathode material but numbers of reported transition metal fluorosulfate frameworks of higher dimensionality are very low.[11]

Successful incorporation of both lithium and sodium cations into structure **XI** is the first known example of a mixed Li/Na manganese fluoride sulfate structure. Though a mixed Li/Na iron fluoride phosphate system has been reported previously, structure **XII** appears to be the first example of a mixed Li/Na manganese fluorophosphate. [2,12]

Structures **XIV** and **XV** are a sodium manganese phosphate and pyrophosphate produced from classical high temperature ceramic synthetic methods. Though fluoride and borate were included in the reaction mixture the crystalline phases produced contained neither of these moieties. However, these structures may still be of interest due to low oxidation state of the manganese raising the possible functionality as a Mn^{2+}/Mn^{4+} double redox active sodium-ion cathode material which would theoretically have very high capacity for ion transport.

5.7 References

(1) Kim, S. W.; Seo, D. H.; Kim, H.; Park, K. Y.; Kang, K. A Comparative Study on Na_2MnPO_4F and Li_2MnPO_4F for Rechargeable Battery Cathodes. *Phys Chem Chem Phys* **2012**, *14* (10), 3299–3303.

(2) Ben Yahia, H.; Shikano, M.; Sakaebe, H.; Koike, S.; Tabuchi, M.; Kobayashi, H.; Kawaji, H.; Avdeev, M.; Miiller, W.; Ling, C. D. Synthesis and Characterization of the Crystal Structure, the Magnetic and the Electrochemical Properties of the New Fluorophosphate $LiNaFe[PO_4]F$. *Dalt. Trans.* **2012**, *41* (38), 11692–11699.

(3) Menezes, P. W.; Hoffmann, S.; Prots, Y.; Schnelle, W.; Kniep, R. Synthesis and Crystal Structure of $SrFe[BP_2O_8(OH)_2]$. *Zeitschrift fur Anorg. und Allg. Chemie* **2009**, *635* (8), 1153–1156.

(4) Zhou, Y.; Hoffmann, S.; Menezes, P. W.; Carrillo-Cabrera, W.; Huang, Y.-X.; Vasylechko, L.; Schmidt, M.; Prots, Y.; Deng, J.-F.; Mi, J.-X.; Kniep, R. Nanoporous Titanium Borophosphates with Rigid Gainesite-Type Framework Structurew. *Chem. Commun. Chem. Commun* **2011**, *47*, 11695–11696.

(5) Li, M.; Xie, D.; Chang, J.; Shi, H. Template Synthesis, Structure and Magnetic Property of a New Open-Framework Manganese Borophosphate: $(C_4N_2H_{12})Mn[B_2P_3O_{12}(OH)]$. *Inorganica Chim. Acta* **2007**, *360* (2), 710–714.

(6) Huang, Y. X.; Schnelle, W.; Zhang, H.; Borrmann, H.; Kniep, R. Hydrothermal Synthesis, Crystal Structure, and Magnetic Properties of a Novel Organo-Templated Iron(III) Borophosphate: $(C_3H_{12}N_2)FeIII_6(H_2O)_4[B_4P_8O_{32}(OH)_8]$. *J. Solid State Chem.* **2009**, *182* (4), 920–924.

(7) Bontchev, R. P.; Jacobson, A. J. Synthesis and Characterization of the Open-Framework Cobalt Borophosphate: $(C_4N_2H_{12})Co[B_2P_3O_{12}(OH)]$. *Mater. Res. Bull.* **2002**, *37* (12), 1997–2005.

(8) Ewald, B.; Huang, Y. X.; Kniep, R. Structural Chemistry of Borophosphates, Metalloborophosphates, and Related Compounds. *Zeitschrift fur Anorg. und Allg. Chemie* **2007**, *633* (10), 1517–1540.

(9) Yaghoobnejad Asl, H.; Stanley, P.; Ghosh, K.; Choudhury, A. Iron Borophosphate as a Potential Cathode for Lithium- and Sodium-Ion Batteries. *Chem. Mater.* **2015**, *27* (20), 7058–7069.

(10) Armstrong, J. A.; Williams, E. R.; Weller, M. T. Manganese (III) Fluorophosphate Frameworks. *Dalt. Trans.* **2013**, *42*, 2302–2308.

(11) Wang, Q.; Madsen, A.; Owen, J. R.; Weller, M. T. Direct Hydrofluorothermal Synthesis of Sodium Transition Metal Fluorosulfates as Possible Na-Ion Battery Cathode Materials. *Chem. Commun.* **2013**, *49* (49), 2121–2123.

(12) Ellis, B. L.; Makahnouk, W. R. M.; Makimura, Y.; Toghill, K.; Nazar, L. F. A Multifunctional 3.5V Iron-Based Phosphate Cathode for Rechargeable Batteries. *Nat. Mater.* **2007**, *6* (10), 749–753.

Chapter 6 : Vanadium, Chromium and Lanthanide Sulfate Frameworks

6.0 Introduction

Once all the titanium and manganese framework investigations were thoroughly exhausted, the author's research changed to investigate other first row transition metal centres (vanadium and chromium) and then the lanthanides and yttrium (5th period TM). Vanadium frameworks had previously been synthesised within the group and across the research field, with $Na_3V_2(PO_4)_2F_3$ being studied by Barker *et al.* in 2006 as a potential cathode material in a lithium-ion battery.[1–4]

While several chromium phosphates have previously been published, relatively few chromium sulfate phases appear in the literature. [5–7] Unlike the chromium phosphates, the few chromium sulfates which have been reported are mostly hydrated phases with no recorded fluoride incorporation. [8,9]

The lanthanides and yttrium are of interest in the search for novel fluoride sulfate frameworks due to the increased ionic radius giving rise to greater variation in the possible frameworks formed. Various yttrium sulfates have been reported and investigated with interest in superconductivity observed in some yttrium copper oxides with sulfate anions. [10] Lanthanides have been heavily researched in terms of metal organic frameworks (MOFs) where lanthanide phosphates have played a key role. [11–13]

The sodium/vanadium/fluoride/sulfate system was given to another project student under the supervision of the author. The synthesis of structure **XV** reported herein was therefore carried out by Hannah S.I. Sullivan with single crystal diffraction data collection and structure solution being carried out as a dual effort/training exercise. The remaining three structures were the sole efforts of the author. Structures **XV** and **XVI** were included in the paper 'Synthesis and structural characterisation of transition metal fluoride sulfates' submitted by the author and published in Dalton Transactions. [14]

As with much of this research, the structures reported herein were produced under hydrofluorothermal reaction conditions utilising TM/Ln fluorides and HF, as summarised in Table 6.1.

Table 6.1 Summary of reaction conditions and crystal morphologies of the structures presented herein.

Reagents	Temp (°C)	Time (h)	Crystal morphology	Product formula	Section
NaOH , (12 mmol , 0.64 mL) VF_3, (4 mmol, 0.4317 g) H_2SO_4, (8 mmol, 0.45 mL)	175	48	Forest green plate	$Na_2VF_3SO_4$	6.1
CrF_3, (1 mmol, 0.10919 g) H_2SO_4, (4 mmol, 0.22 mL) NaF,, (2 mmol, 0.08379 g) HF (0.6 mmol, 2 drops)	180	96	Green prisms	$Na_3CrF_3(SO_4)_2$	6.2
NaF, (0.5 mmol, 0.0209 g) DyF_3, (4.5 mmol, 0.0982 g) H_2SO_4, (2 mmol, 0.112 mL)	200	48	Colourless to pale grey prisms	$NaLn(SO_4)_2F$ (Ln = Y, Nd, Eu, Gd, Tb, Dy, Ho, Er)	6.3
NaF (0.5 mmol, 0.0210 g) YF_3, (0.5 mmol, 0.0732 g) H_2SO_4, (2 mmol, 0.112 mL)	200	48	Colourless to grey prisms	$NaY(SO_4)_2$	6.4

6.1 Structure XVI: $Na_2VF_3SO_4$

The product crystallised as forest green plates, a suitable sample of which was selected for an SXRD study carried out at 150 K on an Agilent Xcalibur EosS2 diffractometer operating Mo Kα (λ = 0.71073 Å) radiation. Data collected were refined to a structure containing two-dimensional layers of inter-connected VF_4O_2 octahedra and SO_4 tetrahedra with sodium cations in the interlayer space, Figure 6.1. The structure shows a triclinic unit cell in the space group $P\bar{1}$, the crystallographic information for structure **XVI** is summarised in Table 6.2.

Table 6.2 Single crystal diffraction structure solution summary for structure **XVI**.

Empirical Formula	$Na_2VF_3SO_4$
Formula Weight ($gmol^{-1}$)	350.0
Temperature (K)	150
Appearance	Forest green plates
Crystal size (mm)	0.05 ×0.05 × 0.01
Crystal system	Triclinic
Space group	P-1
Unit cell dimensions	a = 6.3555(5) b = 6.4255(8) c = 7.3724(7) α = 65.119(11) β = 89.696(7) γ = 7.3724(7)
λ/Å	0.701073 (Mo Kα)
Volume ($Å^3$)	272.66(15)
Z	2
Density (gcm^{-3})	3.04
Reflections collected	3469
Unique reflections	1257
R_1 (all)	0.032
wR_2 (all)	0.063
GoF	1.112

The layers within structure **XVI** are comprised of two crystallographically distinct vanadium centres which are both coordinated by four fluorines and two oxygens. These two vanadium centres form vertex sharing chains through μ_2-bridging fluorines, each chain is then further connected to the next chain via the sulfate tetrahedra vertex sharing with two vanadium centres of each chain. Both terminal fluorines of the *trans*-VF_4O_2 and two terminal oxygens of each SO_4 are oriented to the inter-layer space and form the coordination environment for the two crystallographically distinct sodium ions. The layers are stacked directly above one another in the *a*-direction with an interlayer distance of 2.926-3.155 Å.

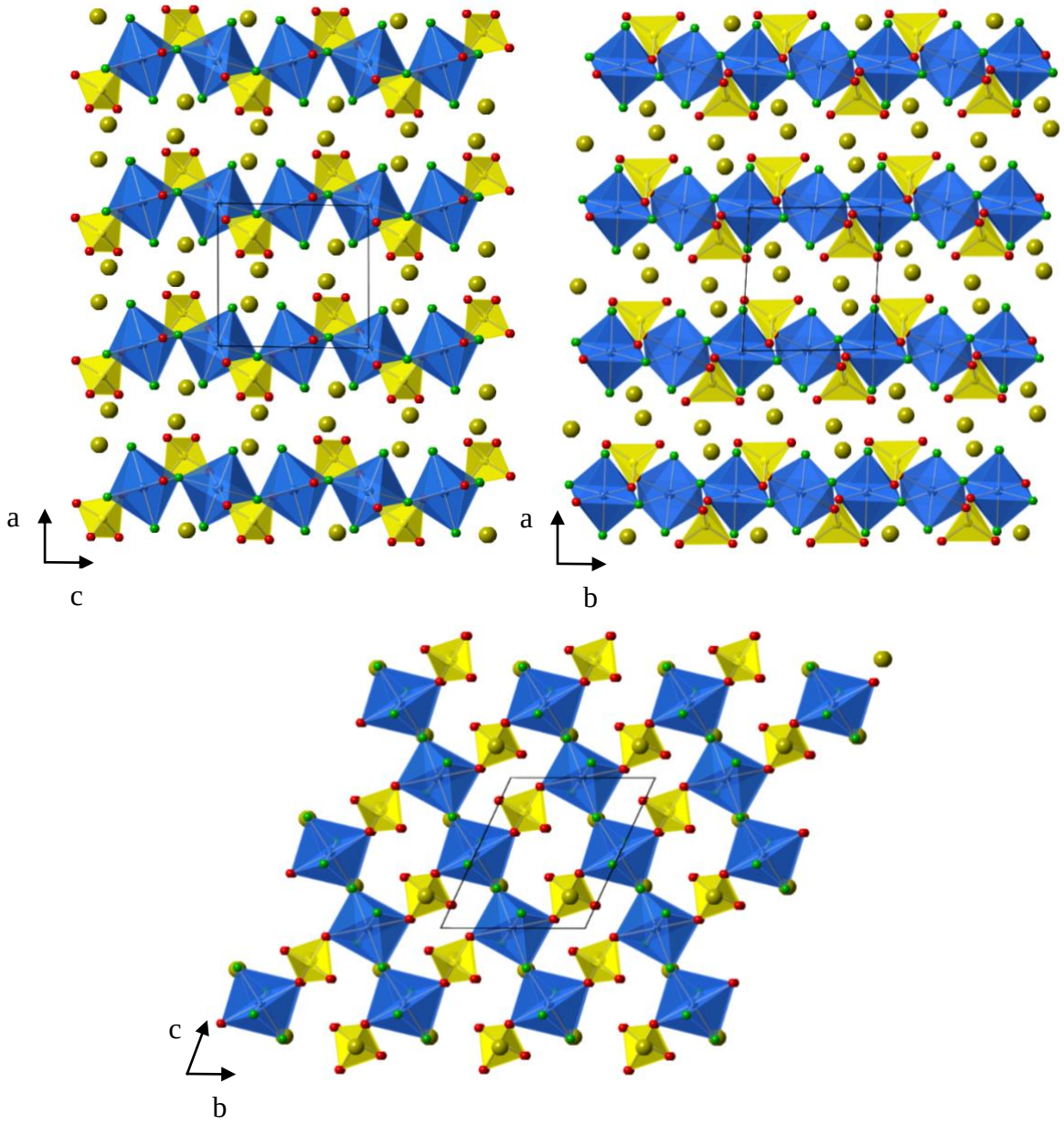

Figure 6.1 Structure **XVI** viewed along the b-axis (top left), c-axis (top right) and a-axis (bottom). V octahedra are shown in navy blue, SO_4 tetrahedra in yellow and O, F and Na atoms shown in red, green and yellow respectively. The unit cell is outlined in black.

Bond valence values for structure **XVI** are reported in Table 6.3 and are all typical for the atoms within the structure and confirm the calculated +3 oxidation state for the vanadium centres. Bond lengths are also reported in

Table 6.4 and show the expected shortening of M-F bonds in comparison to M-O bonds. Very high sample purity is evidenced by the PXRD pattern comparison as simulated from the solved SXRD data (Figure 6.1)

Structure **XVI** has the potential to be of interest as a functional material in rechargeable Na-ion batteries as it has a favourable layered structure with the potential for two Na^+ cations to be removed resulting in the chemical formula: $V(V)F_3SO_4$.

Table 6.3 Bond valence values for all atoms in structure **XVI**.

Atom Label	Bond Valence (v.u.)	Atom Label	Bond Valence (v.u.)
O1	2.05-	F3	0.99-
O2	2.08-	Na1	1.07+
O3	1.95-	Na2	1.09+
O4	2.04-	S1	5.98+
O5	2.04-	V1	3.04+
F1	1.16-	V2	3.12+
F2	0.95-		

Table 6.4 Bond length between atoms in structure **XVI**.

Bond	Bond Length (Å)	Bond	Bond Length (Å)
V1-F1	1.955(2) x2	S1-O5	1.500(2) x2
V1-F2	1.896(2) x2	Na1-F2	2.265(2) x2
V1-O5	2.008(2) x2	Na1-F3	2.360(2) x2
V2-F1	1.906(2) x2	Na1-O3	2.421(2) x2
V2-F3	1.897(2) x2	Na2-O1	2.573(2) x2
V2-O2	2.023(2) x2	Na2-O5	2.827(2)
S1-O2	1.492(2)		2.929(2)
S1-O3	1.449(2)	Na2-F3	2.357(2) x2

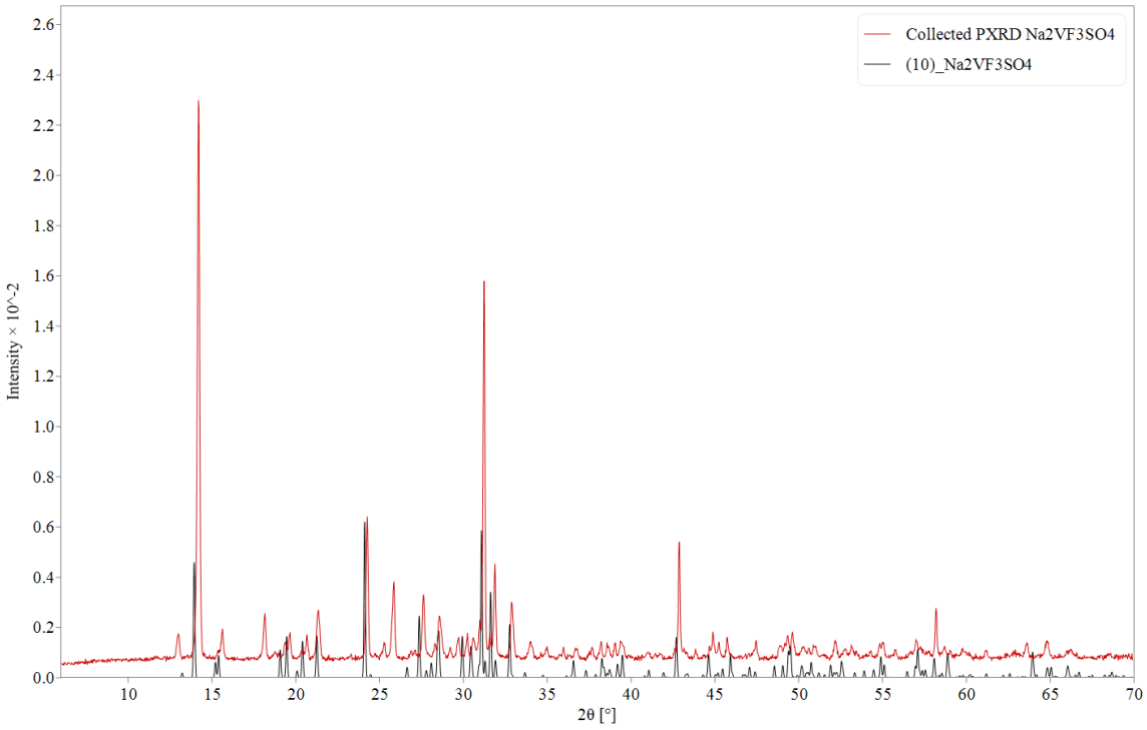

Figure 6.2 Comparison of collected PXRD pattern (red) with simulated PXRD pattern from SXRD data (black) for structure **XVI.**

6.2 Structure XVII: $Na_3CrF_2(SO_4)_2$

The product crystallised as green prisms which grew in an amorphous green solid, a suitable sample of which was selected for an SXRD study carried out on at 150 K on an Agilent SuperNova dual source EosS2 diffractometer operating Cu Kα (λ = 1.54184 Å) radiation. Data collected were refined to a structure containing two-dimensional layers of interconnected CrO_4F_2 octahedra and SO_4 tetrahedra with sodium cations in the interlayer space, Figure 6.3. The structure shows an orthorhombic unit cell in space group *Pbcn*, the crystallographic information for structure **XVII** is summarised in Table 6.5.

Table 6.5 Single crystal diffraction structure solution summary for structure **XVII**.

Empirical Formula	$Na_3CrF_2S_2O_8$
Formula Weight ($gmol^{-1}$)	234.1
Temperature (K)	150
Appearance	Green plate
Crystal size (mm)	0.04 x 0.03 x0.02
Crystal system	Orthorhombic
Space group	Pbcn
Unit cell dimensions	a = 8.7463(5) b = 13.8814(7) c = 6.6009(3)
λ/Å	1.54184 (Cu Kα)
Volume ($Å^3$)	801.42(1)
Z	4
Density (gcm^{-3})	2.91
Reflections collected	1639
Unique reflections	791
R_1 (all)	0.049
wR_2 (all)	0.128
GoF	1.046

This structure is isostructural with the previously reported $Na_3MF_2(SO_4)_2$ (M = V, Mn and Fe), with layers comprised of *cis*-CrO_4F_2 which vertex share through all four oxygen atoms with four SO_4 tetrahedra.[1] Each SO_4 tetrahedra bridges two CrO_4F_2 octahedra with two μ_2-bridging oxygen atoms, the remaining two oxygen atoms are terminal and are oriented towards the inter-layer space. The two *cis*- coordinated fluorine atoms of the CrO_4F_2 octahedra are also terminal and oriented towards the inter-layer space such that each polyhedron's four nearest neighbour fluorine atoms are on the opposite sides of the layer. The layers are stacked in the *b*-direction with an alternating offset such that when viewed along the *c*-axis (top right of Figure 6.3) the terminal fluorine atoms of neighbouring layers are aligned in the *b*-direction but when viewed along the *a*-axis (top left of Figure 6.3) the

two fluorine atoms of one octahedron in one layer are oriented towards fluorine atoms of two different octahedra of the neighbouring layer. There are two crystallographically distinct sodium cations within the inter-layer space each showing different coordination environments: trigonal prismatic NaO_2F_4, and irregular seven-fold NaO_6F.

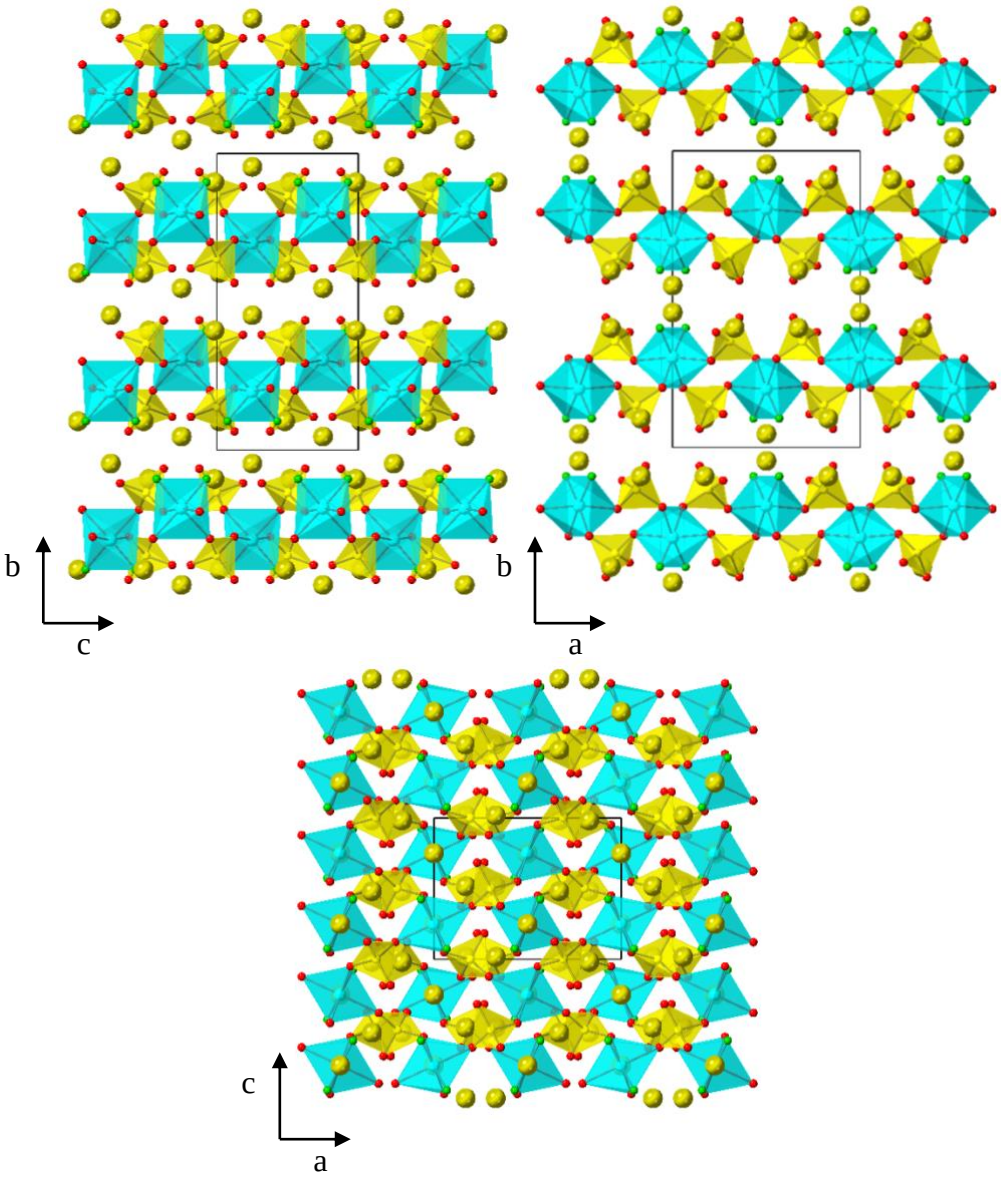

Figure 6.3 Structure **XVII** viewed along the a-axis (top left), c-axis (top right) and b-axis (bottom). Cr octahedra are shown in cyan/turquoise, SO_4 tetrahedra in yellow and O, F and Na atoms in red, green and yellow respectively. The unit cell is outlined in black.

Bond valence values calculated for the atoms in structure **XVII** are summarised in All the other bond valence values are close to the expected oxidation states.

Table 6.6 and confirm the calculated +3 oxidation state for the chromium centres. All the other bond valence values are close to the expected oxidation states.

Table 6.6 Bond valence values for atoms in structure **XVII**.

Atom Label	Bond Valence (v.u.)	Atom Label	Bond Valence (v.u.)
Cr1	2.93+	O1	2.08-
S1	6.03+	O2	2.05-
Na1	1.16+	O3	2.06-
Na2	1.11+	O4	2.01-
F1	0.99-		

Bond lengths between selected atoms are shown in Table 6.7 and show regular octahedral geometry of the CrO_4F_2 octahedra which matches the Fe and V analogues previously reported and contrasts the Mn analogue which showed Jahn-teller distortion as with many of the Mn structures reported in Chapter 5.[1]

Table 6.7 Bond lengths between atoms within structure **XVII**.

Bond	Bond Length (Å)	Bond	Bond Length (Å)
Cr1-O1	2.003(3) x 2	Na1-F1	2.338(2) x 2
Cr1-O2	1.990(3) x 2		2.377(3) x 2
Cr1- F1	1.891(2) x 2	Na2-O1	2.474(3)
S1-O1	1.493(3)	Na2-O2	2.880(4)
S1-O2	1.493(3)	Na2-O3	2.383(3)
S1-O3	1.445(3)	Na2-O4	2.421(3)
S1-O4	1.450(3)		2.871(4)
Na1-O3	2.264(3) x 2	Na2-F1	2.322(3)

Structure **XVII** has a potential interest as a functional material within rechargeable Na-ion batteries as it also has the favourable layered structure with an even greater capacity to remove three Na^+ cations resulting in the well-known Cr(IV) in $CrF_2(SO_4)_2$. To investigate the electrochemical potential of this structure, phase-pure samples must be achieved as the initial phase purity is very low as shown in the collected PXRD pattern in Figure 6.4.

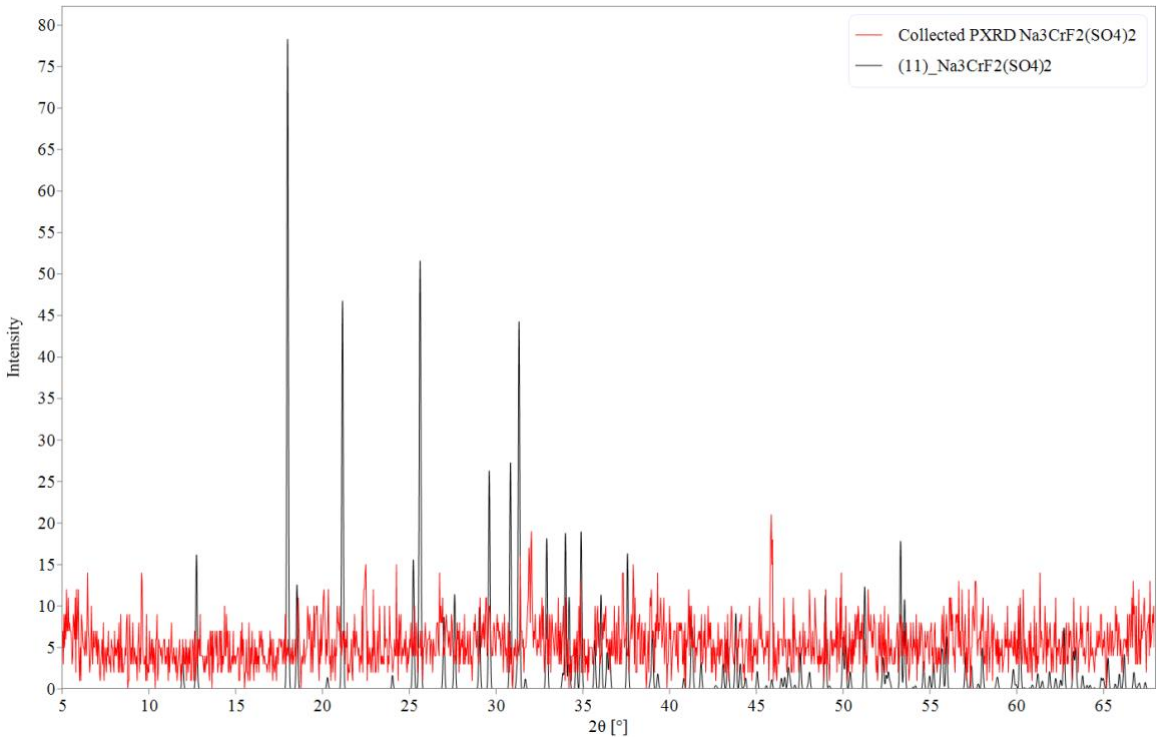

Figure 6.4 Comparison of collected PXRD pattern (red) with simulated PXRD pattern from SXRD data (black) for structure **XVI**.

6.3 Structure XVIII: $NaLn(SO_4)_2F$ (Ln=Nd, Eu, Gd, Tb, Dy, Ho, Er)

The product crystallised as colourless prisms, a suitable sample of which was selected for an SXRD study carried out at 150 K on an Agilent Xcalibur EosS2 diffractometer operating Mo Kα (λ = 0.71073 Å) radiation. Data collected were refined to a structure containing a three-dimensional framework of interconnected DyO_8F polyhedra and SO_4 tetrahedra with sodium cations contained in alternating channels, Figure 6.5. The structure shows a trigonal unit cell in the space group $P3_121$, the crystallographic information for structure **XVII** is summarised in Table 6.8. Upon solution of the Dysprosium containing structure, reactions were carried out with the other lanthanides, and isostructural phases were confirmed in varying purities for Neodymium, Europium, Gadolinium, Terbium, Holmium and Erbium. These phases were confirmed by powder X-ray diffraction.

Table 6.8 Single crystal diffraction structure solution summary for structure **XVIII**.

Empirical Formula	$NaDyS_2O_8F$
Formula Weight ($gmol^{-1}$)	297.5
Temperature (K)	150
Appearance	Colourless prism
Crystal size (mm)	0.16 × 0.04 × 0.03
Crystal system	Trigonal
Space group	$P3_121$
Unit cell dimensions	a = 6.8228(1) b = 6.8228(1) c = 12.6851(3)
λ/Å	0.71073 (Mo Kα)
Volume ($Å^3$)	511.39(0)
Z	4
Density (gcm^{-3})	3.86
Reflections collected	12647
Unique reflections	995
R_1 (all)	0.020
wR_2 (all)	0.047
GoF	1.075

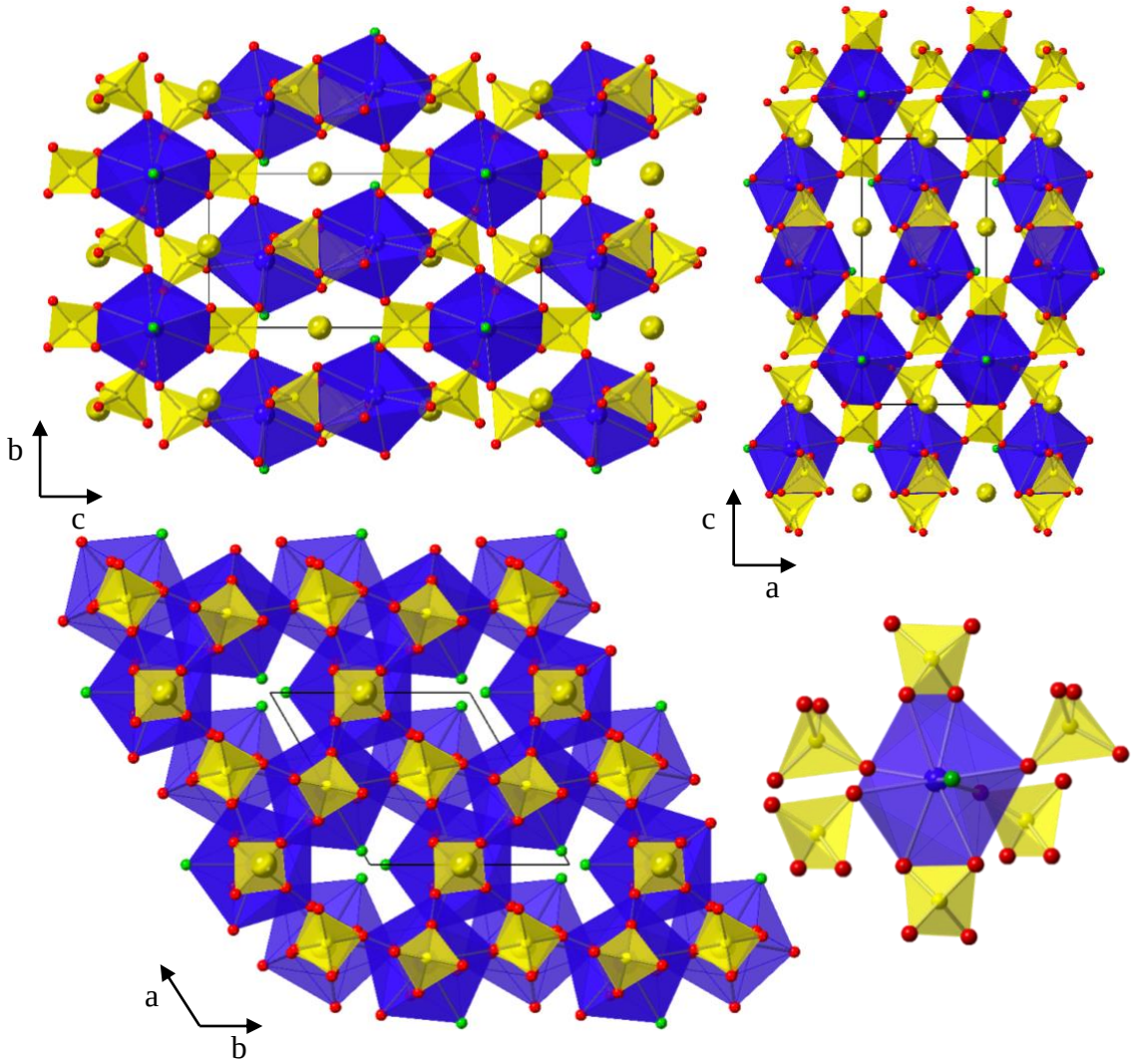

Figure 6.5 Structure **XVII** viewed along the a-axis (top left), b-axis (top right) and c-axis (bottom left) with the connectivity around the Dy centre shown bottom right. Dy nonahedra are shown in royal blue, SO_4 tetrahedra shown in yellow and O,F and Na atoms shown in red, green and yellow respectively. The unit cell is outlined in black.

The three-dimensional framework comprises of one crystallographically distinct DyO_8F polyhedron which is coordinated by two edge sharing SO_4 tetrahedra, four vertex sharing SO_4 tetrahedra and one terminal fluorine atom. The sodium atoms are positioned in channels which run parallel to the *a*- and *b*- axes and the terminal fluorine atoms line very narrow channels which run parallel to the *c*-axis. The comparative PXRD patterns presented in Figure 6.6 show strong agreement between the solved crystal structure and the collected PXRD pattern along with high phase purity.

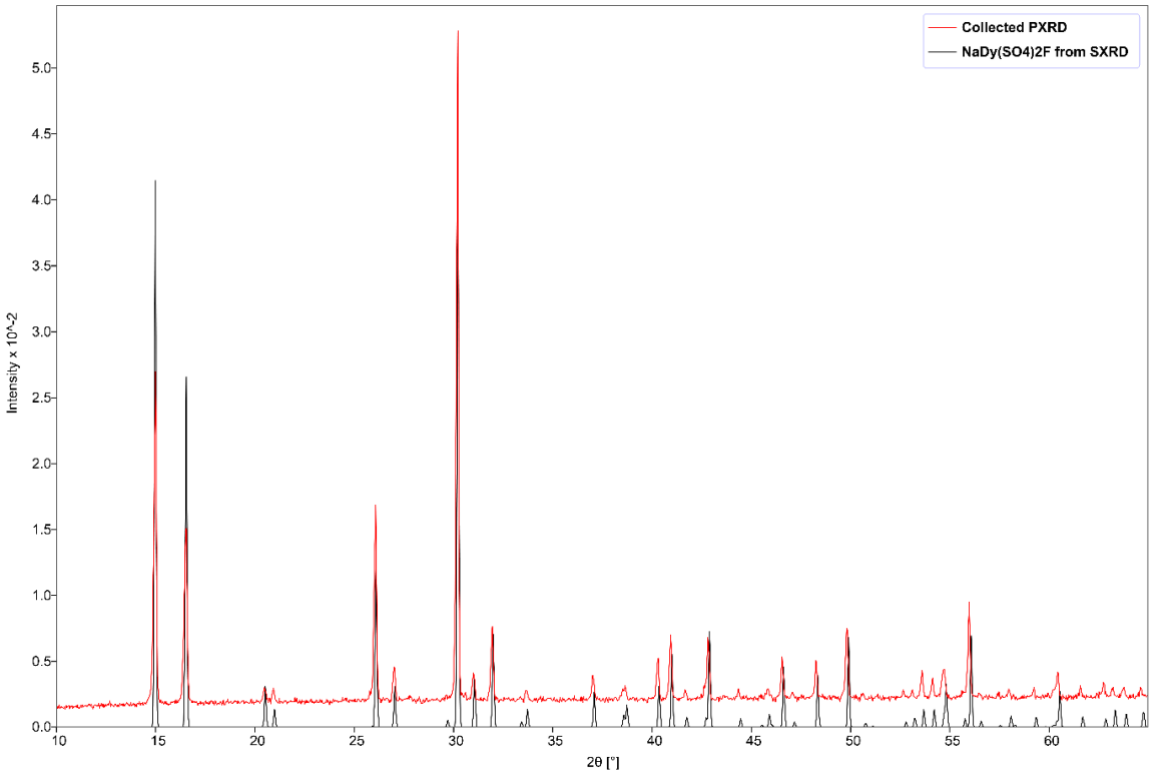

Figure 6.6 Comparison of collected PXRD pattern (red) with simulated PXRD pattern from SXRD data (black) for structure **XVIII**.

The bond lengths between selected bonds are shown in Table 6.9 and are all typical for the atoms involved.

Table 6.9 Bond lengths between atoms in structure **XVIII**.

Bond	Bond Length (Å)	Bond	Bond Length (Å)
Dy1-O1	2.391(5)	S1-O3	1.485(3)
Dy1-O2	2.477(4)	S1-O4	1.472(5)
Dy1-O3	2.449(4)	Na1-O1	2.522(5)
Dy1-O4	2.366(5)	Na1-O2	2.349(5)
Dy1-F1	2.428(6)	Na1-O3	2.413(5)
S1-O1	1.464(5)	Na1-O4	2.873(5)
S1-O2	1.479(4)		

Various lanthanide analogues of structure **XVIII** were synthesised and found in varying phase purity in combination with the relevant lanthanide fluoride and sodium lanthanide sulfate, as shown in Figure 6.7.

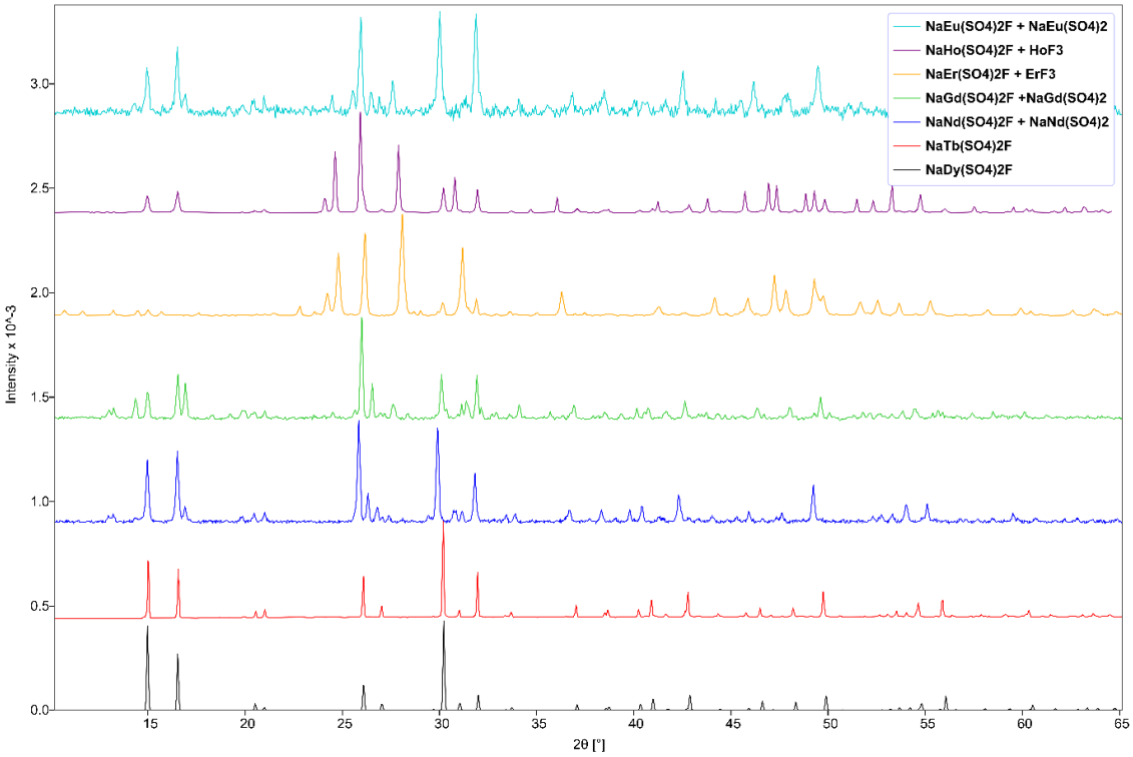

Figure 6.7 Comparison of collected PXRD patterns for $NaLn(SO_4)_2F$ (Ln = Dy, Tb, Nd, Gd, Er, Ho, Eu).

6.4 Structure XIX: $NaY(SO_4)_2$

The product crystallised as colourless prisms, a suitable sample of which was selected for an SXRD study carried out at 150 K on an Agilent SuperNova dual source EosS2 diffractometer operating Mo Kα (λ = 0.71073 Å) radiation. Data collected were refined to a structure containing two-dimensional layers of interconnected YO_7 polyhedra and SO_4 tetrahedra with sodium cations in the interlayer space, Figure 6.8. The structure shows a monoclinic unit cell in space group $P2_1/m$, the crystallographic information for structure **XIX** is summarised in Table 6.10.

Table 6.10 Single crystal diffraction structure solution summary for structure **XIX**.

Empirical Formula	$NaYS_2O_8$
Formula Weight ($gmol^{-1}$)	208.0
Temperature (K)	150
Appearance	Colourless prism
Crystal size (mm)	0.05 × 0.04 × 0.03
Crystal system	Monoclinic
Space group	$P2_1/m$
Unit cell dimensions	a = 4.6594(2) b = 6.8638(4) c = 9.5098(4) β = 96.873(5)
λ/Å	0.71073 (Mo Kα)
Volume ($Å^3$)	301.95(2)
Z	2
Density (gcm^{-3})	2.29
Reflections collected	2315
Unique reflections	774
R_1 (all)	0.033
wR_2 (all)	0.095
GoF	1.783

The layers within structure **XIX** are comprised of YO_7 polyhedra interconnected by one edge sharing SO_4 tetrahedra and five vertex sharing SO_4 tetrahedra. There is one crystallographically distinct Yttrium centre and two crystallographically distinct sulphurs. One SO_4 tetrahedra edge shares with the YO_7 heptahedra further vertex shares with another YO_7 heptahedron and has one terminal oxygen atom which is oriented towards the inter-chain space. The other SO_4 vertex shares with four different YO_7 in the centre of each layer. The singly crystallographically distinct sodium cation is eight-fold coordinated by the terminal and bonding oxygens of the sulfate groups. The layers are stacked directly above one another in the *c*-direction.

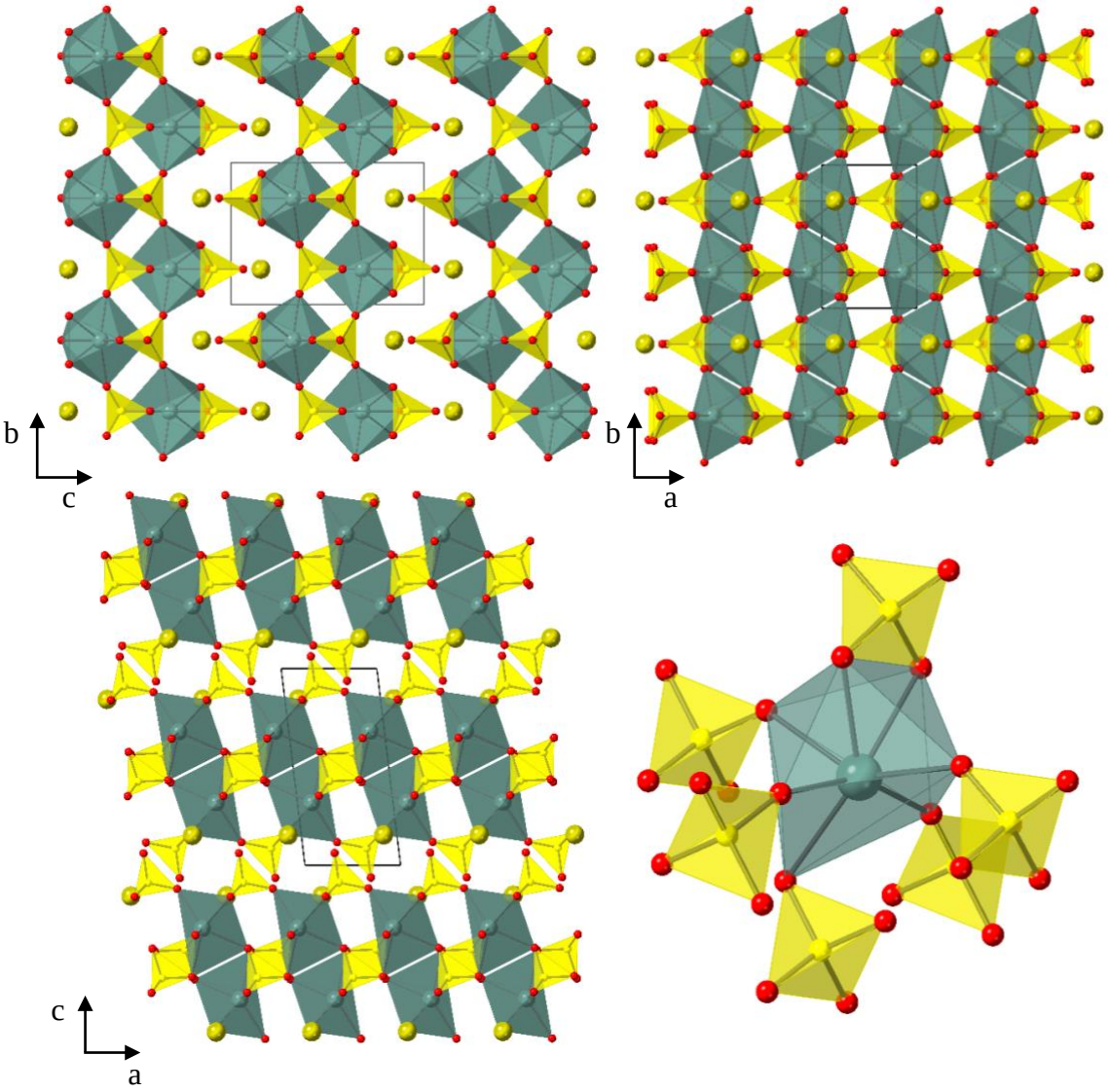

Figure 6.8 Structure **XIX** viewed along the a-axis (top left), c-axis (top right), b-axis (bottom left) and Y connectivity (bottom right). Y heptahedra are shown in grey, SO_4 tetrahedra in yellow and O and Na atoms in red and yellow respectively. The unit cell is outlined in black.

Bond lengths between selected atoms in structure **XIX** are shown in Table 6.11 and are typical for the atoms involved. The calculated bond valence values for structure **XIX** are reported in Table 6.12 and support the calculated formula with Yttrium in the common +3 oxidation state. A low phase purity for structure **XIX** is shown in the comparative PXRD patterns presented in Figure 6.9, the major phase present in the sample matches the PXRD pattern for structure **XVIII**.

Table 6.11 Bond lengths within structure **XIX**.

Bond	Bond Length (Å)	Bond	Bond Length (Å)
Y1-O1	2.264(5)	S2-O1	1.472(5)
Y1-O2	2.416(5)	S2-O3	1.436(5)
	2.628(5)	S2-O5	1.484(4)
Y1-O4	2.381(5)	Na1-O1	2.674(6)
Y1-O5	2.353(3)	Na1-O3	2.430(6)
Y1-O6	2.291(4)		2.538(6)
S1-O2	1.495(5)	Na1-O4	2.896(6)
S1-O4	1.471(5)	Na1-O5	2.272(4)
S1-O6	1.467(4)	Na1-O6	2.695(4)

Table 6.12 Bond valance values calculated for atoms in structure **XIX**

Atom Label	Bond Valence (v.u.)	Atom Label	Bond Valence (v.u.)
Y1	3.2575	O2	2.0363
S1	6.0017	O3	1.9677
S2	6.0683	O4	1.9918
Na1	1.2135	O5	2.1146
O1	2.1203	O6	2.0977

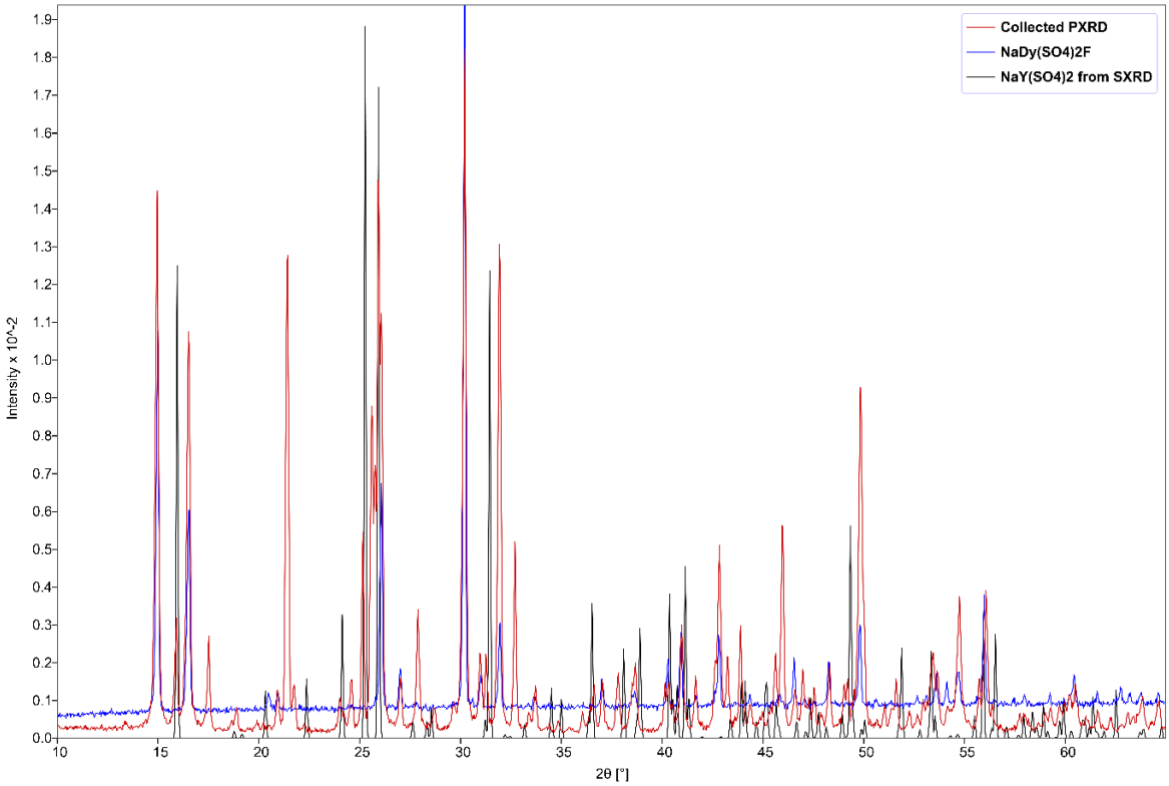

Figure 6.9 Comparative PXRD patterns of $NaY(SO_4)_2$ simulated from SXRD data $NaDy(SO_4)_2F$ and the collected PXRD pattern of the product sample for compound **XIX**.

6.5 Conclusion

Two novel two-dimensional first row transition metal fluoride sulfates and one novel three-dimensional lanthanide fluoride sulfate frameworks have been successfully synthesised and characterised using hydrofluorothermal techniques and single crystal X-ray diffraction. Additionally, one novel two-dimensional yttrium sulfate framework has also been synthesised from hydrofluorothermal conditions and characterised using SXRD. All the frameworks incorporate sodium cations in the inter-framework space with a variety of coordination environments.

The lack of fluoride inclusion in structure **XIX** is attributed to it being a minor-phase product, as determined by PXRD, with the major phase being the yttrium analogue of structure **XVIII**.

Perhaps the most interesting phases in terms of potential application as functional materials in rechargeable Na-ion batteries are structures **XVI** and **XVII** which have the chemical potential for their interlayer sodium ions to be removed.

6.6 References

(1) Wang, Q.; Madsen, A.; Owen, J. R.; Weller, M. T. Direct Hydrofluorothermal Synthesis of Sodium Transition Metal Fluorosulfates as Possible Na-Ion Battery Cathode Materials. *Chem. Commun.* **2013**, *49* (49), 2121–2123.

(2) Riou-Calellec, M.; Serre, C.; Ferey, G. Hydrothermal Synthesis and Structure Determination of [VF(PO_4), $N_2C_2H_9$] and [Ti(OH)(PO_4), $N_2C_2H_9$], Two M(III) Phosphates with the ULM-11 Bidimensional Topology. *C. R. Acad. Sci. Paris* **1999**, *2* (2), 147–152.

(3) Barker, J.; Gover, R. K. B.; Burns, P.; Bryan, A. J. Hybrid-Ion A Lithium-Ion Cell Based on a Sodium Insertion Material. *Electrochem. Solid-State Lett.* **2006**, *9* (4), A190–A192.

(4) Cheetham, A. K.; Férey, G.; Loiseau, T. Open-Framework Inorganic Materials. *Angew. Chemie Int. Ed.* **1999**, *38*, 3268–3292.

(5) Mosymow, E.; Glaum, R.; Kremer, R. K. Searching for "LiCrIIPO_4." *J. Solid State Chem.* **2014**, *218*, 131–140.

(6) Lucazeau, G.; Barj, M.; Soubeyroux, J. L.; Dianoux, A. J.; Delmas, C. Neutron Scattering and Diffraction Study of $Na_3Cr_3P_3O_{12}$, $NaZr_2P_3O_{12}$ and $Na_3ZrMgP_3O_{12}$. *Solid State Ionics* **1986**, *19*, 959–963.

(7) Patoux, S.; Rousse, G.; Leriche, J. B.; Masquelier, C. Crystal Structure and Lithium Insertion Properties of Orthorhombic $Li_2TiFe(PO_4)_3$ and $Li_2TiCr(PO_4)_3$. *Solid State Sci.* **2004**, *6* (10), 1113–1120.

(8) Ledsham, A. H. C.; Steeple, H. The Classification of the Chromium Alums. *Acta Crystallogr. Sect. B Struct. Crystallogr. Cryst. Chem.* **1969**, *25* (2), 398–400.

(9) West, D. V.; Huang, Q.; Zandbergen, H. W.; McQueen, T. M.; Cava, R. J. Structural Disorder, Octahedral Coordination and Two-Dimensional Ferromagnetism in Anhydrous Alums. *J. Solid State Chem.* **2008**, *181* (10), 2768–2775.

(10) Wang, X.; Liu, L.; Ross, K.; Jacobson, A. J. Synthesis and Crystal Structures of Yttrium Sulfates Y(OH)(SO_4), Y(SO_4)F, YNi$(OH)_3(SO_4)$-II and $Y_2Cu(OH)_3(SO_4)2F{\cdot}H_2O$. *Solid State Sci.* **2000**, *2*, 109–118.

(11) Vilela, S. M. F.; Firmino, A. D. G.; Mendes, R. F.; Fernandes, J. A.; Ananias, D.; Valente, A. A.; Ott, H.; Carlos, L. D.; Rocha, J.; Tomé, J. P. C.; Paz, F. A. A. Lanthanide-Polyphosphonate Coordination Polymers Combining Catalytic and Photoluminescence Properties. *Chem. Commun.* **2013**, *49*, 6400–6402.

(12) Vilela, S. M. F.; Fernandes, J. A.; Ananias, D.; Carlos, L. D.; Rocha, J.; Tomé, J. P. C.; Paz, F. A. A. Photoluminescent Layered Lanthanide–Organic Framework Based on a Novel Trifluorotriphosphonate Organic Linker. *Cryst. Eng. Comm.* **2014**, *16*, 344–358.

(13) Vilela, S. M. F.; Ananias, D.; Fernandes, J. A.; Silva, P.; Gomes, A. C.; Silva, N. J. o; Rodrigues, M. O.; Tome, J. C.; Valente, A. A.; Ribeiro-Claro, P.; Carlos, L. D.; Rocha, J.; Almeida Paz, F. A. Multifunctional Micro-and Nanosized Metal– Organic Frameworks Assembled from Bisphosphonates and Lanthanides. *J. Mater. Chem. C* **2014**, *2*, 3311–3327.

(14) Marshall, K. L.; Wang, Q.; Sullivan, H. S. I.; Weller, M. T. Synthesis and Structural Characterisation of Transition Metal Fluoride Sulfates. *Dalt. Trans.* **2016**, *45*.

Chapter 7 : Conclusions

7.0 Overall conclusions and future work

The aim of this research was to utilise 'hydrofluorothermal' and ceramic synthetic methods to produce novel fluoride containing transition metal (and lanthanide) phosphate and sulfate framework materials and to characterise them with SXRD. Both hydrofluorothermal and ceramic reaction mixtures contained high fluoride reagents and minimised water as far as possible, in order to increase the fluoride content in combination with the metal polyanionic frameworks of the crystalline products. Of the nineteen new products presented fluorine was successfully incorporated into fifteen TM/Ln phosphate/sulfate structures.

Ten new titanium containing structures were reported in chapters three and four. The most unusual of these products was the organic tetraazapentacenium salt $[C_{18}N_4H_{14}][TiF_6]$ which comprises of near regular octahedral $[TiF_6]_{2-}$ anions between parallel layers of doubly protonated 5,12-dihydro-5,7,12,14-tetraazapentacene molecular cations. This product was the result of a reaction mixture containing 1,2-phenylenediamine combined with H_2TiF_6 and H_3PO_4, so it is summarised that this could be a simple synthetic route to producing tetraazapentacene species. The more anticipated results were the products which exhibited a combination of titanium, sulfate and fluoride, of which five products were described with a variety of dimensionalities from discreet polyanionic motifs through one-dimensional titanium fluoride and hydrogeno-/fluoro-sulfate chains to a three-dimensional titanium fluoride sulfate. In terms of potential functionalities attributed to structural motifs, the partial cation substitution observed in $Li_{1.87}Ti_{1.13}O_{0.39}F_{1.61}(SO_4)_2$ could extend this structure's connectivity into a three-dimensional framework from one-dimensional chains. If this does not also block potential lithium ion diffusion pathways this material could be of interest as a solid electrolyte or electrode material for lithium ion batteries. This would need to be investigated in further studies than the structural evaluation performed here.

The remaining four titanium-based frameworks are based on phosphates in combination with fluoride ions. Two are similar layered titanium hydrogeno-/fluoro-phosphates with caesium and potassium cations in the inter-layer space and two are three-dimensional titanium fluorophosphates exhibiting cavities/channels. None of the titanium fluorophosphate phases incorporate lithium or sodium ions, however, there are structural features to the three-dimensional phases which would suggest a possibility of small ion transport. As with the $Li_{1.87}Ti_{1.13}O_{0.39}F_{1.61}(SO_4)_2$ structure ion exchange properties could be

tested in further studies of the functionality of these layered and three-dimensional framework materials.

Chapter five described three fluoride inclusive novel manganese structures and two oxo-anion only structures. $LiNa_2MnF_3(SO_4)_2$ and $(H/Li)Na_6Mn_3F_{12}(HPO_4)_2$ successfully incorporated both lithium and sodium counter cations, while the other three are sodium managanese fluoro-/hydrogen-/phoshphate/pyrophosphate structures showing a variety of structural motifs from one dimensional chains, through two-dimensional double layers to a three-dimensional framework. $Na_2Mn_5(PO_4)_4$ and $Na_2Mn_3(P_2O_7)_2$ both contain Mn^{2+} and distorted/irregular manganese coordination environments, whereas the other three managanese structures contain Mn^{3+} and Jahn-Teller distorted octahedral coordination environments. The presence of Mn^{2+} in the last two managanese structures makes them worth looking at in terms of electrochemical properties, as it opens the possibility of the Mn^{2+}/Mn^{4+} double redox potential giving very high capacity to sodium-ion battery cathodes.

Finally, chapter six further explored the sodium/fluoride/sulfate system, this time altering the metal cations from titanium and manganese to vanadium, chromium, yttrium and the lanthanides. The results described four new phases, one of which was not fluoride containing. Of the three structures containing fluoride, two were layered 1^{st} row transition metal fluoride sulfates: $Na_2VF_3SO_4$ and $Na_3CrF_2(SO_4)_2$, both of which have the potential for a > 2 Na ion removal indicating possible high capacity functionality as cathode materials in sodium-ion batteries. The sodium lanthanide fluoride sulfate structure reported is the first example of an ordered fluoride sulfate of greater than two-dimensionality, which is attributed to the greater valency of the larger lanthanide ions allowing for increased connectivity with sulfate anions. Future work should be focused on electrochemical testing of $Na_2VF_3SO_4$ and $Na_3CrF_2(SO_4)_2$ in order to establish if the theoretical 2 - 3 Na per formula unit capacity can be achieved in practice.

Appendix

Comparative PXRD patterns for structures **I** through **IV** published in article reference in Chapter 3 section 3.1:

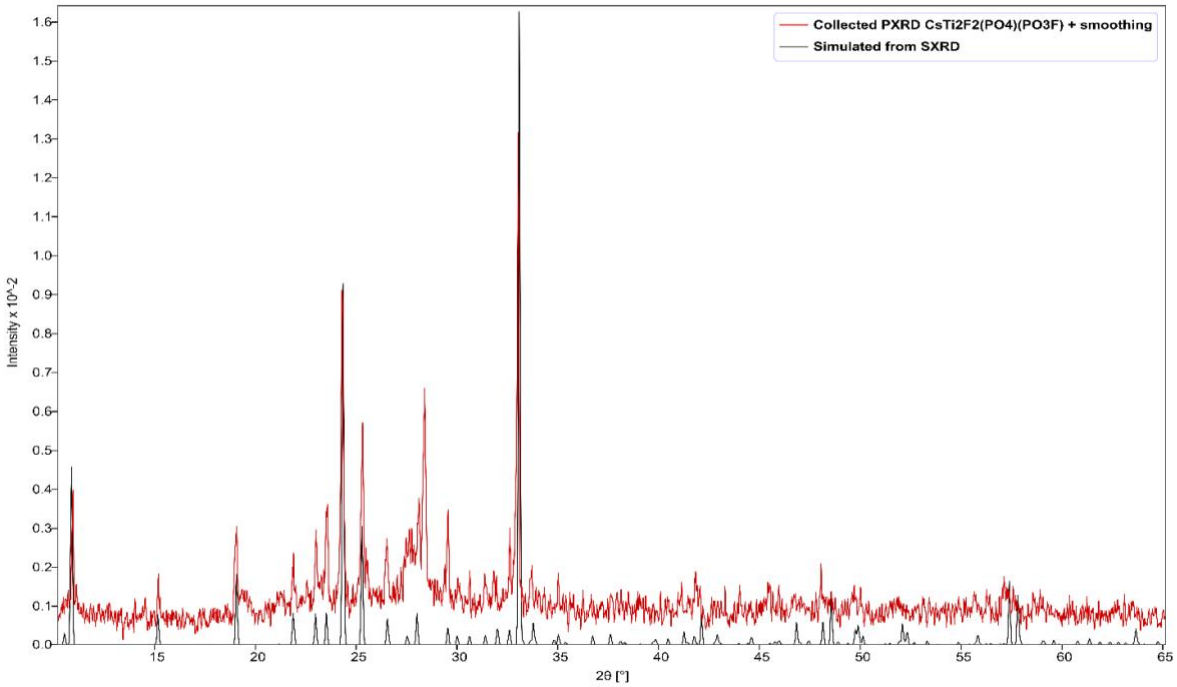

Figure 10 Comparison of collected PXRD pattern (red) with a simulated PXRD pattern from SXRD data (black) for structure **I**.

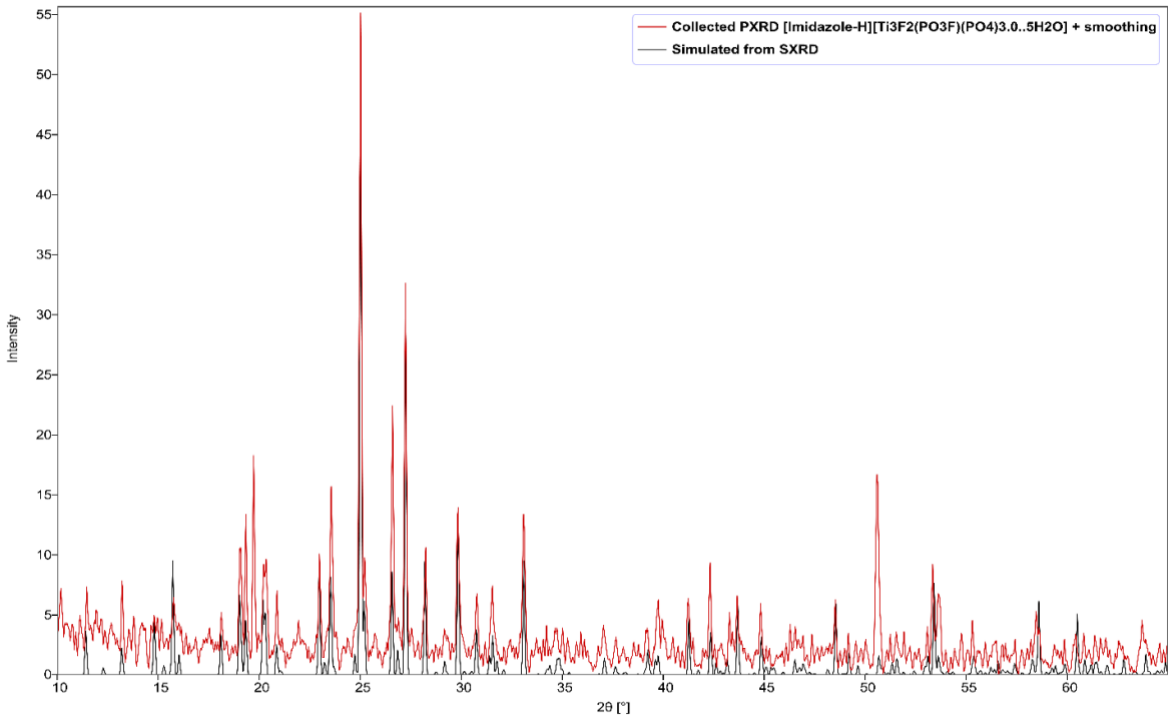

Figure 11 Comparison of collected PXRD pattern (red) with a simulated PXRD pattern from SXRD data (black) for structure **II**.

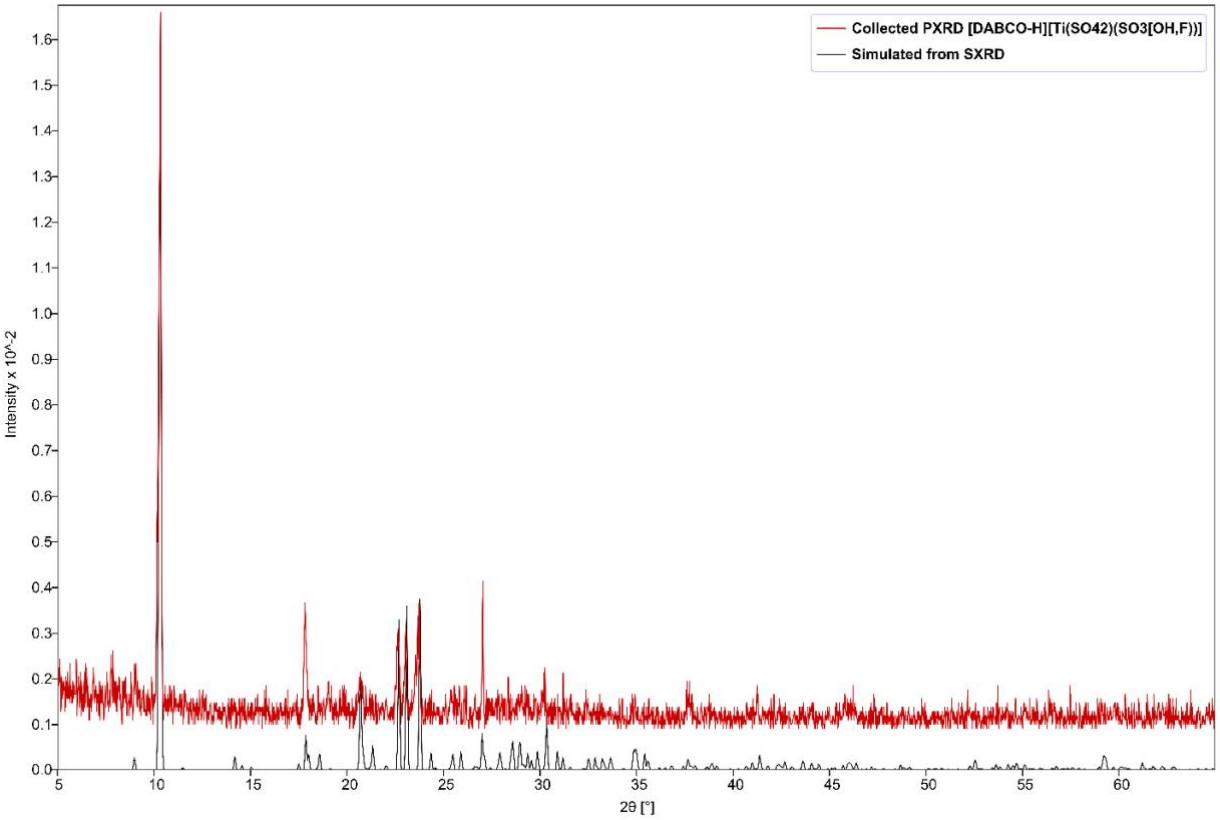

Figure 12 Comparison of collected PXRD pattern (red) with a simulated PXRD pattern from SXRD data (black) for compound **III**.

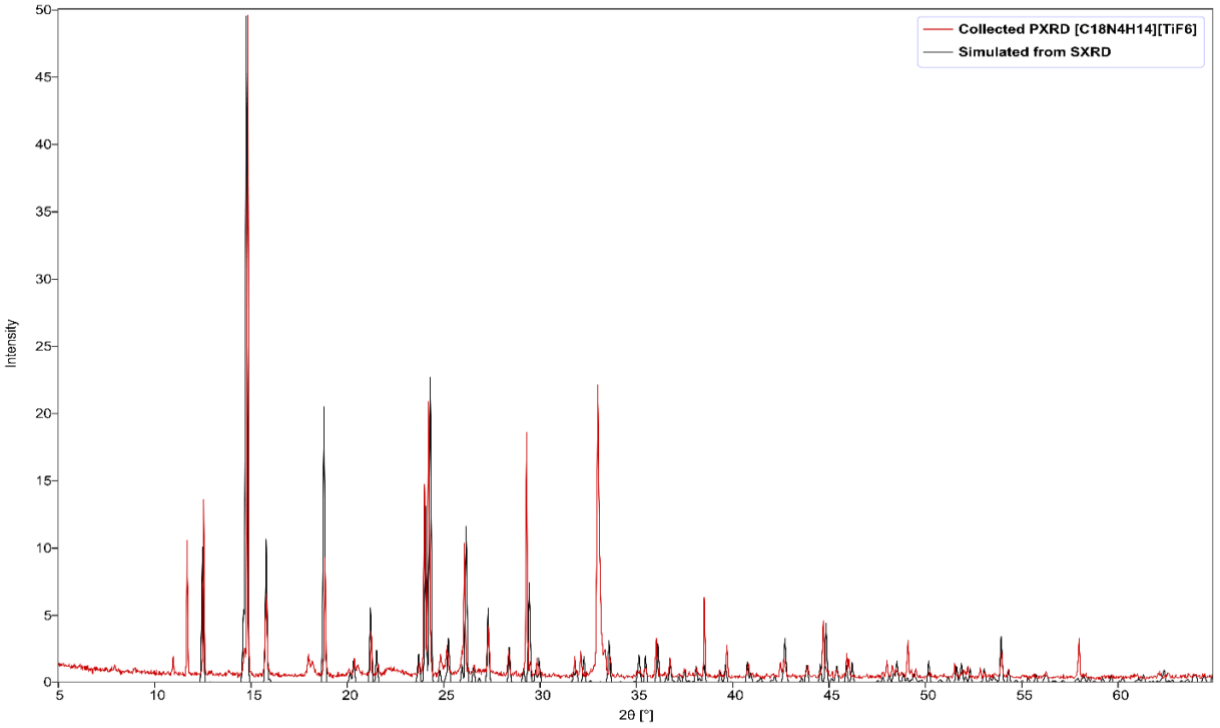

Figure 13 Comparison of collected PXRD pattern (red) with a simulated PXRD pattern from SXRD data (black) for structure **IV**.